

# **Fault Tolerant Control of Active Trailer Steering Systems for Multi-Trailer Articulated Heavy Vehicles**

By

Saurabh Kapoor

A Thesis Presented in Partial Fulfillment of the  
Requirements for the Degree of

Master of Applied Science

in

Automotive Engineering

Faculty of Engineering and Applied Science

University of Ontario Institute of Technology

Oshawa, Ontario, Canada.

July 2017

© 2017 Saurabh Kapoor

***Dedicated***

***to***

***my beloved family***

# ABSTRACT

Faults in a controlled plant often deteriorate the system performance. In severe cases, faults pose a risk of component damage, plant shutdown or even personnel safety. Fault Tolerant Control (FTC) aims at preventing the escalation of rectifiable faults to serious failure. A FTC system combines fault diagnosis with reconfiguration methods to manage faults intelligently. This thesis focuses on FTC systems for Multi-Trailer Articulated Heavy Vehicles (MTAHVs), particularly for Active Trailer Steering (ATS) systems. MTAHVs are vital to the trucking industry, and it is crucial to enhance their safety, reliability and usability. In this research, a 4-DOF linear yaw-plane model of a B-Train double is generated. The vehicle model is validated using the commercial software package, TruckSim. Additionally, this thesis presents an ATS system for the B-Train double. The ATS mechanism is modeled as a hydraulic control system, consisting of a hydraulic actuator and an electrohydraulic control valve. The hydraulics for the ATS system are validated using MathWorks Simscape. To enhance the hydraulic control system's robustness and reliability, FTC is applied. Numerous model-based fault diagnosis techniques such as Kalman Filter, Luenberger Observer, parity equations and residual generation are employed. Furthermore, for the control system synthesis, Linear Quadratic Regulator (LQR) and  $H^\infty$  control techniques are utilized. Control techniques' influence on FTC is analyzed, and the most appropriate technique is proposed for the FTC-ATS control system. Several fault scenarios, such as actuator malfunction(s) and sensor failure are explored, and their impact on system dynamics is investigated.

## **ACKNOWLEDGEMENTS**

I wish to express my heartfelt gratitude to my supervisor, Dr. Yuping He and co-supervisor Dr. Jing Ren, for their assistance, guidance and encouragement. Moreover, I would like to thank Dr. He for this opportunity.

I also thank my fellow graduate students Mr. Tao Sun, Mr. Eungkil Lee, Mr. Zhituo Ni, Ms. Tushita Sikder and Ms. Smitha Vempaty for their support during this research. The financial support of this research by the Natural Science and Engineering Research Council of Canada (NSERC), and Ingersoll Axles is gratefully acknowledged.

# TABLE OF CONTENTS

<b>ABSTRACT</b> .....	iii
<b>ACKNOWLEDGEMENTS</b> .....	iv
<b>TABLE OF CONTENTS</b> .....	v
<b>LIST OF FIGURES</b> .....	x
<b>LIST OF TABLES</b> .....	xxii
<b>ABBREVIATIONS</b> .....	xxiii
<b>CHAPTER 1 INTRODUCTION</b> .....	1
<b>1.1. Multi-Trailer Articulated Heavy Vehicles (MTAHVs)</b> .....	1
<b>1.2. Configuration of MTAHVs</b> .....	2
<b>1.3. Motivation</b> .....	3
<b>1.4. Thesis Contributions</b> .....	6
<b>1.5. Thesis Organization</b> .....	8
<b>CHAPTER 2 LITERATURE REVIEW</b> .....	9
<b>2.1. Introduction</b> .....	9
<b>2.2. ATS systems for MTAHVs</b> .....	9
<b>2.3. Control Techniques for ATS</b> .....	12
<b>2.3.1. LQR Control</b> .....	13
<b>2.3.2. <math>H^\infty</math> Control</b> .....	14
<b>2.4. Fault Tolerant Control (FTC)</b> .....	16

2.4.1.	Introduction .....	16
2.4.2.	Approaches to FTC .....	17
2.4.3.	FTC in ATS systems .....	19
2.5.	FTC Tools and Techniques .....	20
2.5.1.	Model-based FDD Methods .....	20
2.5.2.	Luenberger Observer .....	23
2.5.3.	Kalman Filter .....	24
2.6.	Summary .....	27
<b>CHAPTER 3 VEHICLE SYSTEMS MODELING and VALIDATION .....</b>		<b>28</b>
3.1.	Introduction .....	28
3.2.	Linear Yaw-Plane Model .....	29
3.3.	Model Validation .....	32
3.3.1.	Non-linear TruckSim Model .....	32
3.3.2.	Test Maneuvers for Model Validation.....	34
3.3.3.	Model Validation Results .....	36
3.4.	ATS Hydraulic Actuation (AHA) System.....	39
3.4.1.	Hydraulic Actuator Modeling .....	39
3.4.2.	Electrohydraulic Valve Modeling.....	44
3.5.	AHA System Model Validation .....	46
3.5.1.	Non-linear Simscape Model .....	46

3.5.2. AHA System Validation .....	47
3.6. Summary .....	48
<b>CHAPTER 4 FAULT TOLERANT CONTROL OF ACTIVE TRAILER STEERING SYSTEMS .....</b>	<b>49</b>
4.1. Introduction .....	49
4.2. Controller Synthesis .....	51
4.2.1. Introduction .....	51
4.2.2. LQR Control.....	52
4.2.2.1. LQR Control Theory .....	52
4.2.2.2. Selection of Q and R Matrices.....	52
4.2.2.3. Simulation Results .....	53
4.2.3. $H^\infty$ Control .....	57
4.2.3.1. $H^\infty$ Control Theory .....	57
4.2.3.2. Selection of Weighting Functions.....	58
4.2.3.3. Controller Optimization for Variation in Forward Speed....	62
4.2.3.4. Yaw Rate Reference Model.....	63
4.2.3.5. Simulation Results .....	64
4.3. ATS Hydraulic Actuation (AHA) System Integration .....	69
4.3.1. Introduction .....	69
4.3.2. PID Controller.....	69

4.3.3.	Simulation Results.....	70
4.4.	Observer Selection.....	81
4.4.1.	Introduction.....	81
4.4.2.	Observer Design Techniques .....	82
4.4.2.1.	Luenberger Observer .....	82
4.4.2.2.	Kalman Filter.....	83
4.4.3.	Simulation Results.....	84
4.4.3.1.	Sensor Measurements .....	84
4.4.3.2.	Sensor Measurements with Additive Noise .....	88
4.4.3.3.	Sensor Measurements with Additive Noise and different Initial Conditions.....	91
4.5.	FTC-ATS Framework.....	96
4.5.1.	Introduction.....	96
4.5.2.	Overview of the FTC-ATS Framework.....	97
4.5.3.	Fault Detection and Diagnosis.....	98
4.5.3.1.	Observer 1.....	98
4.5.3.2.	Observer 2.....	102
4.5.3.3.	Observer 3.....	109
4.5.4.	Fault Tolerance .....	111
4.5.4.1.	Residual Generation .....	111

4.5.4.2.	Fail-Operational and Fail-Safe Modes .....	115
4.5.4.3.	Simulation Setup .....	117
4.5.5.	Simulation Results.....	118
4.5.5.1.	Sensor Failure .....	118
4.5.5.2.	Actuator Malfunction(s) .....	124
4.5.5.3.	Fail-Safe Operation .....	131
4.6.	Summary .....	134
<b>CHAPTER 5 CONCLUSIONS and RECOMMENDATIONS FOR FUTURE</b>		
<b>RESEARCH .....</b>		
5.1.	Conclusions.....	135
5.2.	Recommendations for Future Research .....	138
<b>PUBLICATIONS.....</b>		
<b>REFERENCES .....</b>		
<b>APPENDIX A: NOTATIONS OF THE 4DOF B-TRAIN DOUBLE MODEL</b>		
<b>PARAMETERS .....</b>		
<b>APPENDIX B: VEHICLE SYSTEMS MATRICES .....</b>		

# LIST OF FIGURES

Figure 3.1 Configuration of the linear B-Train model.....	29
Figure 3.2 Configuration of the B-Train MTHAV.....	33
Figure 3.3 TruckSim's User Interface (Run Control Screen).....	33
Figure 3.4 Schematic representation of the single lane change maneuver specified by SAE J2179 [84].....	34
Figure 3.5 Time history of Steering Wheel Angles for the 1 <sup>st</sup> SLC and the 2 <sup>nd</sup> SLC maneuvers.....	35
Figure 3.6 Time history of lateral accelerations of the 4DOF model and the TruckSim model under the 1 <sup>st</sup> SLC test maneuver.....	37
Figure 3.7 Time history of lateral accelerations of the 4DOF model and the TruckSim model under the 2 <sup>nd</sup> SLC test maneuver.....	37
Figure 3.8 Time history of yaw rates of the 4DOF model and the TruckSim model under the 1st SLC test maneuver.....	38
Figure 3.9 Time history of yaw rates of the 4DOF model and the TruckSim model under the 2 <sup>nd</sup> SLC test maneuver.....	38
Figure 3.10 Schematic diagram for the AHA system [85].....	40
Figure 3.11 Block diagram of the Simscape hydraulic model.....	46
Figure 3.12 Time history of actuator position response for the AHA model and the Simscape model to the step input.....	47

Figure 3.13 Time history of actuator position response for the AHA model and the Simscape model to the sinewave input.....	48
Figure 4.1 Time history of Steering Wheel Angles for SLC and DLC maneuvers..	50
Figure 4.2 Time history of lateral accelerations for the LQR controlled vehicle and the baseline vehicle under the SLC maneuver.....	54
Figure 4.3 Time history of lateral accelerations for the LQR controlled vehicle and the baseline vehicle under the DLC maneuver.....	54
Figure 4.4 Time history of yaw rates for the LQR controlled vehicle and the baseline vehicle under the SLC maneuver.....	55
Figure 4.5 Time history of yaw rates for the LQR controlled vehicle and the baseline vehicle under the DLC maneuver.....	55
Figure 4.6 Trajectories of the LQR controlled vehicle and the baseline vehicle under the SLC maneuver.....	56
Figure 4.7 Trajectories of the LQR controlled vehicle and the baseline vehicle under the DLC maneuver.....	56
Figure 4.8 Configuration of a generalized $H^\infty$ closed-loop system.....	58
Figure 4.9 Configuration of the $H^\infty$ controller for ATS system.....	59
Figure 4.10 Frequency response of the $H^\infty$ closed-loop system in the entire range vehicle forward speeds.....	62

Figure 4.11 Time history of lateral accelerations for the $H^\infty$ controlled vehicle and the baseline vehicle under the SLC maneuver.....	65
Figure 4.12 Time history of lateral accelerations for the $H^\infty$ controlled vehicle and the baseline vehicle under the DLC maneuver.....	65
Figure 4.13 Time history of yaw rates for the $H^\infty$ controlled vehicle and the baseline vehicle under the SLC maneuver.....	66
Figure 4.14 Time history of yaw rates for the $H^\infty$ controlled vehicle and the baseline vehicle under the DLC maneuver.....	66
Figure 4.15 Time history of yaw rates for the $H^\infty$ controlled vehicle, and the reference signals under the SLC maneuver.....	67
Figure 4.16 Time history of yaw rates for the $H^\infty$ controlled vehicle, and the reference signals under the DLC maneuver.....	67
Figure 4.17 Trajectories of the $H^\infty$ controlled vehicle and the baseline vehicle under the SLC maneuver.....	68
Figure 4.18 Trajectories of the $H^\infty$ controlled vehicle and the baseline vehicle under the DLC maneuver.....	68
Figure 4.19 Time history of lateral accelerations for the AHA-LQR controlled vehicle and the LQR controlled vehicle under the SLC maneuver.....	71
Figure 4.20 Time history of lateral accelerations for the AHA-LQR controlled vehicle and the LQR controlled vehicle under the DLC maneuver.....	71

Figure 4.21 Time history of yaw rates for the AHA-LQR controlled vehicle and the LQR controlled vehicle under the SLC maneuver.....	72
Figure 4.22 Time history of yaw rates for the AHA-LQR controlled vehicle and the LQR controlled vehicle under the DLC maneuver.....	72
Figure 4.23 Time history of ATS angles achieved by the AHA-LQR system, and the desired ATS angles under the SLC maneuver.....	73
Figure 4.24 Time history of ATS angles achieved by the AHA-LQR system, and the desired ATS angles under the DLC maneuver.....	73
Figure 4.25 Time history of lateral accelerations for the AHA-H $\infty$ controlled vehicle and the H $\infty$ controlled vehicle under the SLC maneuver.....	75
Figure 4.26 Time history of lateral accelerations for the AHA-H $\infty$ controlled vehicle and the controlled H $\infty$ vehicle under the DLC maneuver.....	75
Figure 4.27 Time history of yaw rates for the AHA-H $\infty$ controlled vehicle and the H $\infty$ controlled vehicle under the SLC maneuver.....	76
Figure 4.28 Time history of yaw rates for the AHA-H $\infty$ controlled vehicle and the H $\infty$ controlled vehicle under the DLC maneuver.....	76
Figure 4.29 Time history of ATS angles achieved by the AHA-H $\infty$ system, and the desired ATS angles under the SLC maneuver.....	77
Figure 4.30 Time history of ATS angles achieved by the AHA-H $\infty$ system, and the desired ATS angles under the DLC maneuver.....	77

Figure 4.31 Time history of lateral accelerations for the AHA- $H^\infty$  controlled vehicle and the  $H^\infty$  controlled vehicle under the DLC maneuver at 120 km/h.....79

Figure 4.32 Time history of yaw rates for the AHA- $H^\infty$  controlled vehicle and the  $H^\infty$  controlled vehicle under the DLC maneuver at 120 km/h.....80

Figure 4.33 Time history of ATS angles achieved by the AHA- $H^\infty$  system, and the desired ATS angles under the DLC maneuver at 120 km/h.....80

Figure 4.34 Time history of lateral acceleration predictions for the Kalman Filter and Luenberger Observer, and the true outputs under the SLC maneuver using sensor measurements. ....86

Figure 4.35 Time history of lateral acceleration predictions for the Kalman Filter and Luenberger Observer, and the true outputs under the DLC maneuver using sensor measurements.....86

Figure 4.36 Time history of yaw rate predictions for the Kalman Filter and Luenberger Observer, and the true outputs under the SLC maneuver using sensor measurements.....87

Figure 4.37 Time history of yaw rate predictions for the Kalman Filter and Luenberger Observer, and the true outputs under the DLC maneuver using sensor measurements.....87

Figure 4.38 Time history of lateral acceleration predictions for the Kalman Filter and Luenberger Observer, and the true outputs under the SLC maneuver using sensor measurements with additive noise.....89

Figure 4.39 Time history of lateral acceleration predictions for the Kalman Filter and Luenberger Observer, and the true outputs under the DLC maneuver using sensor measurements with additive noise.....89

Figure 4.40 Time history of yaw rate predictions for the Kalman Filter and Luenberger Observer, and the true outputs under the SLC maneuver using sensor measurements with additive noise.....90

Figure 4.41 Time history of yaw rate predictions for the Kalman Filter and Luenberger Observer, and the true outputs under the DLC maneuver using sensor measurements with additive noise.....90

Figure 4.42 Time history of Steering Wheel Angles for the SLC and DLC maneuvers utilized for different initial conditions predictions.....91

Figure 4.43 Time history of lateral acceleration predictions for the Kalman Filter and Luenberger Observer, and the true outputs under the SLC maneuver using sensor measurements with additive noise and different initial conditions.....92

Figure 4.44 Time history of lateral acceleration predictions for the Kalman Filter and Luenberger Observer, and the true outputs under the DLC maneuver using sensor measurements with additive noise and different initial conditions.....93

Figure 4.45 Time history of yaw rate predictions for the Kalman Filter and Luenberger Observer, and the true outputs under the SLC maneuver using sensor measurements with additive noise and different initial conditions.....94

Figure 4.46 Time history of yaw rate predictions for the Kalman Filter and Luenberger Observer, and the true outputs under the DLC maneuver using sensor measurements with additive noise and different initial conditions.....95

Figure 4.47 The schematic representation of the sub-systems structure of the vehicle.....97

Figure 4.48 Time history of yaw rate estimates by Observer 1, and the actual TruckSim outputs under the SLC maneuver.....101

Figure 4.49 Time history of yaw rate estimates by Observer 1, and the actual TruckSim outputs under the DLC maneuver.....101

Figure 4.50 Time history of force output estimates by Observer 2, and the actual force outputs under the SLC maneuver.....106

Figure 4.51 Time history of force output estimates by Observer 2, and the actual force outputs under the DLC maneuver.....106

Figure 4.52 Time history of actuator velocity estimates by the Kalman Filter (Observer 2), and the actual velocity outputs under the SLC maneuver.....107

Figure 4.53 Time history of actuator velocity estimates by the Kalman Filter (Observer 2), and the actual velocity outputs under the DLC maneuver.....107

Figure 4.54 Time history of actuator position estimates by the Kalman Filter (Observer 2), and the actual position outputs under the SLC maneuver.....108

Figure 4.55 Time history of actuator position estimates by the Kalman Filter (Observer 2), and the actual position outputs under the DLC maneuver.....108

Figure 4.56 Time history of ATS angle estimates by Observer 3, and the actual ATS angles under the SLC maneuver.....110

Figure 4.57 Time history of ATS angle estimates by Observer 3, and the actual ATS angles under the DLC maneuver.....110

Figure 4.58 Time history of Observer 1’s residual signals, and the threshold limits under the SLC maneuver.....112

Figure 4.59 Time history of Observer 1’s residual signals, and the threshold limits under the DLC maneuver.....112

Figure 4.60 Time history of Observer 2’s residual signals, and the threshold limits under the SLC maneuver.....113

Figure 4.61 Time history of Observer 2’s residual signals, and the threshold limits under the DLC maneuver.....113

Figure 4.62 Time history of Observer 3’s residual signals, and the threshold limits under the SLC maneuver.....114

Figure 4.63 Time history of Observer 3’s residual signals, and the threshold limits under the DLC maneuver.....114

Figure 4.64 Simplified Simulink diagram signifying the FTC system built using TruckSim and Simulink software.....117

Figure 4.65 Time history of Observer 1’s residual signals, and the threshold limits under the SLC maneuver for the yaw-rate sensor failure.....119

Figure 4.66 Time history of Observer 1’s residual signals, and the threshold limits under the DLC maneuver for the yaw-rate sensor failure.....	119
Figure 4.67 Time history of lateral accelerations for the $H^\infty$ controlled vehicle and the baseline TruckSim vehicle under the SLC maneuver for the yaw-rate sensor failure.....	120
Figure 4.68 Time history of lateral accelerations for the $H^\infty$ controlled vehicle and the baseline TruckSim vehicle under the DLC maneuver for the yaw-rate sensor failure .....	120
Figure 4.69 Time history of yaw rates for the $H^\infty$ controlled vehicle and the baseline TruckSim vehicle under the SLC maneuver for the yaw-rate sensor failure.....	121
Figure 4.70 Time history of yaw rates for the $H^\infty$ controlled vehicle and the baseline TruckSim vehicle under the DLC maneuver for the yaw-rate sensor failure.....	121
Figure 4.71 Time history of lateral accelerations for the $H^\infty$ controlled (Observer 1) vehicle and the baseline TruckSim vehicle under the SLC maneuver for the yaw-rate sensor failure.....	122
Figure 4.72 Time history of lateral accelerations for the $H^\infty$ controlled (Observer 1) vehicle and the baseline TruckSim vehicle under the DLC maneuver for the yaw-rate sensor failure.....	122
Figure 4.73 Time history of yaw rates for the $H^\infty$ controlled (Observer 1) vehicle and the baseline TruckSim vehicle under the SLC maneuver for the yaw-rate sensor failure.....	123

Figure 4.74 Time history of yaw rates for the  $H^\infty$  controlled (Observer 1) vehicle and the baseline TruckSim vehicle under the DLC maneuver for the yaw-rate sensor failure.....123

Figure 4.75 Time history of Observer 2’s residual signals, the threshold limits, force output estimates, and the actual force outputs under the SLC maneuver for Axle 4’s actuator malfunction.....125

Figure 4.76 Time history of Observer 2’s residual signals, the threshold limits, force output estimates, and the actual force outputs under the DLC maneuver for Axle 4’s actuator malfunction.....125

Figure 4.77 Time history of Observer 3’s residual signals, the threshold limits, ATS angle estimates, and the actual ATS angles under the SLC maneuver for Axle 4’s actuator malfunction.....126

Figure 4.78 Time history of Observer 3’s residual signals, the threshold limits, ATS angle estimates, and the actual ATS angles under the DLC maneuver for Axle 4’s actuator malfunction.....126

Figure 4.79 Time history of Observer 2’s residual signals, the threshold limits, force output estimates, and the actual force outputs under the SLC maneuver for Axle 6’s actuator malfunction.....127

Figure 4.80 Time history of Observer 2’s residual signals, the threshold limits, force output estimates, and the actual force outputs under the DLC maneuver for Axle 6’s actuator malfunction.....127

Figure 4.81 Time history of Observer 3’s residual signals, the threshold limits, ATS angle estimates, and the actual ATS angles under the SLC maneuver for Axle 6’s actuator malfunction.....	128
Figure 4.82 Time history of Observer 3’s residual signals, the threshold limits, ATS angle estimates, and the actual ATS angles under the DLC maneuver for Axle 6’s actuator malfunction.....	128
Figure 4.83 Time history of Observer 2’s residual signals, the threshold limits, force output estimates, and the actual force outputs under the SLC maneuver for Axle 7’s actuator malfunction.....	129
Figure 4.84 Time history of Observer 2’s residual signals, the threshold limits, force output estimates, and the actual force output under the DLC maneuver for Axle 7’s actuator malfunction.....	129
Figure 4.85 Time history of Observer 3’s residual signals, the threshold limits, ATS angle estimates, and the actual ATS angles under the SLC maneuver for Axle 7’s actuator malfunction.....	130
Figure 4.86 Time history of Observer 3’s residual signals, the threshold limits, ATS angle estimates, and the actual ATS angles under the DLC maneuver for Axle 7’s actuator malfunction.....	130
Figure 4.87 Time history of lateral accelerations for the $H^\infty$ controlled vehicle and the baseline TruckSim vehicle under the DLC maneuver for Axle 4’s actuator malfunction.....	132

Figure 4.88 Time history of FTC system’s residual signal and the threshold limit under the DLC maneuver for Axle 4’s actuator malfunction.....132

Figure 4.89 Time history of lateral accelerations for the FTC vehicle and the baseline TruckSim vehicle under the DLC maneuver for Axle 4’s actuator malfunction.....133

Figure 4.90 Time history of ATS angles generated by the FTC system, and the actual ATS angles under the DLC maneuver for Axle 4’s actuator malfunction.....133

# LIST OF TABLES

Table 3.1 Table 3.1 Design parameters for AHA system [85-89].....	45
Table 4.1 Optimal Weighting Functions for the $H^\infty$ Controller.....	61
Table 4.2 FDD and FTC Modes.....	116

# ABBREVIATIONS

*4WS* Four Wheel Steering

*AFS* Active Front Steering

*AHA* ATS Hydraulic Actuation

*ARC* Active Roll Control

*ARE* Algebraic-Riccati Equations

*ATS* Active Trailer Steering

*CG* Center of Gravity

*CVDC* Cambridge Vehicle Dynamics Consortium

*DHIL* Driver Hardware-In-the-Loop

*DLC* Double Lane Change

*DOF* Degree(s) of Freedom

*EV* Electric Vehicle

*FDD* Fault Detection and Diagnosis

*FO* Fail Operational

*FS* Fail Safe

*FTC* Fault Tolerant Control

*GA* Genetic Algorithm

*HIL* Hardware-In-the-Loop

*IVHS* Intelligent Vehicle Highway Systems

*LPV* Linear Parameter Varying

*LQR* Linear Quadratic Regular

*MIMO* Multi-Input Multi-Output

*MRAC* Model Reference Adaptive Control

*MTAHV* Multi-Trailer Articulated Heavy Vehicles

*MVSDL* Multi-disciplinary Vehicle System Design Laboratory

*PBS* Performance Based Standards

*PFOT* Path-Following Off-Tracking

*PID* Proportional Integral Derivative

*RWA* Rear-Ward Amplification

*SAE* Society of Automotive Engineers

*SIL* Software-In-the-Loop

*SLC* Single Lane Change

*UOIT* University of Ontario Institute of Technology

*VS* Vehicle Sim

# CHAPTER 1

## INTRODUCTION

### 1.1. Multi-Trailer Articulated Heavy Vehicles (MTAHVs)

The trucking industry is a vital component of a country's economy. It continues to be the primary mode of transportation for moving freight. However, with the ever-increasing oil prices, and global warming concerns, the industry faces an enduring demand to enhance the transportation efficiency. So far, single-unit vehicles, such as trucks and tractor-semitrailers, have dominated the trucking industry. In the past decades, however, Multi-Trailer Articulated Heavy Vehicles (MTAHVs) have been introduced, which offer a significant reduction in shipping costs and emissions. MTAHVs are a cost-effective, logistically efficient and adaptable solution for freight transportation [1]. Moreover, they exhibit superior fuel economy in comparison to single-unit vehicles [2, 3].

MTAHVs can reduce shipping costs in the range of \$374 million to \$1.9 billion a year compared to the commonly used tractor-semitrailer combinations [4]. In Alberta, Canada, MTAHVs have displayed the capability to reduce the cost of shipping by 40%, fuel by 32%, and pavement wear by 40% [5]. MTAHVs have demonstrated the potential to save nearly \$320 million, and 70 million liters fuel a year in Ontario, Canada [6]. Additionally, such vehicles promote traffic decongestion and have a substantial impact on reducing greenhouse gas emissions [4-8].

## 1.2. Configuration of MTAHVs

A MTAHV comprises of a towing unit and two or more trailing units coupled by articulation joints. The leading unit, typically, consists of a steerable axle at the front end followed by one or more rigid axles at the rear. The trailing unit is termed as a trailer. Generally, trailers can be categorized as full trailers or semitrailers. In a full trailer, running gear support the trailer's load at its front and rear ends, whereas in a semitrailer, the load is supported by the running gear at the rear end and by the leading unit at the front end [1, 3]. Vehicle units connect to one another by means of mechanical couplings, such as dollies, hitches, pintles and fifth-wheels [1, 3].

MTAHVs may be classified as A, B and C Trains depending upon the mechanical coupling employed to connect the trailers. A-Train is a combination of a tractor-semitrailer towing one or more trailers using a converter dolly as a mechanical coupling for connecting the semitrailers. Despite being the most commonly used configuration, A-Trains exhibit poor lateral stability at high-speeds [1, 6]. The B-train configuration successfully mitigates the poor lateral stability problem by employing fewer articulation joints [1]. In a B-Train, the towing trailers include extended frames, on which the fifth-wheel coupling is mounted for accommodating the towed semitrailers [1]. Such configurations however, pose logistical concerns, as they require special towing units. Conversely, in an A-Train a conventional semitrailer can be used at any position. Similar to A-trains, C-Trains employ converter dollies to connect the trailers [1]. However, unlike an A-Train, a C-Train's dolly does not allow articulation between the dolly and the vehicle unit(s).

### **1.3. Motivation**

Despite their numerous benefits, MTAHVs' poor directional performance restricts their applications [6]. In Ontario, Canada, MTAHVs are allowed to operate exclusively on designated freeway networks and approved municipal roads. Moreover, they cannot carry Gross Vehicle Weight greater than that of a conventional tractor-semitrailer [6]. Similarly, in USA, under the Intermodal Surface Transportation Efficiency Act of 1991, MTAHVs are permitted in merely "19" of 50 states due to concerns of safety and infrastructure damage [6, 9].

MTAHVs exhibit reduced low-speed maneuverability and diminished high-speed lateral stability. The reduced low-speed maneuverability occurs due to the increased overall length and addition of unit(s) [1, 7]. This leads to large path-following off-tracking (PFOT), rendering them unsuitable for narrow city roads. The curtailed high-speed lateral stability arises due to increased number of articulated joints. These drawbacks often make MTAHVs prone to unstable motions, such as trailer sway, jack-knifing and rollover [6-8].

Research shows that in USA and Canada nearly 23% of all heavy vehicle accidents are associated with rollover [10, 11]. In USA alone, each year there are over 25,000 rollovers of commercial trucks including tractor-semitrailers [10, 12]. Moreover, accidents involving heavy vehicles cause greater damage and injury.

Australian Performance Based Standards (PBS) specify static rollover threshold, rearward amplification (RWA) ratio, and yaw damping coefficient as high-speed directional performance measures for ensuring vehicle stability [13,

14]. Static rollover threshold, defined in terms of peak lateral acceleration, is a standard measure of vehicle's roll stability [6, 15], as rollover tends to occur while negotiating high-speed sharp (high lateral acceleration) corners [6, 15]. It is interesting to note that the static rollover threshold for most passenger cars is larger than 1 g; for light trucks, vans and SUVs the threshold is in the range of 0.8-1.2 g; whereas for MTAHVs the threshold is less than 0.5 g [6, 15].

MTAHV's high center of gravity (CG) and relatively narrow track width renders them particularly susceptible to rollover [6-7, 13]. Moreover, in articulated vehicles including MTAHVs, the rearmost trailer has the highest tendency to rollover [13], which is usually ascribed to a phenomenon known as rearward amplification or RWA.

RWA causes the rearmost trailer to reach a higher maximum lateral acceleration than that of the towing unit, especially under high-speed evasive maneuvers [13, 16-18]. The performance measure, RWA ratio, is defined as the ratio of the peak lateral acceleration at the rearmost trailer to that of the towing unit, at their respective CG's, under an obstacle avoidance lane-change maneuver [1, 13]. The maximum RWA ratio acknowledged by the PBS is associated with the static rollover threshold [13, 19-23]. Further, vehicle's roll stability is highly dependent on the RWA ratio [13, 18]. The aforementioned concerns discredit the benefits offered by MTAHVs. Hence, it is necessary to address these concerns in order to facilitate their large-scale commercialization.

Numerous control technologies such as anti-roll control, differential braking and active trailer steering have been proposed to enhance the low-speed and high-speed performance of MTAHVs [6, 13]. Amongst these, a promising technology is Active Trailer Steering (ATS) [6-8, 13]. ATS comprises of steerable trailer axles, where a suitable control system generates the optimal steering angle depending on the low-speed and high-speed requirements [6-8, 13]. Although, systems such as ATS are very crucial for MTAHVs directional performance, like other cited technologies, ATS is still under development and not utilized commercially.

So far, ATS systems have been restricted to laboratory experiments and simulations. This limited use of ATS can be attributed to numerous reasons, though the primary causes are system performance in real-life and in presence of faults and failures. Faults in a control system can adversely affect its performance. Moreover, in some cases, seemingly benign faults can propagate to cause disastrous system failures. Hence, the need for a fault tolerance scheme arises to combat situations where faults may cause such systems to fail and induce accidents.

Fault Tolerant Control (FTC) systems take into account scenarios where some arbitrary fault can occur in a controlled plant, which may degrade the robustness of the system and cause systems failures. In other words, a fault tolerant controller can detect the existence of a fault within the plant and respond to counteract or diminish the faulty behavior within the plant [25].

In the last few years, FTC has been applied to innumerable automotive systems and sub-systems such as drive-by-wire systems, electronic steering, feedback sensors, and so on [26, 27]. Considering its potential to maintain system capability in presence of faults, it can be particularly beneficial for MTAHVs, where real-life applications are still a major concern. Hence, in this research, the primary focus will be to develop a fault tolerant system for MTAHV's ATS systems to enhance their safety characteristics and aid them to achieve widespread implementation.

#### **1.4. Thesis Contributions**

Contributions made towards implementing FTC in MTAHVs have been summarized in this section. The prime focus of this research has been to apply FTC techniques to ATS systems.

FTC relies on analytical redundancy methods to investigate the propagation of faults in a system. Generally, these methods are based on the physical system's mathematical models. Thus, a 4DOF linear model for a B-Train double is developed, followed by model validation using TruckSim software package.

Since actuators significantly affect a control system's performance, an effective control system design must consider the actuator's dynamics. In this research, for the first time the effects of actuator dynamics on an ATS control system are considered. To allow the study of actuator dynamics, a linear model for an ATS Hydraulic Actuation (AHA) system is developed. The AHA system model is verified using MathWorks Simscape software package.

The thesis presents ATS control systems based on the Linear Quadratic Regular (LQR), and  $H^\infty$  control techniques. A comparative analysis of the LQR and  $H^\infty$  based ATS controllers is performed under complex high-speed maneuvers. In addition to studying the effects of actuator dynamics on the above control techniques, both control techniques are analyzed for suitability to the FTC-ATS scheme.

An important aspect of FTC is the supervision system or the Fault Detection and Diagnosis (FDD) sublayer, which is responsible for fault detection, fault isolation and fault magnitude estimation. This thesis presents a novel FDD system, specifically, to predict the impending faults in an ATS control system. Moreover, two FDD methods, Luenberger Observer and Kalman Filter, are compared under a variety of simulated test conditions. Analytical redundancy tools such as Kalman Filters, residual generation and parity equations, have been used to develop a comprehensive FDD system.

A FTC scheme defines certain failure modes, which instruct the active control system to remain operational or shutdown in case of a failure. This thesis presents a FTC scheme to regulate the ATS control system during fault occurrences. Software-In-the-loop (SIL) simulations for the FTC system are performed using MATLAB/Simulink and TruckSim platforms. The vehicle's high-speed lateral stability is analyzed under Single-lane Change (SLC) and Double-lane Change (DLC) maneuvers. Various cases of faults, such as actuator failure, and sensor failure are explored, and their impact on system performance is examined.

## 1.5. Thesis Organization

Chapter 1 introduces the MTAHVs, and their different configurations. Moreover, the advantages and limitations concerning their performance and design conflictions are discussed. Further, it highlights the motivation behind this research and novelty of the work conducted.

Chapter 2 presents a comprehensive literature review concerning the previous research conducted on ATS systems for MTAHVs. Furthermore, various fault tolerant diagnosis and identification techniques are discussed. Chapter 3 discusses the systems modeling and validation of the 4DOF linear vehicle model and the ATS Hydraulic Actuation (AHA) system model.

Chapter 4 establishes the FTC-ATS scheme. LQR and  $H^\infty$  controllers are synthesized and their effectiveness in enhancing system performance is discussed. Moreover, the effects of actuator dynamics are examined. Kalman Filter and Luenberger Observers are applied to design a fault diagnosis framework. Finally, a novel FTC scheme is developed and investigated using TruckSim vehicle model. Chapter 5 provides the conclusion and suggestions for future research work.

# **CHAPTER 2**

## **LITERATURE REVIEW**

### **2.1. Introduction**

This chapter aims at introducing the concepts of ATS, and FTC. In addition, it presents a comprehensive literature review concerning the previous research conducted on ATS and FTC. Furthermore, it discusses the control techniques employed for ATS implementation, and numerous FTC techniques.

### **2.2. ATS systems for MTAHVs**

Attaining reasonable low-speed maneuverability and high-speed lateral stability is a challenging task, as these characteristics leads to conflicting design features. To ensure optimal trade-off between low-speed and high-speed performance of MTAHVs, ATS has been proposed [6-8, 13]. Active trailer steering for a MTAHV consists of a one or more steerable axles located in the trailer(s), where closed-loop feedback control modulates the optimal steering input. The actuation occurs using hydraulic or electronic actuators.

The Multi-disciplinary Vehicle System Design Laboratory (MVSDL) research group at the University of Ontario Institute of Technology (UOIT) has conducted numerous studies to evaluate the efficacy of the ATS technique for enhancing the lateral dynamics of Articulated Heavy Vehicles (AHVs) [6-8, 10, 13, 28-30]. He and Islam presented an ATS design methodology for articulated heavy vehicles to achieve an optimal tradeoff between maneuverability and lateral stability [28]. Wang developed an ATS system for a MTAHV using a model reference adaptive control (MRAC) technique [7]. The MRAC technique

demonstrated enhanced lateral dynamics despite parametric uncertainties such as vehicle forward speeds and trailer payloads. Moreover, the system was analyzed using driver-hardware-in-the-loop (DHIL) real-time simulation [7, 29]. He and Islam published an integrated design method employing ATS to enhance the lateral stability and path following of AHVs [30]. Zhu developed a coordinated control strategy for MTHAVs employing Trailer Differential Braking (TDB), Active Roll Control (ARC) and ATS as active control techniques [6]. The research reinforced the superiority of the ATS technique in enhancing lateral stability. In another study, ATS was applied to an A-Train MTAHV and corroborated using Hardware-In-the-Loop (HIL) testing [10].

Cambridge Vehicle Dynamics Consortium (CVDC) developed an active steering system for a tractor-semitrailer combination. The proposed system enhances the path-following ability, by manipulating the steering angles of semitrailer axles, which allows the semitrailer's rear end to effectively follow the tractor's fifth-wheel's trajectory [32]. The strategy improves maneuverability and reduces tire scrubbing at low-speeds, while improving stability and dynamic response of the vehicle at high-speeds. Cheng et al. [33] proposed an ATS controller for a tractor-semitrailer combination to augment the vehicle's path-following ability in low-speed maneuvers and improved roll stability in transient maneuvers. Cheng and Cebon implemented ATS using the LQR control technique for optimizing the roll stability and path following ability of articulated heavy vehicles by minimizing a combination of the path-tracking deviation and the lateral acceleration of the semitrailer [34].

Rangavajhula and Tsao developed an active trailer steering system for articulated heavy vehicles to improve the low-speed stability and path following off tracking [35-36]. Kyong-il kim et al. developed an active steering controller for a tractor-trailer configuration based on the LQR control theory. The controller was designed to follow the desired yaw rate and minimize the vehicle's side-slip angle simultaneously. Results illustrate significant improvements in the vehicle's low-speed maneuverability and high-speed stability [37].

Abroshan et al. suggested a combined fuzzy logic and PID based controller for an automated-steering articulated vehicle. The proposed vehicle aimed at reducing low-speed off tracking by implementing steerable axles for both tractor and trailer. Moreover, the tractor and trailer were independently controlled. The simulation results indicate enhanced maneuverability with accurate path following [38].

ATS systems have the ability to enhance both the low-speed and high-speed performance of AHVs. However, physical implementation of such systems entails substantial costs. Moreover, ATS is a complex array of numerous sub-systems. Generally, an ATS system consists of a modified steering axle, a hydraulic actuator, fluid reservoir, a hydraulic power supply, a control valve and ancillary systems such as accumulators, locking mechanisms and so on [39]. Moreover, it requires a complex control architecture to facilitate smooth interaction between these components. Hence, ATS systems have had limited commercial applications, and so far most systems have been applied using the numerical simulation environment.

Although few commercial ATS systems exist [39], they are primarily designed for single unit vehicles such as trucks, and tractor-semitrailers. Commercial ATS systems for MTAHVs are very rare. Moreover, compared to single unit vehicles, ATS systems for MTAHVs are more expensive. The primary reason being the augmented complexity of such vehicle configurations. Hence, practical implementation of ATS in MTHAVs has been restricted to prototype vehicles [39].

In 2010, Odhams et al. [39] implemented a physical ATS system in a B-Train double. The study employed the CT-AT-AT (Conventional Tractor-Active Trailer-Active Trailer) control strategy to improve steady-state off tracking and trailer sway simultaneously. Moreover, the vehicle's performance was evaluated during both forward and reverse motion. Results suggest that ATS can significantly improve the vehicle's dynamic behavior. Specifically for MTAHVs, ATS is essential to allow sufficient maneuverability [39]. Although a physical ATS system is complex and involves high implementation costs, such costs may be justifiable considering the numerous benefits offered by such systems.

### **2.3. Control Techniques for ATS**

Numerous control techniques have been investigated for implementing ATS systems including Proportional Integral Derivative (PID) [40], LQR [6-8, 10, 13, 28-36],  $H^\infty$  [10, 41], Sliding Mode Control (SMC) [6, 42-43] and Fuzzy Logic control [38, 44-45]. This section discusses the most commonly applied ATS control scheme, i.e. LQR, followed by a comprehensive literature survey of  $H^\infty$  based controllers employed in vehicle dynamic control.

### **2.3.1. LQR Control**

LQR based ATS control systems have been widely investigated [6-8, 10, 13, 28-36]. Predominantly, LQR based ATS systems have been applied to enhance the lateral stability and maneuverability of articulated vehicles [31, 46-47]. Such systems aid in achieving optimal trade-off between vehicle's maneuverability and lateral stability [28].

LQR based controllers exhibit superior performance in comparison to other traditional control strategies, such as PID [7, 24]. They employ full-state feedback to stabilize the system. Moreover, such controllers are comparatively straightforward to synthesize [7]. Therefore, LQR based controllers are widely implemented to optimize and stabilize active systems.

Despite their widespread application(s), LQR based controllers exhibit certain robustness concerns. In the presence of system uncertainties and external disturbances, they are unable to regulate complex systems [7, 24, 48]. Specifically, LQR based controllers fail to compensate the discrepancies between the system model and the real system, and the presence of noise [48]. Therefore, for controlling a complex system such as a MTAHV, it is vital to adopt a robust control technique that can achieve optimal performance despite system uncertainties. Controllers based on the  $H^\infty$  technique are considered robust [50]. The  $H^\infty$  technique is considered superior compared to the LQR control technique, which may not always ensure robustness [51].

### 2.3.2. $H^\infty$ Control

Robustness is a crucial design criteria considered while designing controllers.  $H^\infty$  based controllers exhibit robustness against system uncertainties while guaranteeing system stability and noise rejection [50]. Moreover, the  $H^\infty$  technique handles the model uncertainties, un-modeled dynamics and the disturbances in the system effectively [52]. Ever since its advent in 1980s [53], the  $H^\infty$  technique has been regarded as a powerful tool for handling complex uncertain systems [50].

In vehicle control studies, the  $H^\infty$  technique is utilized extensively. However, most of the research conducted so far has been limited to single unit vehicles. So far, the  $H^\infty$  technique for ATS systems in articulated heavy vehicles has received little consideration [6].

Horiuchi et al. [54] suggested an active steering control strategy for a four-wheel steering (4WS) vehicle using a 2DOF (feedback and feedforward)  $H^\infty$  control system. The control system was designed to track the vehicle's desired yaw rate and lateral acceleration responses. The feedback controller was incorporated to enhance the system's robustness, whereas the feedforward controller was employed to ensure accurate reference following while minimizing the control signals. The proposed controller was installed on a test vehicle and good referencing tracking was observed. Another  $H^\infty$  based controller was proposed for a 4WS vehicle [55]. The control objective was to reduce the peak values of yaw rates, lateral accelerations and sideslip angles under high-speed maneuvers. The 4WS demonstrated preferable behavior of the three performance measures [55].

In 2013, Zhao et al. [56] designed a  $H^\infty$  based controller for an active front steering (AFS) system. The control objective was to ensure robust performance and stability, while maintaining adequate steering feel [56]. Simulation results revealed that the proposed  $H^\infty$  controller delivers enhanced performance and stability.

Generally, road vehicles experience large parametric uncertainties. Linear parameter-varying (LPV)  $H^\infty$  methods are suitable for systems with large uncertainties [50]. Güvenç et al. [57] developed a 2DOF  $H^\infty$  steering controller for improving a passenger car's yaw dynamics by applying the LPV  $H^\infty$  technique. Moreover, the controller was gain scheduled using a combination of different forward speeds and road-adhesion coefficients. The traditional front steering mechanism was integrated with an auxiliary-steering actuation system to provide driver assistance. Control system was designed to permit the driver to perform low frequency driving and to impart corrective action only when necessary [57]. Linear, nonlinear and HIL simulations were performed to establish the control system's efficacy. Pushkar et al. [58] proposed a LPV  $H^\infty$  based controller for implementing automated lane keeping in a tractor-trailer combination. The study emphasized the benefits of linear control techniques. Linear controllers offer ideal tradeoff between steering action, passenger comfort, robustness and tracking performance [58].

Chen et al. [59] proposed an adaptive fuzzy elimination based  $H^\infty$  technique. The  $H^\infty$  control strategy was applied in a wheeled robot vehicle system to achieve robust tracking performance, despite the presence of parametric uncertainties and external disturbances [59]. In 2014, Sun and Yan developed a

robust  $H^\infty$  fuzzy control design method for a virtual truck-trailer combination. The controller was evaluated using the Lyapunov function for a non-linear system. [60].

A robust fault tolerant  $H^\infty$  based controller was suggested for active suspension systems [61]. According to the study, the controller synthesis considers presence of actuator faults and external disturbances. Moreover, suspension deflection and actuator saturation were included. System performance was investigated using a full car model [61].

## **2.4. Fault Tolerant Control (FTC)**

### **2.4.1. Introduction**

A “fault”, within a plant, is defined as the aberration of system characteristics and performance parameters [25]. In the event of a fault occurrence, the interaction between the different components and sub-systems is hampered, which can lead to erroneous feedback and loss of system functions. Examples of such faults include actuator failure, the loss of a sensory information etc. [25].

It is imperative to detect “faults” timely and stop their propagating effects in an aim to avoid the deterioration of the system performance or any damage to exposed machines [25]. Effectively controlled measures should be taken in order to make the system fault tolerant. FTC is mainly concerned with the interaction between the system and the controller. If the system exposed to faults comprises of a control algorithm that is capable of adapting to the faulty plant after a short interval of noted degraded performance, such systems are fault tolerant [25].

A fault tolerant controller includes feedback and feedforward control law, and a decision-making layer that regulates the controller's configuration. FTC analyses the behavior of the plant, identifies faults in the system, and accordingly reconfigures the control law to ensure acceptable closed-loop system performance [25].

Control systems are intended for regulating an error-free plant, where the criteria are to meet the performance requirements using closed-loop feedback [25]. FTC systems, however, take into account the scenario where some faults can occur in the plant, which may degrade the robustness of the system and cause systems failures. In other words, a fault tolerant controller can detect the existence of a fault within the plant and respond to counteract or diminish the faulty behavior within the plant.

#### **2.4.2. Approaches to FTC**

FTC is classified into two categories, namely active and passive FTC. Active FTC responds to occurrence of fault in real-time [25, 62-64, 66]. Although the performance of the plant might degrade during fault occurrence, its functionality remains within acceptable limits. Active FTC scheme comprises of two key stages, namely Fault Detection and Diagnosis (FDD) and Control-loop Reconfiguration. FDD is responsible for detection of faults that may occur in the plant, whereas the latter is responsible for adjusting the control loop to maintain the plant's functionality [25]. In order to execute these steps, a supervision system is employed which supervises the FDD and actively regulates the control loop [25].

An alternative approach towards FTC is Passive fault tolerance. Passive FTC works only on predefined failure modes. In this FTC strategy, the design is fixed and the control loop can only adapt to faults that have minor effects on the plant's performance [25, 62-64].

Physical and analytical redundancy are the two primary methods employed in FTC systems. Physical redundancy method employs additional redundant components, such as additional sensors and actuators, to ensure fault tolerance. Fault diagnosis is performed through limit checking or spectral analysis of selected signals. If a fault is diagnosed, the controller switches to a redundant component. Due to the unreasonably high complexity and cost, such methods are predominantly applied to safety-critical systems [25]. Moreover, physical redundancy method demands a specific measurable signal to indicate fault occurrence of every fault possible in the system. In complex systems, specific signals pertaining to every possible fault cannot be generated. In addition, it is expensive to measure all such signals [25].

Hence, the analytical redundancy method, better known as model-based FTC, is preferred, where mathematical models are utilized to perform fault tolerant control [25]. Fault diagnosis is performed by comparing the actual output measurements to its mathematical model. The system adapts to the faulty situation such that the closed-loop system satisfies the expected performance criteria. Model-based FTC is computationally efficient and less expensive in comparison to the physical redundancy method [25].

### **2.4.3. FTC in ATS systems**

So far, FTC has been primarily employed in the aerospace industry. Modern airplanes rely on FTC and it is indispensable in Space travel. FTC in vehicle systems control and design is an emerging research discipline. The advance in modern technology and technical processes has created a demand for enhanced system performance and safety [27]. Since FTC is directly concerned with safety and reliability of systems, fault tolerant strategies have become critical [63, 64]. Furthermore, the upsurge towards integrated control has led to augmented complexity, which dictates stringent requirements for the control architecture [63]. In addition to smart actuators, sensors and FTC, reliable communication architecture is required to achieve a dependable fault tolerant system [63].

Being an emerging technology in the automotive industry, fault tolerance of ATS systems has received negligible consideration. So far, most commercial ATS systems only consider certain “fail-safe” modes, where the active system is shut down in case of a failure. In certain commercial systems, the active axles are “locked” at high-speeds, by using a mechanized locking mechanism [65]. Few ATS technologies are equipped with self-centering devices, which allow the active axle(s) to return to an “unsteered” configuration during fault occurrence [65]. Whereas, other ATS systems employ additional actuators to allow redundancy in the system during particular failure scenarios. Since an ATS system significantly alters the vehicle’s dynamics, it is imperative to investigate all aspects of the system, particularly, under faults, and failure scenarios. So far, very few studies have investigated this aspect of ATS systems, one such study is discussed below.

Odhams et al. [65] investigated the dynamic safety of an ATS system for a tractor-semitrailer. The study focused on specific issues associated primarily with the safety systems. The application of safety system(s) (for e.g. axle's centering system) under dynamic fault conditions was studied. Moreover, the influence of the safety system's intervention on the vehicle's dynamic behavior was examined, such as the rapid centering of the axles during an emergency maneuver, which may result in high lateral acceleration and render the vehicle susceptible to rollover. Furthermore, the performance of the ATS system was evaluated under external disturbances, such as wind gusts and split-friction braking. The ATS system featured dedicated sensors for performance monitoring [65].

## **2.5. FTC Tools and Techniques**

### **2.5.1. Model-based FDD Methods**

FDD is an integral part of the FTC framework. So far, numerous FDD techniques have been developed to ensure safe and reliable performance of complex systems [63, 64, 66-70]. As discussed in the Section 2.4.2, these techniques can be categorized into physical and analytical redundancy techniques. Considering the benefits of the latter, this research focuses on developing a FDD framework by employing analytical redundancy or model-based fault detection techniques.

Isermann [68] defines parameter estimation, observer and state estimation and parity equations as the primary methods for model-based fault detection. Parameter estimation method can diagnose multiplicative faults within the system. Multiplicative faults occur due to parametric variation and tend to alter the system's dynamics. A comparison of reference parameters and estimated parameters can

indicate fault occurrence and fault magnitude. Moreover, this method is suitable for discrete time and multi-input-multi-output (MIMO) systems [68]. Since online estimation of parameters is challenging and expensive, data acquired from the parameter estimation approach is extremely valuable [68]. However, Jeppensen and Cebon [70] suggest that parameter estimation method is more suited for diagnosing non-safety critical and slow-acting faults, such as faults that occur due to wear.

By employing observer and state estimation method, a comprehensive fault detection and diagnosis framework can be created. Moreover, it allows detailed modeling of faults by distinguishing multiplicative and additive faults. However, this method relies heavily on the accuracy of system model and parameters. Isermann [68] further classifies observer and state estimation method into five categories. The first is termed as dedicated observer scheme [68], where each observer is defined by one output. This method permits detection and diagnosis of multiple sensor faults. In the second scheme, known as the generalized observer scheme, observers are defined using all but one measurements. This method is more robust as it can observe multiple sub-systems simultaneously [68-70]. In the third scheme, observers are defined using all measurements. The fourth employs Kalman filters to detect stochastic changes in the system. In the last scheme, fault detection filters are specifically synthesized to allow detection of faults [68].

Parity equations method is applicable for additive faults [68]. Similar to observer and state estimation method, this method requires a reference model to predict faulty behavior. However, it is comparatively easier to implement [68].

Observer and state-estimation methods are extensively used to create effective and reliable FDD systems. Most model-based FDD methods, including the observer and state-estimation method, employ residual signal generation for fault detection [66-70]. A residual signal represents the error between estimated value and measured values. Specifically, it detects the underlying discrepancies in the real system by means of comparison with a reference model [69, 70]. Ideally, the residual should be zero during nominal operating conditions, but large in the presence of faults [70].

Observed-based FDD involves estimating the output from the available measurements and creating residuals through weighted output estimation errors [71]. You et al. [72] suggest that current observer-based FDD techniques are ill equipped to deal with both sensors and actuators faults. Sensor faults reduce the system's observability by losing reliable measurement information, whereas actuator faults affect the ability to control the system through one of the actuators [71]. Although an ideal FDD framework must diagnose both sensors and actuator faults, most studies assume that either actuators or sensors are at fault [72]. Effective fault diagnosis of multiple components and system generally necessitates a combination of multiple observers, such as yaw rate versus lateral acceleration sensors [66, 72]. Besides a single observer can only perform fault detection but not diagnosis. Even though reducing the number of observers leads to a less complex and computationally efficient FDD scheme [72], using multiple observers seems to be the more promising approach for model-based fault detection techniques [72].

Fault diagnosis involves isolating the faulty component (sensor or actuator) [70]. This can be a challenging task. Hence, to facilitate a robust fault diagnosis framework, certain assumptions are made. It is assumed that all possible faults are already considered while designing the diagnosis system. Moreover, it is assumed that only one fault occurs at a time [68-70].

An observer estimates the states of a system using known input and output measurements. Generally, observers are employed to estimate a system's states, which are difficult to measure with conventional sensors, e.g. flame temperature of a jet engine's exhaust. However, in the FDD framework they provide analytical redundancy for some sensors. As previously discussed, observer-based FDD methods utilize residuals to generate fault indicator(s). Fault indicators are further processed to determine the occurrence, magnitude and location of faults. The following sections discuss the fundamental observer and state estimation techniques, Luenberger Observer and Kalman Filter. Moreover, it presents a literature survey of their applications.

### **2.5.2. Luenberger Observer**

Luenberger Observers can approximate missing information about the system's states [73]. They are generally applied to deterministic continuous-time systems [73]. Numerous studies have utilized Luenberger Observers to develop FDD schemes [71, 74-76]. Hu et al. [74] developed an adaptive Luenberger observer-based technique for online estimation of the battery pack's State of Charge (SoC) in an electric vehicle. The study featured adaptive regulation of observer gain. The results affirmed the observer's capability to estimate the battery pack's SoC [74].

Ibaraki et al. [75] proposed a fault detection filter based on the Luenberger Observer for the lane-keeping control systems of automated intelligent vehicle highway systems (IVHS). The Luenberger Observer was designed using the  $H^\infty$  loop-shaping methodology. To satisfy robustness requirements, the observer was retuned using constraints defined on the frequency components of the residual. Moreover, results indicated that frequency shaping of residual signals aid in reducing missed detection and false fault detection rates [75].

Cherouat et al. [76] presented an algorithm to observe the vehicle's sideslip angle and the yaw rate using rotational wheel speeds and lateral acceleration measurements. The study employed a Luenberger Observer based on a nonlinear passenger car model. Additionally, a Lyapunov function was used to synthesize and stabilize the observer. Simulation results depicted excellent agreement between the predicted and actual measurements of vehicle's sideslip angle and yaw rate [76].

### **2.5.3. Kalman Filter**

Kalman Filters are widely applied because of their ability to handle both stochastic and deterministic systems. Moreover, in the presence of noise, they exhibit superior estimation performance. Since their introduction in 1960 [77], Kalman Filters have shown wide-ranging applications [78-81]. The Apollo Moon Landings Project utilized a Kalman Filter to aid navigation by estimating the spacecraft's trajectories while travelling in space [78]. However, the following discussion is restricted to use of Kalman filters in vehicle dynamics control, where they are employed as an estimator to predict system states.

Sivashankar and Ulsoy [79] proposed a novel approach to accurately measure vehicle's yaw rate using a steering angle sensor and two accelerometers. The study aimed at providing an inexpensive alternative to commercial yaw rate sensors. Since accelerometers generally produce noisy measurements, the suggested method involved a combination of the kinematic and dynamics estimates of yaw rate to predict vehicle's true yaw rate. The kinematic estimate was calculated by using the measurements from the two accelerometers located on left and right side of the vehicle's CG, whereas the dynamic estimate involved a linear vehicle model coupled with a Kalman Filter. The combined approach optimally weighted the combined estimation based on the sensor noise characteristics and employed a gain scheduled filter to compensate for vehicle's forward speed [79]. The proposed method was analyzed using linear and nonlinear vehicle models. Moreover, sensor noise data were recorded on an actual vehicle. Results indicated that the method effectively predicts yaw rate in presence of system noise and could be an excellent alternative to conventional yaw rates sensor. Furthermore, the authors suggested that by fine-tuning the Kalman Filter, employing gain scheduling, and defining tire operational limits, extremely accurate yaw rate estimation is possible [79].

Venhovens and Naab [80] explored the effectiveness of Kalman Filter in driver assistance systems and vehicle dynamics estimation. They proposed implementation of Kalman Filter in the vehicle's adaptive cruise control system. The suggested method predicted the position of the relevant targets, thereby assisting the adaptive cruise control system to avoid any collisions [80].

Authors further evaluated Kalman filter's performance during lane-keeping control. To devise a control strategy, disturbances to lane-keeping, such as cross-winds or road super-elevation, were modeled as additional steering inputs. Since steering input is proportional to yaw rate, any steering input that does not produce yaw motion would be caused by external disturbances [80]. By means of a Kalman Filter and a linear vehicle model, the strategy could predict magnitude of external disturbances, which would otherwise be very difficult to measure. Furthermore, they demonstrated vehicle's yaw rate estimation using Kalman Filter. Yaw rate was estimated by using noisy rotational wheel speed measurements. Moreover, to compensate for change in wheel speeds due to tire slip angles, the study presented a first-order transient tire model [80]. Additionally, a technique for estimating front-axle's lateral velocity using wheel speeds was presented. Kalman Filter demonstrated reasonable results in all applications.

In 2013, Emirler et al. [81] proposed a technique for estimating a vehicle's yaw rate using a virtual sensor. The virtual sensor contained kinematic estimates of yaw rate and a forward-speed scheduled Kalman Filter. Kinematic yaw rate estimates were computed using rotational wheel speeds, dynamic tire radius, and steering angle measurements, whereas the Kalman Filter utilizing a linearized car model with speed-based gain scheduling [81]. Hardware-in-the-loop simulation was performed and the virtual sensor successfully estimated the yaw rate. Additionally, the simulation results were corroborated with actual road testing data to demonstrate the effectiveness of the virtual sensor by comparing the estimated yaw rate from the virtual sensor with the actual yaw rate of the vehicle [81].

## **2.6. Summary**

MTAHVs are vital to the trucking industry. Hence, to ascertain their widespread application, it is essential to address certain concerns related to their safety and stability. ATS systems provide the necessary solution to address these concerns. As discussed in this chapter, ATS systems have enabled noteworthy improvement in low-speed maneuverability and enhanced high-speed lateral stability for MTAHV. Since an ATS system significantly influences the stability and dynamic characteristics of MTAHV, it is essential to ensure its safe operation. Similar to most industrial systems that requires heavy load requirements, ATS systems employ hydraulic actuation systems. Hydraulic systems can experience sudden failure due to oil leakage, chattering, sensor failure and so on. This mandates the need of a fault tolerant control strategy, which is capable of detecting impending failure(s) and able to regulate the system to maintain functionality. Such a system ensures the safety of the physical system by performing continuous monitoring and diagnosis of possible faults.

This chapter reviewed numerous applications of FTC with a specific focus on vehicle dynamics. Although the literature advocates the usability of such systems, real life applications of FTC in vehicle dynamics, particularly for heavy vehicles is limited. Most studies are based on numerical simulations. Even though such approaches have produced deep insights into the usability of FTC, the complications faced by actual hardware and signals must be addressed before model-based FTC schemes are widely adopted.

# **CHAPTER 3**

## **VEHICLE SYSTEMS MODELING and VALIDATION**

### **3.1. Introduction**

Physical systems are inherently nonlinear. Unlike a linear system, nonlinear systems do not exhibit proportionality between the change of input and the change of output. Moreover, it is difficult to capture all the complex nonlinear dynamics while defining a system model. Therefore, modeling a non-linear physical system is a challenging task. Although incorporation of nonlinear elements in a model enhances its accuracy, it substantially decreases the computational efficiency. Thus, for applications such as controller synthesis, stability analysis and parameter optimization highly complex models are simplified and linearized around predefined operating points. Moreover, most control strategies necessitate the use of linear models. Simplified linear models usually include the salient dynamic features of the system.

Despite their advantages, simplified linear models can lead to low fidelity [3]. Hence, the accuracy of such models is established by comparing their responses with those of high fidelity modeling software in standard test conditions. In this chapter, a linear model for the B-Train double is developed and validated using TruckSim software package. Moreover, a hydraulic system model for the ATS is developed. Modeling the hydraulic control system is necessary to develop fault diagnosis strategies, and to analyze the effects of actuator dynamics on the closed-loop system. The hydraulic system model is validated using MathWorks Simscape software.

### 3.2. Linear Yaw-Plane Model

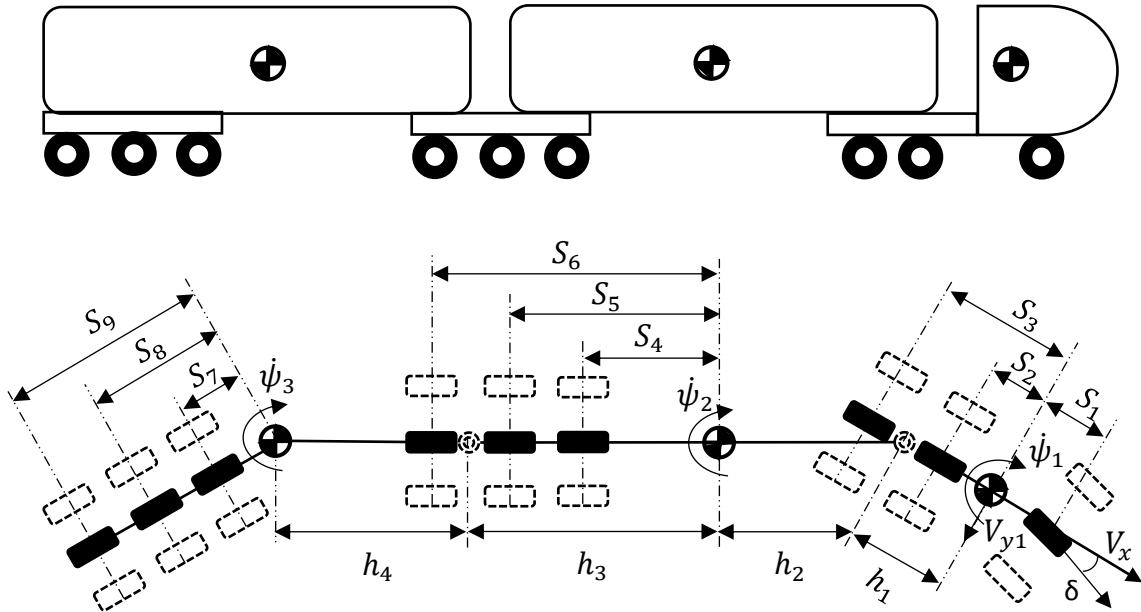


Figure 3.1 Configuration of the linear B-Train double model.

Fig. 3.1 displays the linear yaw-plane model representing the B-Train double. The system has been telescoped laterally, where a single tire represents each axle. The linear vehicle model consists of 4 Degrees of Freedom (DOF), where the considered motions include lateral velocity  $V_{y1}$ , and yaw rate  $\dot{\psi}_1$ , of the tractor, the yaw rate  $\dot{\psi}_2$ , of the first trailer, and the yaw rate  $\dot{\psi}_3$ , of the second trailer.

In order to derive the linear 4DOF model, the following assumptions are made [83]:

- The forward speed of vehicle is constant. In addition, the forward speeds of vehicle units ( $V_{x1}$ ,  $V_{x2}$  and  $V_{x3}$ ) take the same value.
- The tractor steering angle  $\delta$  is small
- The articulation angle between the vehicle units is also small.
- The tire slip angles are small and show linear relationship with lateral tire forces

- The aerodynamic forces, rolling and pitching motions and longitudinal forces between tire and road have been ignored.

The governing equations of motion for the vehicle system are derived using the body fixed coordinate system. Based on Newton-Euler equations of motion, the governing equations of motion for the B-Train double can be written as follows.

The equations of motion of the tractor are expressed as,

$$m_1(\dot{V}_{y1} + V_{x1}\dot{\psi}_1) = F_{y1} + F_{y2} + F_{y3} - F_{h1} \quad (3.1)$$

$$I_1\ddot{\psi}_1 = S_1F_{y1} - S_2F_{y2} - S_3F_{y3} + h_1F_{h1} \quad (3.2)$$

The equations of motion of the first trailer are cast as,

$$m_2(\dot{V}_{y2} + V_{x2}\dot{\psi}_2) = F_{y4} + F_{y5} + F_{y6} + F_{h1} - F_{h2} \quad (3.3)$$

$$I_2\ddot{\psi}_2 = -S_4F_{y4} - S_5F_{y5} - S_6F_{y6} + h_2F_{h1} + h_3F_{h2} \quad (3.4)$$

The equations of motion of the second trailer are formulated as,

$$m_3(\dot{V}_{y3} + V_{x3}\dot{\psi}_3) = F_{y7} + F_{y8} + F_{y9} + F_{h2} \quad (3.5)$$

$$I_3\ddot{\psi}_3 = -S_7F_{y7} - S_8F_{y8} - S_9F_{y9} + h_4F_{h2} \quad (3.6)$$

The lateral motion of the articulation points is subjected to kinematic constraints defined as,

$$\dot{V}_{y2} + h_2\ddot{\psi}_2 = \dot{V}_{y1} - h_1\dot{\psi}_1 + V_{x1}\dot{\psi}_1 - V_{x2}\dot{\psi}_2 \quad (3.7)$$

$$\dot{V}_{y3} + h_4\ddot{\psi}_3 = \dot{V}_{y2} - h_3\dot{\psi}_2 + V_{x2}\dot{\psi}_2 - V_{x3}\dot{\psi}_3 \quad (3.8)$$

The linear relationship between the lateral forces and slip angles is defined as,

$$F_{yi} = -C_i \alpha_i, \quad i = 1, 2, 3, \dots, 9. \quad (3.9)$$

$$\begin{cases} \alpha_1 = \frac{V_{y1} + S_1 \dot{\psi}_1}{V_{x1}} - \delta \\ \alpha_2 = \frac{V_{y1} - S_2 \dot{\psi}_1}{V_{x1}} \\ \alpha_3 = \frac{V_{y1} - S_3 \dot{\psi}_1}{V_{x1}} \end{cases} \quad (3.10)$$

$$\begin{cases} \alpha_4 = \frac{V_{y2} - S_4 \dot{\psi}_2}{V_{x2}} \\ \alpha_5 = \frac{V_{y2} - S_5 \dot{\psi}_2}{V_{x2}} \\ \alpha_6 = \frac{V_{y2} - S_6 \dot{\psi}_2}{V_{x2}} \end{cases} \quad (3.11)$$

$$\begin{cases} \alpha_7 = \frac{V_{y3} - S_7 \dot{\psi}_3}{V_{x3}} \\ \alpha_8 = \frac{V_{y3} - S_8 \dot{\psi}_3}{V_{x3}} \\ \alpha_9 = \frac{V_{y3} - S_9 \dot{\psi}_3}{V_{x3}} \end{cases} \quad (3.12)$$

Since velocities of the fifth-wheels must be comparable, the reaction forces  $F_{h1}$  and  $F_{h2}$  can be eliminated. The 4DOF B-Train double model is expressed in the state space form as,

$$\dot{x}(t) = Ax(t) + Bu(t) \quad (3.13)$$

$$x = [V_{y1} \dot{\psi}_1 \quad V_{y2} \dot{\psi}_2 \quad V_{y3} \dot{\psi}_3]^T \quad u = [\delta]^T \quad (3.14)$$

where, **A** and **B** matrices are provided in Appendix B.

### 3.3. Model Validation

#### 3.3.1. Non-linear TruckSim Model

The linear 4DOF vehicle model described in Section 3.2 is subject to certain assumptions. For example, the 4DOF model assumes that a linear relationship exists between tire slip angles and lateral forces, (see Eq. (3.9)). Moreover, vehicle motions such as roll and pitch are neglected. Hence, to ascertain the reliability of the 4DOF model, the model is validated using the high-fidelity nonlinear TruckSim software package. TruckSim has been developed using real-world experimental data [83]. This sub-section briefly discusses the configuration and the functioning of the TruckSim software package.

TruckSim is primarily based on the multi-body program VehicleSim (VS) Lisp [83]. VS Lisp generates the equations of motion for the 3D multi-body vehicle systems. Input to VS Lisp is the geometric description of the vehicle configuration, such as the DOF(s), the point locations, force vectors and so on. Thereafter, VS Lisp derives the equations of motion and simultaneously solves those equations [83].

In TruckSim, the B-Train double can be defined as  $S\_SS+SSS+SSS$ , where S indicates a solid axle, an underline (  ) signifies a separation of axle groups and a plus sign (+) denotes a fifth-wheel connecting the two vehicle units [83]. Thus, as the configuration indicates, the B-Train double consists of a tractor having one front axle and two rear axles, and two semitrailers consisting of three solid axles (see Fig. 3.2). Fig. 3.3 illustrates the user interface of the TruckSim software.



Figure 3.2 Configuration of the B-Train double.

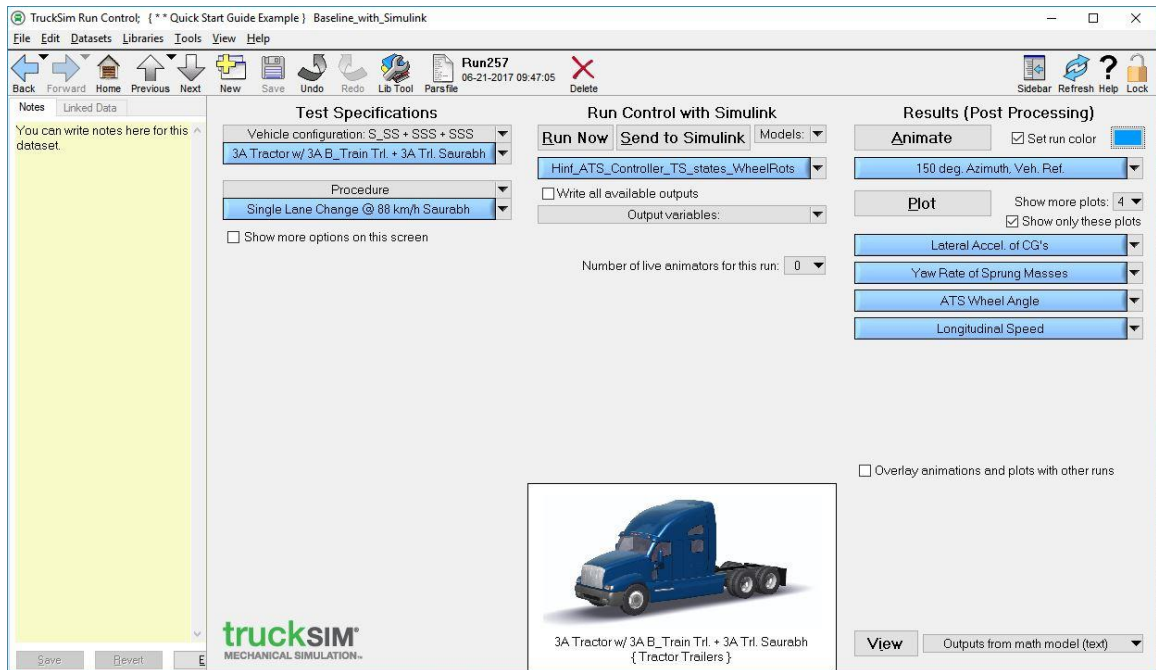
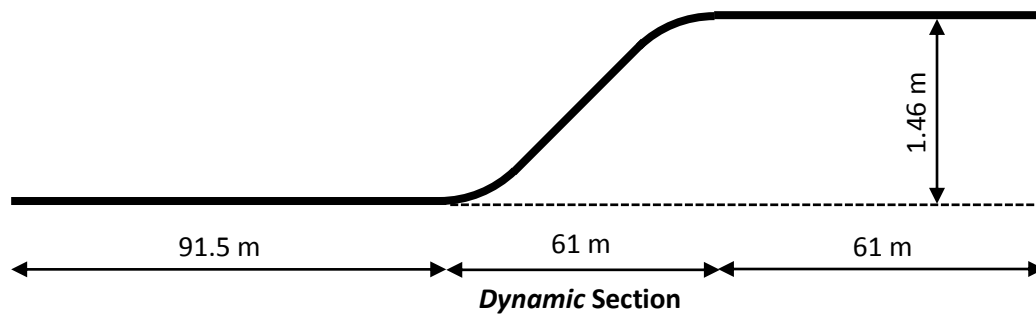


Figure 3.3 TruckSim's User Interface (Run Control Screen)

### 3.3.2. Test Maneuvers for Model Validation

Generally, the lateral dynamics of MTAHVs is evaluated using open-loop and closed-loop simulations. In open-loop tests, the steering input is fixed and independent of the vehicle's response, whereas in closed-loop tests, the driver (or virtual driver model) constantly corrects the steering input to ensure that the vehicle follows the designated path [83]. Open-loop tests are usually preferred for model validation.



Note: Not drawn to scale.

Figure 3.4 Schematic representation of the single lane change maneuver specified by SAE J2179 [84].

In this research, two open-loop tests are simulated to validate the 4DOF linear B-Train double model. The first test is a high-speed single lane-change (SLC) maneuver based on the maneuver specified by SAE J2179 [84]. In this procedure, the forward speed of the vehicle is a constant 88 km/h and the lateral displacement is 1.46m. The comparative analysis of the 4DOF model and the TruckSim model is performed exclusively for the dynamic section as shown in Fig. 3.4.

The steering input for this simulation is a single cycle sine-wave defined as,

$$\begin{cases} \delta(t) = A \sin(2\pi ft) \\ \delta_{st}(t) = i_{st} \delta(t) \end{cases} \quad (3.15)$$

where,  $\delta$  is the steering angle of the front axle,  $A$  the amplitude, and  $f$  the frequency,  $\delta_{st}$  the steering wheel angle, and  $i_{st}$  angular ratio of the steering system. Frequency of the steering input is 0.4Hz, and amplitude  $A$  is tuned to ensure the vehicle has the specified lateral displacement of 1.46m.

Likewise, the second validation test is a SLC maneuver. However, the steering input frequency is 0.2Hz and the amplitude 35.52 degrees [83]. Fig. 3.5 illustrates the steering wheel angles for the two SLC maneuvers. Here, the angular ratio of the steering system is 25.

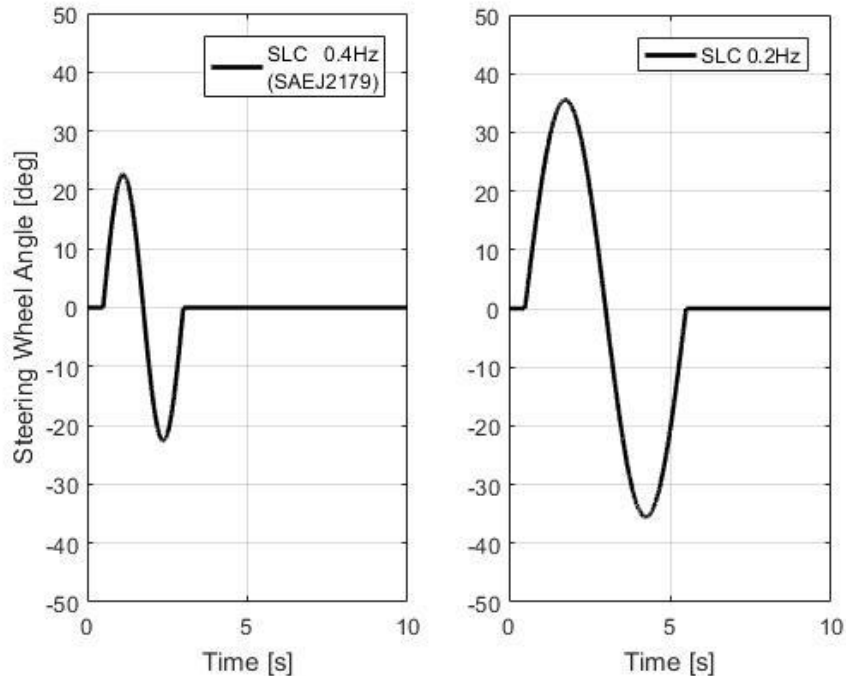


Figure 3.5 Time history of Steering Wheel Angles for the 1<sup>st</sup> SLC and the 2<sup>nd</sup> SLC maneuvers.

### 3.3.3. Model Validation Results

The 4DOF model is validated by comparing the vehicle model's lateral dynamic responses with the TruckSim data. To establish the validity, lateral acceleration and yaw rate are compared.

Fig. 3.6 and 3.7 show the time history of lateral acceleration of the 4DOF and the TruckSim models under the SLC test maneuvers. The three distinct curves signify the three vehicle units, the tractor, the first trailer and the second trailer. Altogether, the figures display reasonable agreement between the 4DOF and TruckSim models. However, notable variation exists in the negative peak lateral acceleration for the 1<sup>st</sup> test maneuver. This variation may be a result of the nonlinearity of the TruckSim model. Lateral acceleration curves under the 2<sup>nd</sup> test maneuver, however, show excellent agreement while attaining peak acceleration, and overall transient response.

Yaw rate response of the 4DOF and TruckSim models under the two test maneuvers exhibit similar results. Fig. 3.8 shows good agreement between the 4DOF and TruckSim models despite the variation observed between the yaw rates of the second trailer. The 4DOF linear model cannot predict the spike in second trailer's yaw rate caused due to the sudden lane change maneuver. The yaw rate response for all three units under the 2<sup>nd</sup> test show close responses between the 4DOF and TruckSim models (see Fig. 3.9). The results help establish the validity of the 4DOF model.

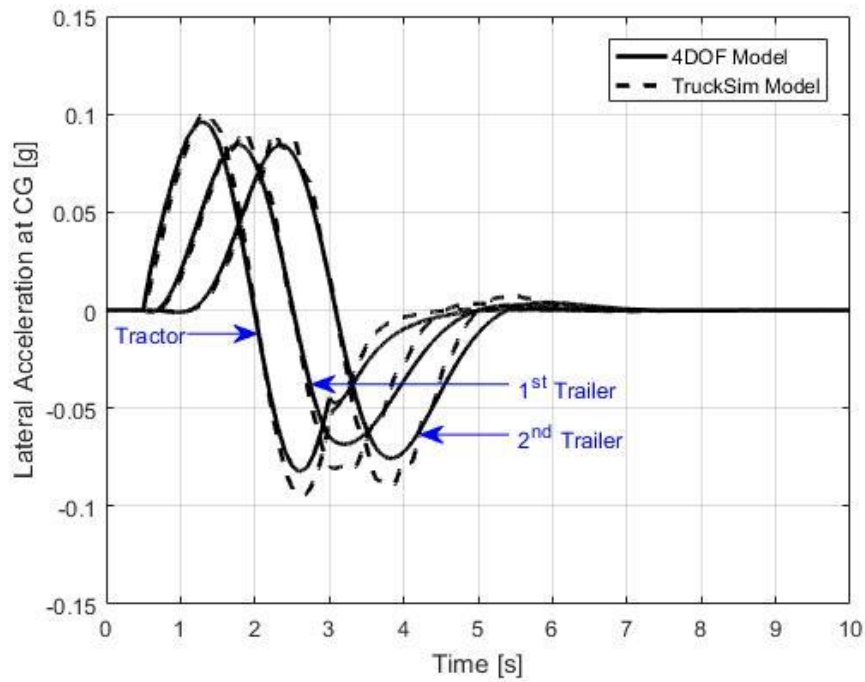


Figure 3.6 Time history of lateral accelerations of the 4DOF model and the TruckSim model under the 1<sup>st</sup> SLC test maneuver.

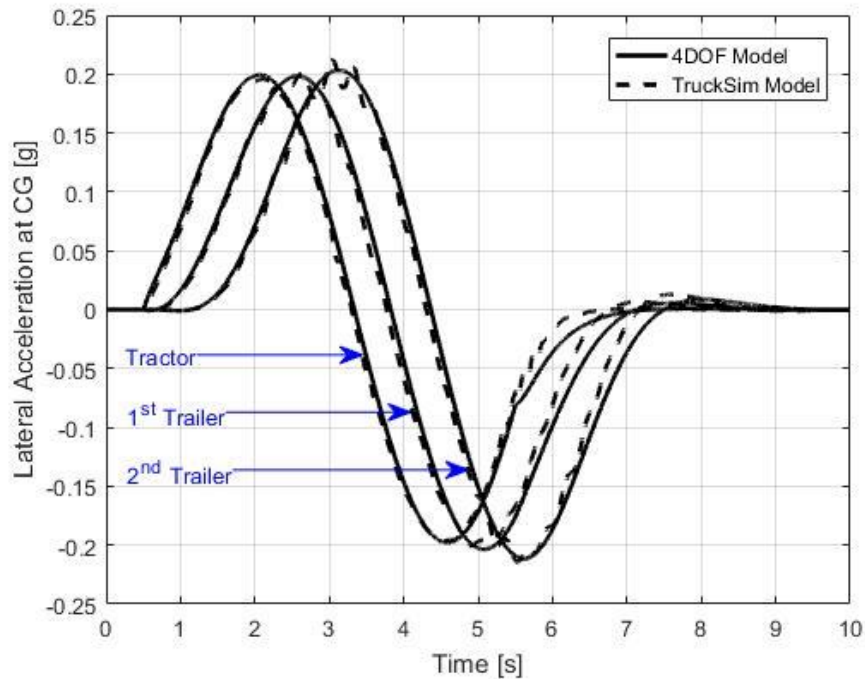


Figure 3.7 Time history of lateral accelerations of the 4DOF model and the TruckSim model under the 2<sup>nd</sup> SLC test maneuver.

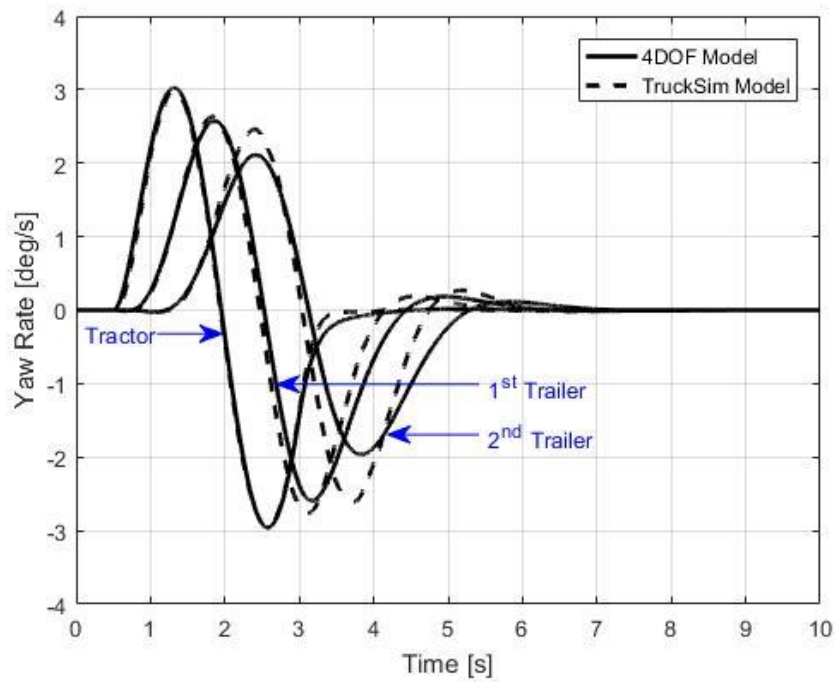


Figure 3.8 Time history of yaw rates of the 4DOF model and the TruckSim model under the 1<sup>st</sup> SLC test maneuver.

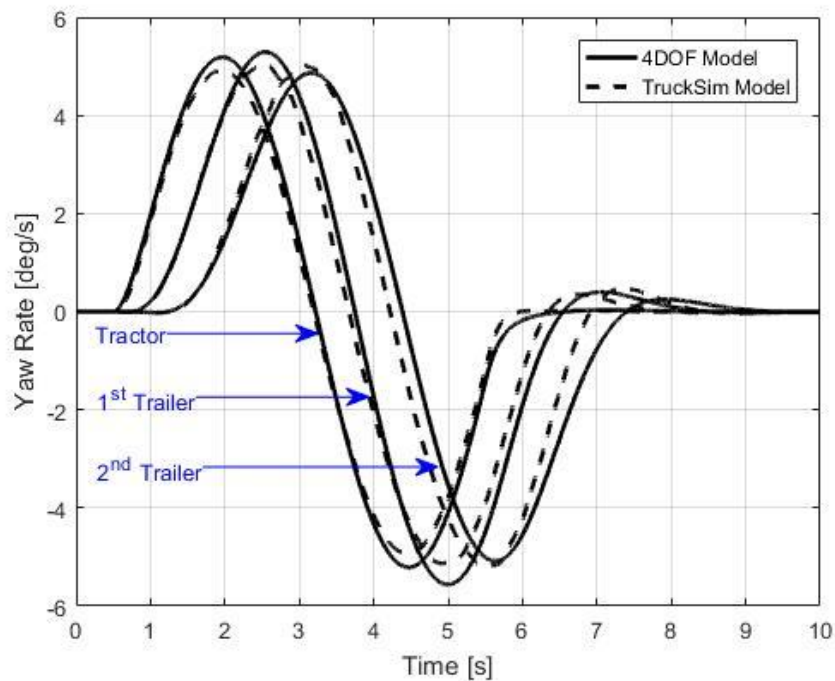


Figure 3.9 Time history of yaw rates of the 4DOF model and the TruckSim model under the 2<sup>nd</sup> SLC test maneuver.

### **3.4. ATS Hydraulic Actuation (AHA) System**

As previously mentioned, this research considers the effects of actuator dynamics on the ATS control system. Hence, an ATS hydraulic actuation (AHA) system model is developed. The AHA system is defined as a four-way valve controlled linear actuator configuration. The selected four-way valve is a two-stage solenoid actuated electrohydraulic valve, and the hydraulic configuration is extensively applied in the hydraulic control industry [85]. Valve controlled systems offer numerous benefits such as low complexity, high flexibility and accurate control. Such systems are widely employed for various applications such as industrial robots, mobile vehicle, agriculture equipment, and the aerospace industry [85].

In this section, the AHA system model is developed. The model includes a hydraulic actuator and an electrohydraulic valve. Thereafter, the governing equations of motion are determined and the system is linearized. Moreover, the system design parameters, such as the required piston diameter, nominal supply pressure, valve coefficients, and pump displacement, are determined based on the steady-state forms of the equations of motion. Finally, the linear model is validated using the non-linear Simscape hydraulic model.

#### **3.4.1. Hydraulic Actuator Modeling**

The AHA system configuration is illustrated in Fig. 3.10. The load to be moved by the hydraulic actuator is modelled as a single mass-spring-damper system [85]. Since the AHA system manipulates the steering angle of the trailer axles, the actuator position is the working objective. Thus, initially the actuator's load analysis is conducted.

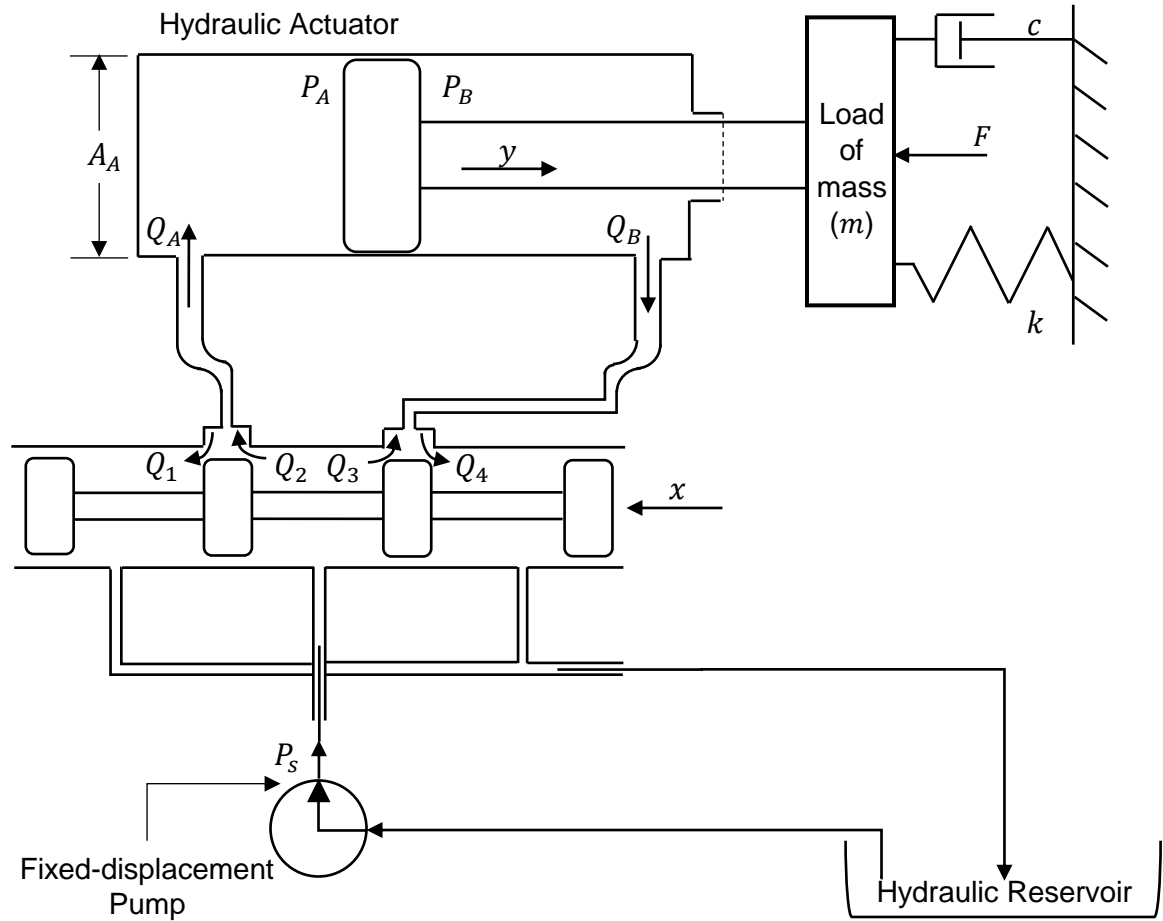


Figure 3.10 Schematic diagram for the AHA system [85].

The governing equation of motion for the load [85] is expressed as,

$$m\ddot{y} + c\dot{y} + ky = \eta_{af}(A_A P_A - A_B P_B) - F - F_o \quad (3.16)$$

where,  $m$  is the mass,  $k$  the spring stiffness,  $c$  the damping coefficient of the load,  $y$  the position of the load,  $A_A$  and  $A_B$  are the piston areas, and  $P_A$  and  $P_B$  the fluid pressures on the A and B sides of the actuator respectively.  $\eta_{af}$  is the force efficiency of the actuator,  $F$  is the disturbance force, and  $F_o$  is the nominal spring and bias load that is applied to actuator when  $y$  is zero.

$$y = 0; P_A = P_B = \frac{P_s}{2} \text{ and } F = 0 \quad (3.17)$$

where,  $P_s$  is the nominal supply pressure. Under steady-state nominal operating conditions, the conditions mentioned in Eq. (3.17) apply [85]. Moreover, from Eq. (3.17), the nominal force exerted on the actuator by the load can be defined as,

$$F_o = \eta_{af}(A_A - A_B) \frac{P_s}{2} \quad (3.18)$$

By substituting Eq. (3.18) in Eq. (3.16), the following equation is generated, which describes the output dynamics of the load.

$$m\ddot{y} + c\dot{y} + ky = \eta_{af} \left[ \left( A_A \left( P_A - \frac{P_s}{2} \right) - A_B \left( P_B - \frac{P_s}{2} \right) \right) \right] - F \quad (3.19)$$

It is evident from Eq. (3.19) that the actuator pressure  $P_A$  and  $P_B$  are required inputs to control the position of the load. These pressures are a result of changing flow and volume conditions within the actuator [85]. Thus, pressure analysis for the actuator is performed. To analyze the fluid pressures on sides A and B of the actuator, the pressure transient effects are neglected. The omission of pressure transient effect is valid for systems where the load dynamics are much slower than the pressure dynamics, and transmission distance between the valve and the actuator is small [85]. Using these assumptions, the volumetric flow rates in and out of the actuator for the system can be defined as,

$$\begin{cases} Q_A = \frac{A_A}{\eta_{av}} \dot{y} \\ Q_B = \frac{A_B}{\eta_{av}} \dot{y} \end{cases} \quad (3.20)$$

where,  $Q_A$  and  $Q_B$  are the volumetric flow rates in and out of the actuator respectively, and  $\eta_{av}$  is the volumetric efficiency of the actuator.

From Fig. (3.10), the flow rates in and out of the actuator can be defined (see Eq. (3.21)). The linearized flow equations for fluid passing across the metering lands of the four-way spool valve are defined in Eq. (3.22) [85].

$$\begin{cases} Q_A = Q_2 - Q_1 \\ Q_B = Q_4 - Q_3 \end{cases} \quad (3.21)$$

$$\begin{cases} Q_1 = K_c \frac{P_s}{2} - K_q x + K_c (P_A - P_r) \\ Q_2 = K_c \frac{P_s}{2} + K_q x + K_c (P_s - P_A) \\ Q_3 = K_c \frac{P_s}{2} - K_q x + K_c (P_s - P_B) \\ Q_4 = K_c \frac{P_s}{2} + K_q x + K_c (P_B - P_r) \end{cases} \quad (3.22)$$

where,  $x$  is the spool displacement, and  $K_q$  and  $K_c$  are the flow gain and the pressure flow coefficient for the valve respectively. The magnitude valve coefficients are the same for each metering land, as the pressure drop across each metering land is equal to half the supply pressure [85]. By substituting Eq. (3.22) into Eq. (3.21), the volumetric flow rates can be expressed as,

$$\begin{cases} Q_A = 2K_q x - 2K_c \left( P_A - \frac{P_s}{2} \right) \\ Q_B = 2K_q x + 2K_c \left( P_B - \frac{P_s}{2} \right) \end{cases} \quad (3.23)$$

Using Eq. (3.20) and (3.23), the operating pressures on both sides of the linear actuator can be written as,

$$\begin{cases} P_A - \frac{P_s}{2} = K_p x - \frac{A_A}{2K_c \eta_{av}} \dot{y} \\ P_B - \frac{P_s}{2} = -K_p x + \frac{A_B}{2K_c \eta_{av}} \dot{y} \end{cases} \quad (3.24)$$

where,  $K_p$  is valve pressure sensitivity given by the ratio of the flow gain to the pressure-flow coefficient ( $K_q/K_c$ ). Based on the above analysis and using Eq. (3.19) and (3.24), the linearized equation of motion for the AHA system is defined as,

$$m\ddot{y} + \left( c + \frac{A_A^2 + A_B^2}{2K_c} \right) \dot{y} + ky = \eta_{af}(A_A + A_B)K_p x - F \quad (3.25)$$

Eq. (3.25) suggests that the mechanical design parameters of the actuator and the control valve significantly affect the overall dynamics of the hydraulic control system [85]. Eq. (3.26) [85] defines the mechanical design parameters.

$$\begin{cases} A_A = A_B = \frac{2F_w}{\eta_{af}P_s} \\ K_q = \frac{2A_A v_o}{u \eta_{av}} \\ K_c = \frac{2A_A v_o}{P_s \eta_{av}} \\ K_p = \frac{K_q}{K_c} = \frac{P_s}{u} \end{cases} \quad (3.26)$$

where,  $F_w$  is the required working force to be produced by the hydraulic actuator, and  $v_o$  the desired no-load velocity. The values for these parameters are listed in Table 3.1.

### 3.4.2. Electrohydraulic Valve Modeling

The two-stage solenoid actuated electrohydraulic valve is modeled as a first-order transient system [85, 86]. Equation of motion for the valve is expressed as,

$$\tau \dot{x} + x = \varphi i \quad (3.27)$$

where,  $\tau$  represents the time constant for the transient response of the system,  $\varphi$  the steady-state gain, and  $i$  the input current. The time constant and the steady-state gain can be approximated by using Eq. (3.28) and (3.29) [85].

$$\begin{cases} \tau \approx \frac{A_s}{k_{qs}} \\ \varphi \approx \frac{\alpha}{k_s} \end{cases} \quad (3.28)$$

$$k_{qs} = 4u C_d \sqrt{\frac{P_p}{\rho}} \quad (3.29)$$

where,  $A_s$  is the cross-sectional area of the valve,  $\alpha$  the magnetic coupling coefficient,  $k_s$  the spring coefficient of the solenoid feedback spring,  $C_d$  the coefficient of discharge,  $\rho$  the fluid density, and  $P_p$  the pilot pressure of the electrohydraulic solenoid valve. Eq. (3.25) and (3.27) describe the AHA system model. The state-space form of the model is defined as,

$$\dot{x}_h(t) = A_h x_h(t) + B_h u_h(t) \quad (3.30)$$

$$x_h = [\dot{y} \ y \ x]^T \quad u_h = [i]^T \quad (3.31)$$

Matrices  $A_h$  and  $B_h$  are provided in Appendix B, and the operating range of input current  $i$  is  $\pm 20 \text{ mA}$ . Table 3.1 provides the values of design parameters.

Table 3.1 Design parameters for AHA system [85-89].

Symbol	Description	Nominal Value
$A_A = A_B$	Piston cross-sectional area	$3.521 \times 10^{-3} \text{ m}^2$
$K_q$	Valve flow gain coefficient	$0.6485 \frac{\text{m}^2}{\text{s}}$
$K_c$	Valve pressure flow coefficient	$5.245 \times 10^{-11} \frac{\text{m}^3}{\text{Pa s}}$
$K_p$	Valve pressure sensitivity	$1.2365 \times 10^{10} \frac{\text{Pa}}{\text{m}}$
$P_s$	Supply Pressure	$20 \times 10^6 \text{ Pa}$
$u$	Valve underlapped dimension	$1.6175 \times 10^{-3} \text{ m}$
$F_w$	Desired Working Force	32400 N
$v_o$	Desired no-load velocity	$0.2 \frac{\text{m}}{\text{s}}$
$\eta_{af}$	Actuator force efficiency	0.92
$\eta_{av}$	Actuator volumetric efficiency	0.96
$\tau$	Time constant for solenoid	0.01 s
$\varphi$	Valve steady-state gain	$0.025 \frac{\text{m}}{\text{A}}$

## 3.5. AHA System Model Validation

### 3.5.1. Non-linear Simscape Model

In the following chapter(s), the AHA system model discussed in Section 3.4 and the ATS controller are integrated. Therefore, it is imperative to examine the model's accuracy and fidelity. Hence, AHA system model is validated using the nonlinear Simscape software package.

Simscape supports the modeling of physical systems using Simulink [90]. Moreover, it allows direct integration of physical component models using block diagrams. Simscape library consists of physical component models, such as electric motors, rectifiers, hydraulic actuators, etc. [90]. The design parameters of these components are adjustable. Additionally, Simscape supports hardware-in-the-loop (HIL) testing, and C-code generation [90]. A system model can be created by assembling these components into a schematic. Fig. 3.11 illustrates the non-linear hydraulic system model.

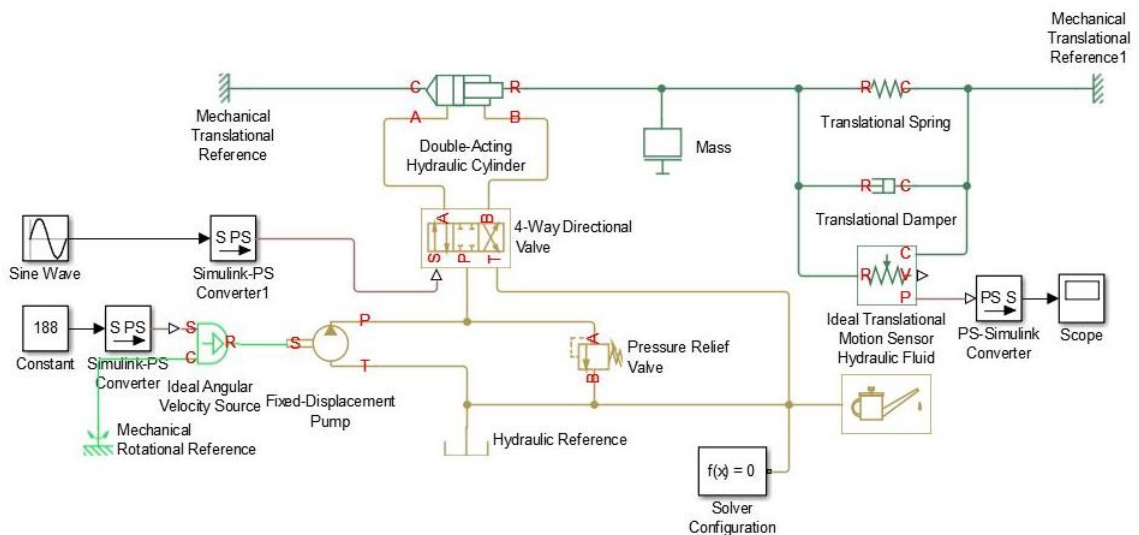


Figure 3.11 Block diagram of the Simscape hydraulic model.

### 3.5.2. AHA System Validation

To validate the linear AHA model, the actuator's position response is evaluated, and the results are compared with the Simscape model. The model is validated using two different inputs. The system is first analyzed using a step input to evaluate the system's rise time, followed by a sinewave input to ensure that the AHA model can track the Simscape model. The magnitude of input current in both cases is 20 mA.

Fig. 3.12 and 3.13 show the time history of actuator position for the step input and sinewave input respectively. Fig. 3.12 shows that both models have similar rise times. Moreover, the AHA model can accurately track the Simscape model during the sinewave input (see Fig. 3.13). The results help establish the validity of the linear AHA model.

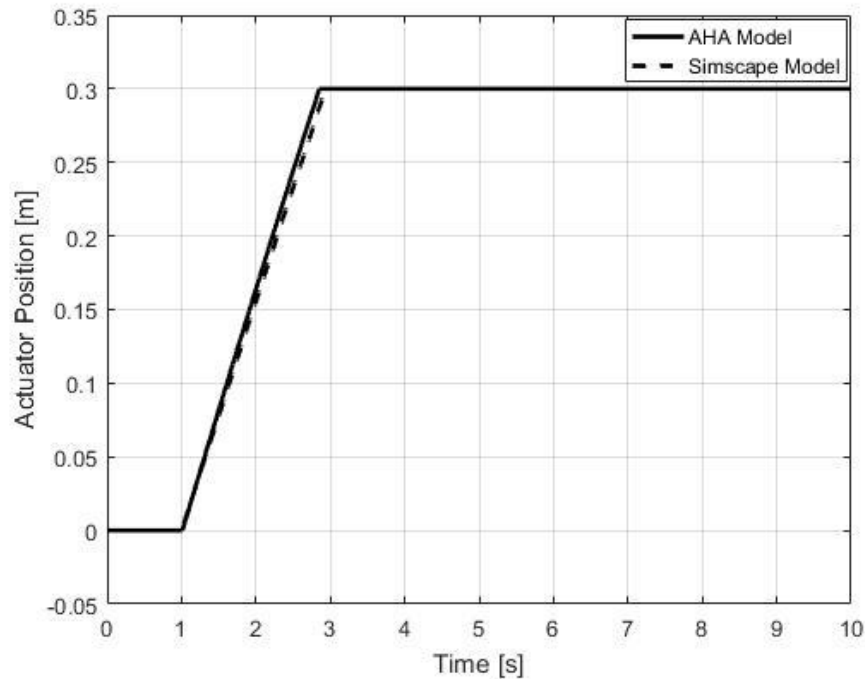


Figure 3.12 Time history of actuator position response for the AHA model and the Simscape model to the step input.

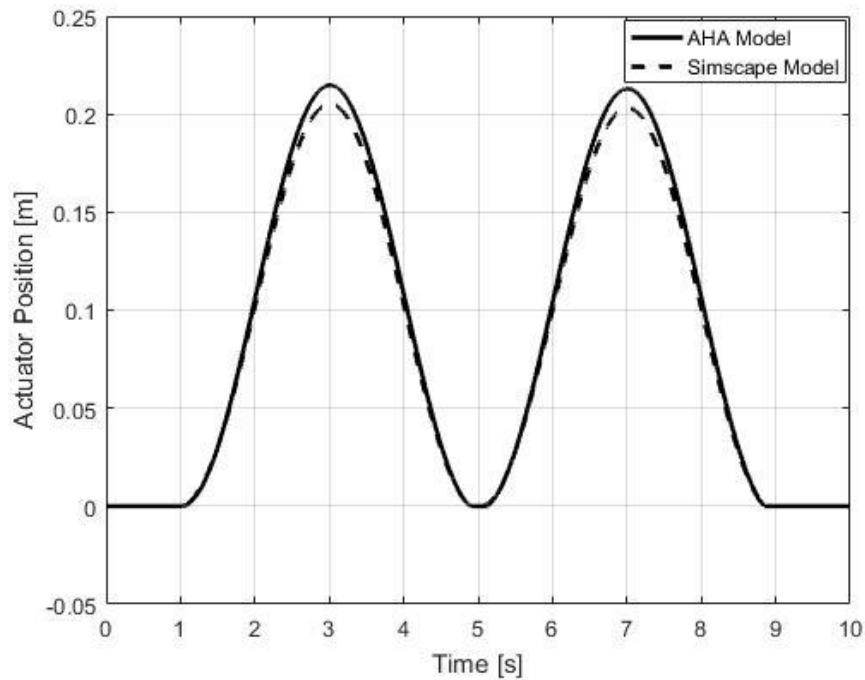


Figure 3.13 Time history of actuator position response for the AHA model and the Simscape model to the sinewave input.

### 3.6. Summary

This chapter described the vehicle systems modeling and validation. First, a linear 4DOF model for a B-Train double was derived. The 4DOF model was validated using the TruckSim software, under two recommended SLC maneuvers. Both the 4DOF and the TruckSim models demonstrated reasonable agreement under the SLC maneuvers. The 4DOF model has been further utilized in Chapter 4 for controller synthesis. Thereafter, the AHA system model was derived, and validated using the Simscape software. The AHA system model has been developed to analyze the effects of actuator dynamics on the controller's performance (see Section 4.3), and to develop fault diagnosis strategies (see Section 4.5.3). The design parameters for the AHA system have been adopted from literature [85-89].

# CHAPTER 4

## FAULT TOLERANT CONTROL OF ACTIVE TRAILER STEERING SYSTEMS

### 4.1. Introduction

This chapter discusses the fundamental elements of the FTC framework necessary for the ATS system. It primarily focuses on selecting the most appropriate controller and observer designs for the model-based FTC-ATS scheme. First, the effectiveness of LQR and  $H^\infty$  control techniques is compared and their suitability for the FTC-ATS scheme is discussed. Thereafter, the ATS Hydraulic Actuation (AHA) system model (see Section 3.4) is integrated with the controllers and the effects of actuator dynamics on the closed-loop system are analyzed. Moreover, the limitations of the AHA system are examined.

Considering the widespread acceptance and effectiveness of observer-based FTC systems (see Section 2.5), this research evaluates the Luenberger Observer and Kalman Filter observer designs, for the FTC-ATS scheme. Both observer designs are analyzed for their effectiveness in predicting true outputs and estimating states using noisy and/or incomplete measurement data. Subsequently, the most suitable controller and observer design(s) are selected for designing the FTC-ATS scheme. The observers are designed by utilizing the generalized observer scheme (see Section 2.5.1), where each observer monitors a specific sub-system. Finally, the FTC-ATS scheme is evaluated under simulated failures, such as actuator and sensor malfunctions, using the TruckSim vehicle model.

Although ATS systems can significantly improve both high-speed and low-speed performance of MTAHVs, this research exclusively focuses on the high-speed performance. Since the primary concern of this research is fault tolerance, it is logical to assume that faults and failures that may occur at high-speeds require greater surveillance than those at low-speeds. Therefore, in this chapter the performance of the various elements of the FTC-ATS scheme is evaluated using the high-speed Single Lane Change (SLC) and Double Lane Change (DLC) maneuvers. The SLC and DLC maneuvers are selected with the intention to analyze the ATS performance under low and high actuator demands respectively. Fig. 4.1 illustrates the steering wheel angle (see Section 3.3.2 for angular ratio of the steering system) for the two maneuvers, where the SLC maneuver is adopted from [83], and the DLC maneuver from TruckSim. The vehicle forward speed for both the maneuvers is a constant 88 km/h.

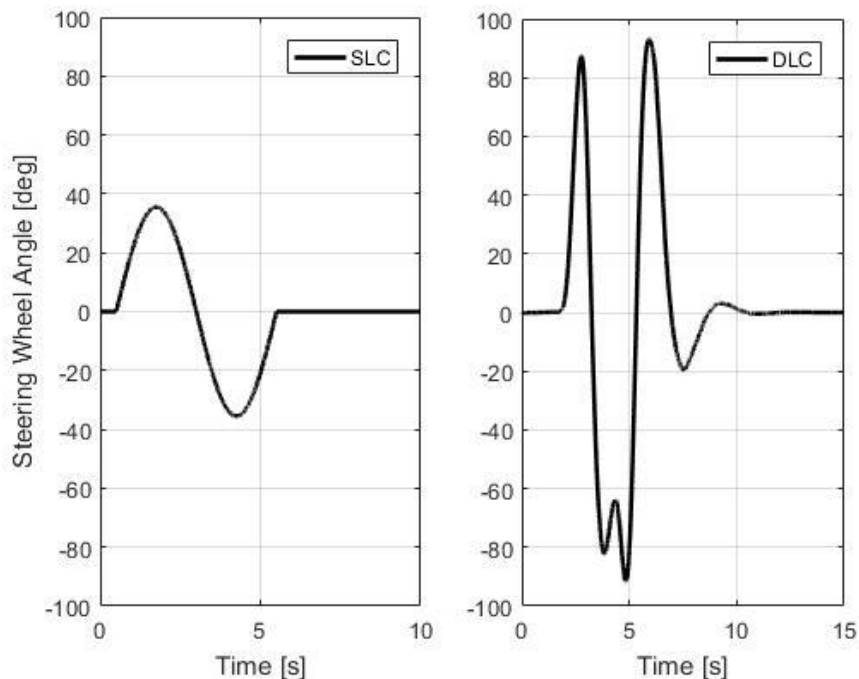


Figure 4.1 Time history of Steering Wheel Angles for SLC and DLC maneuvers.

## 4.2. Controller Synthesis

### 4.2.1. Introduction

LQR based controllers are widely employed for ATS systems primarily due to their simplicity and reasonable performance. However, in the presence of uncertainties such as noise, variation in system parameters etc., the LQR controller is unable to achieve the desired performance. As mentioned in Section 2.3.2, the  $H^\infty$  technique is a widely accepted control strategy for achieving robust stability and performance in presence for uncertainties. Therefore, to select the most effective controller for the FTC-ATS scheme, this section compares the performance of the LQR and  $H^\infty$  based ATS controllers.

Before designing the controller for the ATS system, the location of the ATS axle(s) must be finalized. Most studies [6-8, 13, 28-36] assume that in an ATS-controlled vehicle all trailer axles are assisted with an individual ATS system. However, in the real world such an assumption is unreasonable. For example, the B-Train double (see Fig. 3.2) consists of six trailer axles, which means that conceptually the vehicle consists of six independently controlled hydraulic actuation systems. Such an integrated system will lead to very high complexity and unreasonable costs. Although an all-axle ATS system is superior, to address the aforementioned economic concerns this study assumes only three axles are ATS axles. The first and third axles of the first trailer and the first axle of the second trailer are considered as ATS axles. Hereafter, these axles will be referred as Axle 4, Axle 6 and Axle 7 respectively. Axles 4, 6 and 7 were selected, since they illustrated the highest influence on the dynamic behavior of the B-Train double.

## 4.2.2. LQR Control

### 4.2.2.1. LQR Control Theory

A continuous-time system can be described as,

$$\dot{x}(t) = Ax(t) + Bu(t) \quad (4.1)$$

The infinite horizon LQR problem considers the following state-feedback law,

$$u(t) = -Kx(t) \quad (4.2)$$

Which is the result of minimizing the quadratic cost function,

$$J = \int_0^{\infty} (x^T Q x + u^T R u) dt \quad (4.3)$$

The LQR problem mandates that the pair of system matrices ( $A, B$ ) is stabilizable.

The feedback gain  $K$  is computed by solving the Algebraic-Riccati Equations (ARE) [3, 8, 13]. Where,  $Q$  and  $R$  represent the weighting matrices that penalize the magnitude and duration of the states and control inputs respectively. The selection of  $Q$  and  $R$  matrices is discussed in the next sub-section.

### 4.2.2.2. Selection of Q and R Matrices

$Q$  and  $R$  matrices define the desired performance of a LQR control system.  $R$  is the input-weighting matrix that penalizes the control input, whereas  $Q$  is the state-weighting matrix that penalizes the states. In this study, the commonly used trial and error method is employed for selecting both matrices; where the values of both matrices are fine-tuned to obtain the desired performance while minimizing control input based on hardware limitations.

#### 4.2.2.3. Simulation Results

This sub-section presents the comparative results of the baseline vehicle and LQR controlled vehicle under the aforementioned high-speed SLC and DLC maneuvers. Fig. 4.2 and 4.3 illustrate the time history of lateral accelerations of the baseline vehicle and the LQR controlled vehicle under both maneuvers. Fig. 4.2 suggests that the LQR controller can successfully enhance the vehicle's stability by reducing the peak lateral acceleration of all vehicle units. Moreover, the controller significantly reduces the peak lateral acceleration of the rearmost trailer, thereby reducing its rollover tendency. Fig. 4.3 shows the LQR controller's inability to enhance the vehicle's stability during the complex DLC maneuver. As shown in the figure, throughout the maneuver, both the baseline and the controlled vehicle exhibit approximately the same lateral acceleration responses.

Fig. 4.4 and 4.5 illustrate the yaw rate responses of the two vehicles under SLC and DLC maneuvers respectively. Similar to the lateral acceleration response it is evident that the LQR controller exhibits superior performance under the SLC maneuver. It is worthy mentioning that the LQR controlled vehicle has lower peak values of yaw rate for all vehicle units under both maneuvers. Moreover, the controlled vehicle exhibits reduced settling times. Although the reduction of peak lateral acceleration and yaw rate is desired, these performance measures cannot sufficiently explain the true behavior of the vehicle. Both lateral acceleration and yaw rate affect the vehicle's desired trajectory. Ideally, the controller should optimize these performance measures while maintaining the desired trajectory.

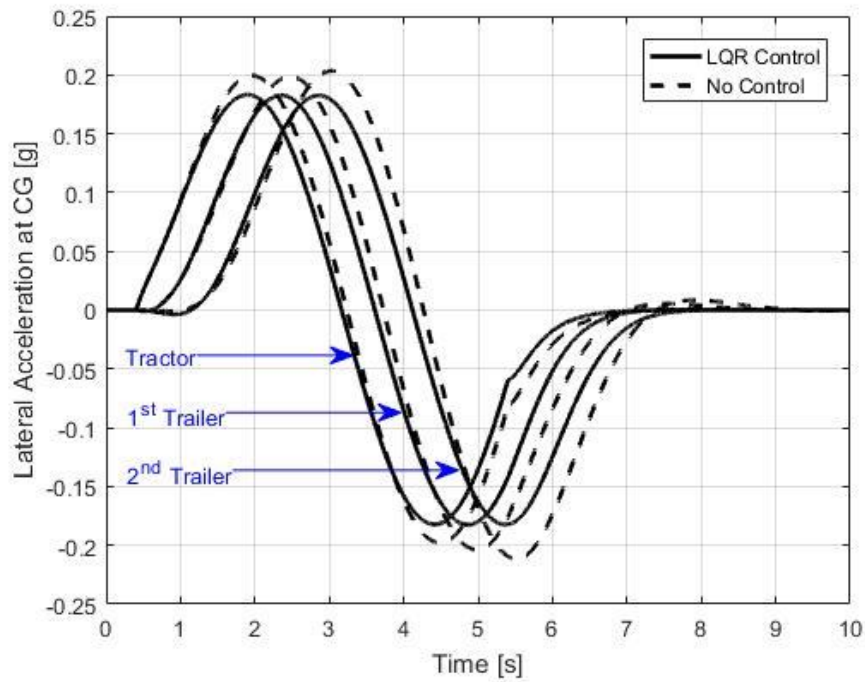


Figure 4.2 Time history of lateral accelerations for the LQR controlled vehicle and the baseline vehicle under the SLC maneuver.

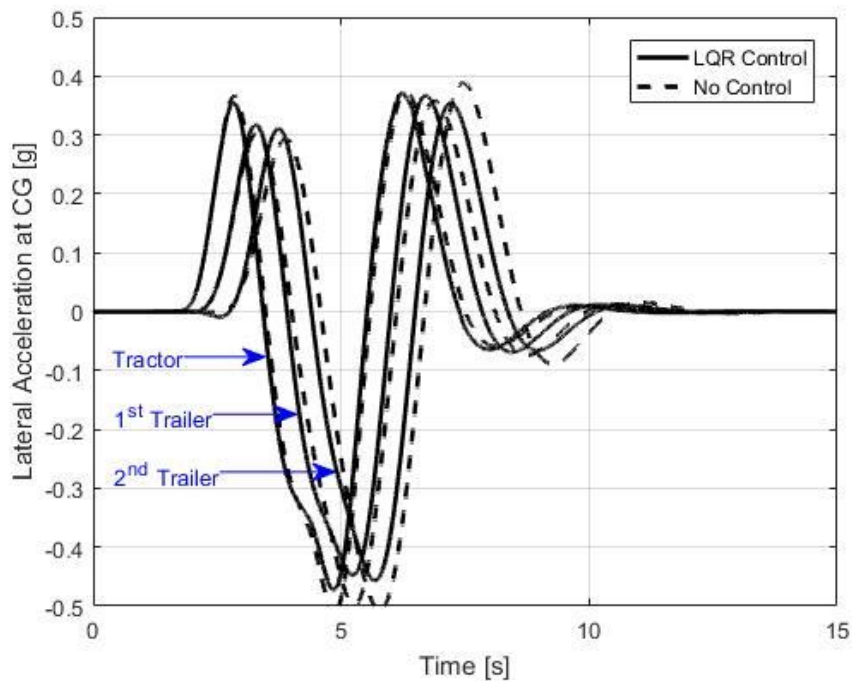


Figure 4.3 Time history of lateral accelerations for the LQR controlled vehicle and the baseline vehicle under the DLC maneuver.

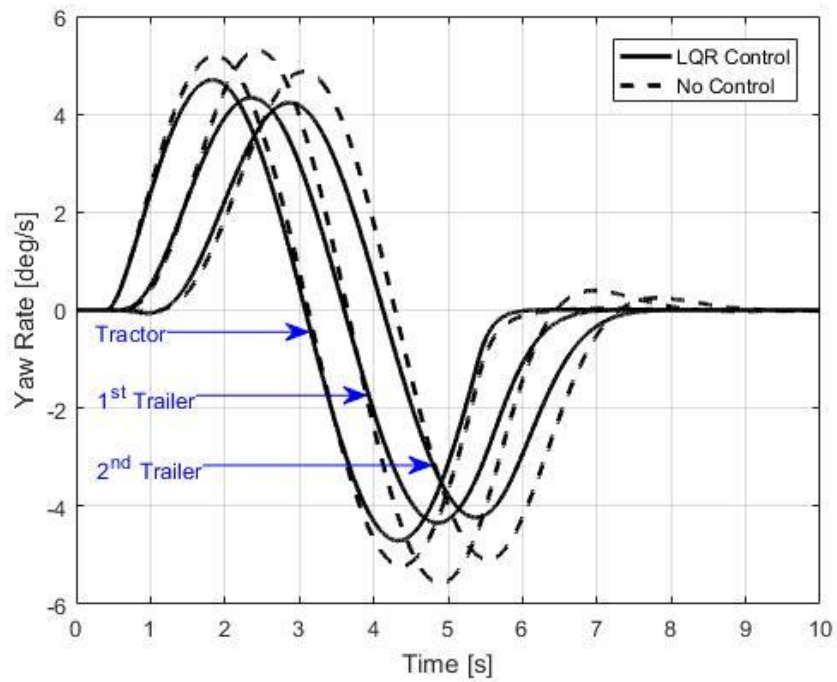


Figure 4.4 Time history of yaw rates for the LQR controlled vehicle and the baseline vehicle under the SLC maneuver.

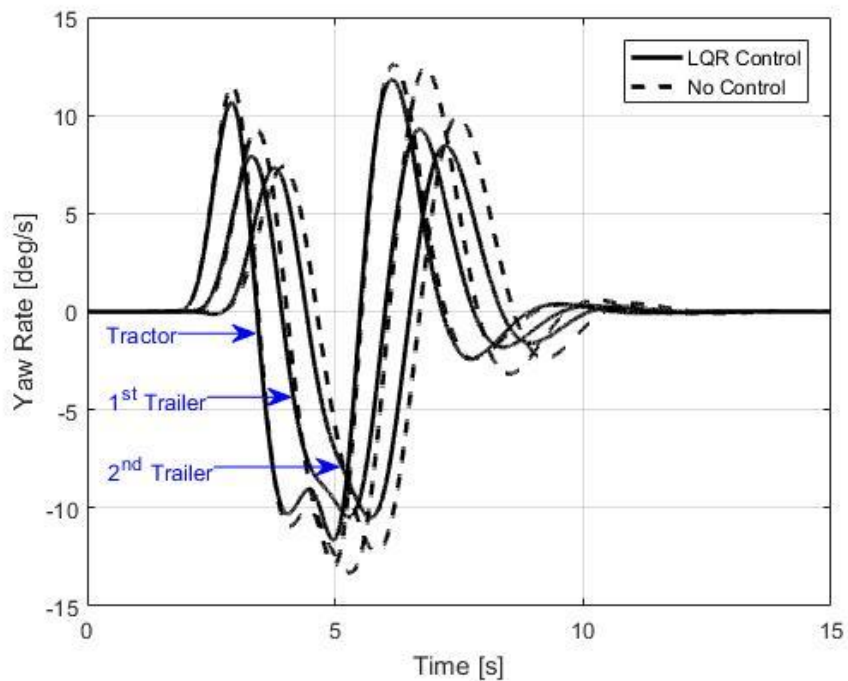


Figure 4.5 Time history of yaw rates for the LQR controlled vehicle and the baseline vehicle under the DLC maneuver.

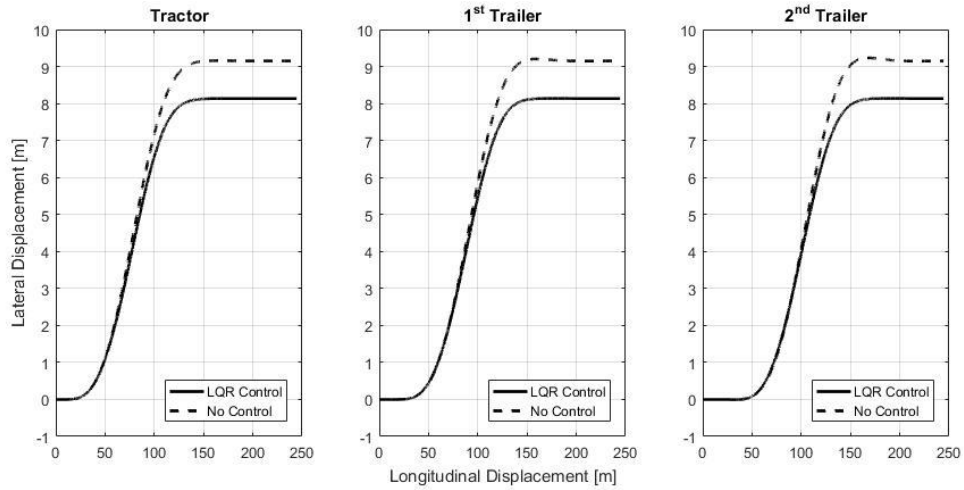


Figure 4.6 Trajectories of the LQR controlled vehicle and the baseline vehicle under the SLC maneuver.

Fig. 4.6 and 4.7 illustrate the trajectories of the three vehicle units under the SLC and DLC maneuvers respectively. The lateral displacement achieved under the SLC maneuver is 9m. Although in reality, such a high value is not feasible, the aim here is to analyze the influence of the control system on the vehicle’s path following. Both figures suggest that the LQR controlled vehicle is unable to follow the intended path. The intended path following can be improved by employing a closed-loop driver model or by adding a reference yaw rate model.

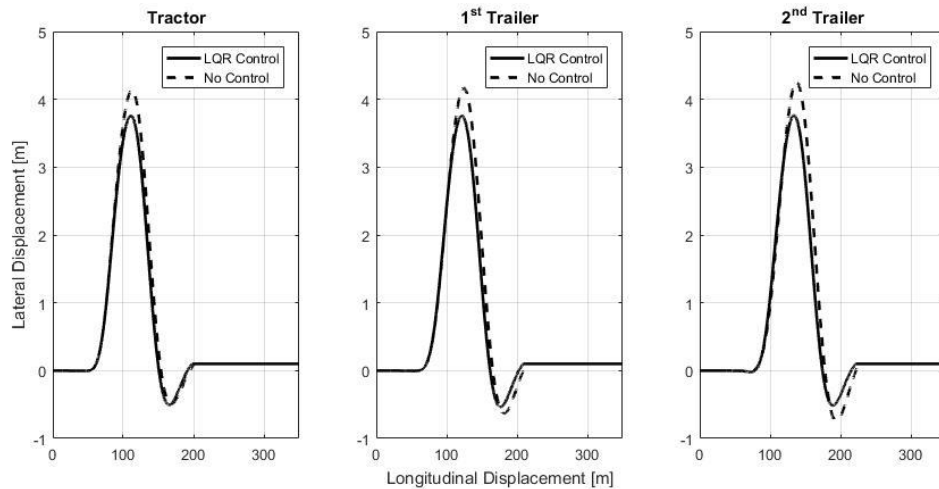


Figure 4.7 Trajectories of the LQR controlled vehicle and the baseline vehicle under the DLC maneuver.

### 4.2.3. $H^\infty$ Control

Considering the drawbacks of LQR control, a robust control strategy is required, which is capable of regulating the vehicle's dynamic behavior during complex maneuvers without hampering its intended path. The following sub-sections discuss the synthesis of an  $H^\infty$  based controller for the ATS system.

#### 4.2.3.1. $H^\infty$ Control Theory

Cost functions represent the design objectives of the closed-loop system, such as accurate reference tracking, disturbance rejection and robust stabilization and so on [50, 51]. Contrary to the LQR control methodology, a robust control design requires multiple cost functions. A suitable design consists of a combination of such cost functions. The  $H^\infty$  control technique deals with the optimization problem presented in the frequency domain [50]. Frequency dependent weighting functions are employed to minimize the cost functions and achieve the desired closed-loop system performance [51].

In this research, the mixed-sensitivity  $H^\infty$  synthesis is employed, where the objective is to formulate a stabilizing controller  $K$  to minimize the output  $z$  over all external inputs  $w$  [50]. Moreover, this technique permits accurate reference tracking while minimizing the required control input [50, 51]. Eq. (4.4) depicts the nominal performance criteria that must be satisfied by the control system [50].

$$\min_{K \text{ stabilizing}} \left\| \frac{(I + GK)^{-1}}{K(I + GK)^{-1}} \right\|_\infty \quad (4.4)$$

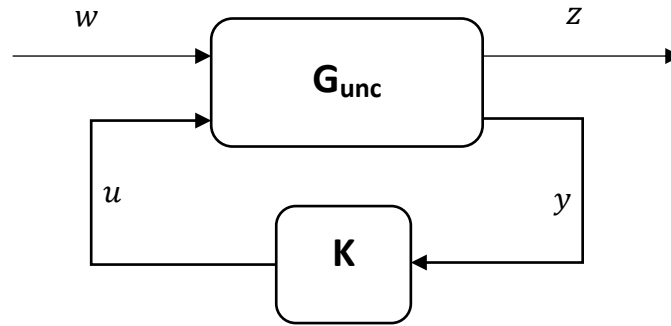


Figure 4.8 Configuration of a generalized  $H^\infty$  closed-loop system

Fig. 4.8 depicts a generalized  $H^\infty$  closed-loop system with system uncertainties and disturbances [50].  $G_{unc}$  is the uncertain system,  $K$  represents the stabilizing controller,  $z$  denotes the measured output signals to be controlled,  $w$  depicts all the external inputs,  $y$  is the measurements available to the controller  $K$ , and  $u$  represents control signal. System uncertainties represent any external disturbances, or un-modeled dynamics. External disturbances may arise as unknown inputs, for example, heavy crosswinds that deviate the vehicle from its desired path. Whereas, un-modeled dynamics include the variation between the physical system and its mathematical representation.

#### 4.2.3.2. Selection of Weighting Functions

As mentioned in Section 4.2.3.1, the desired closed-loop performance in a  $H^\infty$  control system is regulated by selecting appropriate weighting functions. The control system comprises of performance weighting functions ( $W_p$ ), disturbance rejection functions ( $W_d$ ) and control-signal weighting functions ( $W_u$ ). The performance weighting functions regulate the system outputs, disturbance rejection functions ensure noise rejection, whereas the control-signal weighting functions minimize the control signal requirements.

In this study, the  $H^\infty$  controller is designed to ensure that the vehicle units follow their respective desired yaw rates. Section 4.2.3.4 describes the desired yaw rate reference model. This strategy simultaneously enhances the vehicle stability and ensures minimal deviation of the vehicle from its intended path. Thus, the control system comprises of three performance weighting functions depicting the respective yaw rates of the vehicle units, three disturbance rejection functions related to the three yaw rate outputs, and three control-signal weighting functions responsible for the three ATS axes. The inputs to the controller are the errors between the desired and actual yaw rates of the vehicle units, whereas the controller's outputs are the ATS angles. Fig. 4.9 depicts the closed-loop system diagram of the B-Train double with the  $H^\infty$  controller and the various weighting functions.

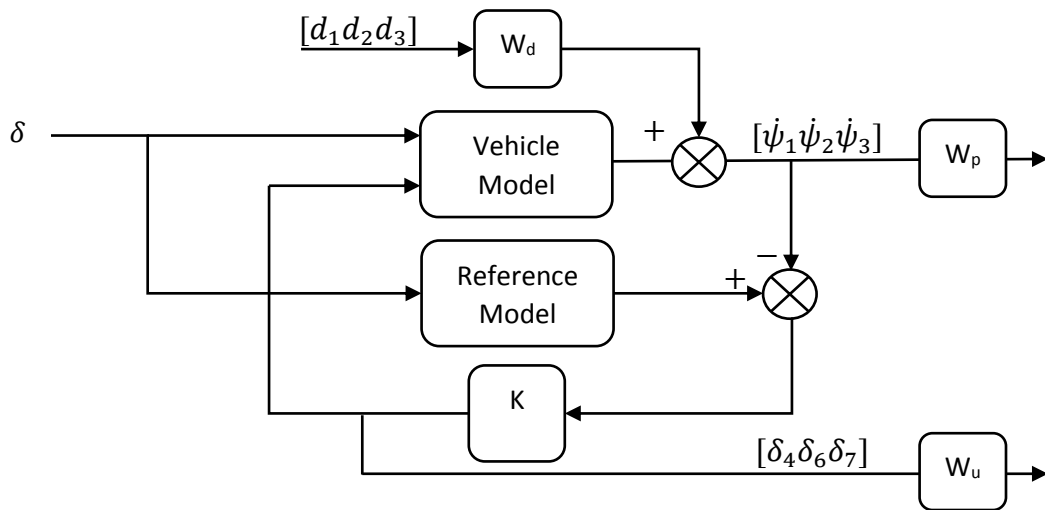


Figure 4.9 Configuration of the  $H^\infty$  controller for ATS system.

Generally, the weighting functions are modeled as band-pass filters [48, 51], and they are fine-tuned using the trial and error method. However, designing a robust controller by using the trial and error method can be challenging. Nevertheless, certain weighting functions such as the control-signal weighting function, cannot be arbitrarily chosen. These functions must consider the actuator limitations. Hence, in this study, suitable control-signal weighting functions are chosen based on the hydraulic actuators' frequency bandwidths. Conversely, considering the challenging nature of the trial and error method, a Genetic algorithm (GA) optimization method is employed to optimize the performance weighting and disturbance rejection functions.

A Genetic Algorithm (GA) is a preferred optimization method for solving complex optimization problems. It is a stochastic evolutionary algorithm inspired by the principles of natural evolution [48, 92]. The fundamental steps of a GA include coding, selection, crossover and mutation. In the beginning, GA selects an initial set of random values by employing uniform probability distribution [48, 92]. Further, the most suitable values are chosen for crossover and mutation, where another set of suitable values are produced from the previous iteration. The process continues until the optimal values are achieved.

The random selection processes of GA provides it with the capabilities of escaping the local domain, and enables it to find the global optima for the problem [92]. Table 4.1 displays the final values of the optimized performance weighting functions ( $W_p$ ), disturbance rejection functions ( $W_d$ ) and control-signal weighting functions ( $W_u$ ).

The control-signal weighting functions are adopted from [51] and [93]. Eq. (4.5) defines the second-order control-signal weighting functions.

$$\left\{ \begin{array}{l} W_u = G^o \frac{\left(\frac{1}{2\pi f_l} s + 1\right) \left(\frac{1}{2\pi f_u} s + 1\right)}{\left(\frac{1}{40\pi f_u} s + 1\right)^2} \\ G^o = G \frac{\left(\frac{\Delta f}{40\pi f_u} + 1\right)^2}{\left(\frac{\Delta f}{2\pi f_l} s + 1\right) \left(\frac{\Delta f}{2\pi f_u} + 1\right)} \\ \Delta f = \frac{2\pi(f_u + f_l)}{2} \end{array} \right. \quad (4.5)$$

where,  $f_l$  and  $f_u$  represent the lower and upper limit frequencies of actuator bandwidth, and  $G$  represents a band pass filter that limits the use of the actuator frequencies between  $f_l$  and  $f_u$ .

Table 4.1 Optimal Weighting Functions for the  $H^\infty$  Controller.

Performance Weighting Functions	Disturbance Rejection Functions	Control-signal Weighting Functions
$\left[ \frac{0.05151s + 0.002813}{s + 0.05151} \right]$	$\left[ \frac{0.03782s + 0.001}{0.1827s + 1} \right]$	$\left[ \frac{10^{-5}s^2 + 0.0168s + 0.09894}{10^{-8}s^2 + 0.0006s + 1} \right]$
$\left[ \frac{0.1848s + 0.02577}{s + 0.1662} \right]$	$\left[ \frac{0.01799s + 0.001}{0.3078s + 1} \right]$	$\left[ \frac{10^{-5}s^2 + 0.0168s + 0.09894}{10^{-8}s^2 + 0.0006s + 1} \right]$
$\left[ \frac{0.2257s + 0.03731}{s + 0.1667} \right]$	$\left[ \frac{0.04032s + 0.001}{0.2552s + 1} \right]$	$\left[ \frac{10^{-5}s^2 + 0.0168s + 0.09894}{10^{-8}s^2 + 0.0006s + 1} \right]$

#### 4.2.3.3. Controller Optimization for Variation in Forward Speed

A robust controller must account for variation in vehicle's forward speed. As this study only considers the high-speed operation, the  $H^\infty$  controller is optimized for a speed range of 40 to 120 km/h. To optimize the controller, the forward speed is considered as an uncertain variable and the GA is employed for providing optimal results such that the controller achieves robust performance under the entire range. The proof of the system robustness is displayed in Fig. 4.10, which shows the  $H^\infty$  norm over a wide frequency range. The desired values of the  $H^\infty$  norm should be less than one for the system to be robust [50] (see Eq. (4.6)).

$$\|T_{zw}\|_\infty < 1 \quad (4.6)$$

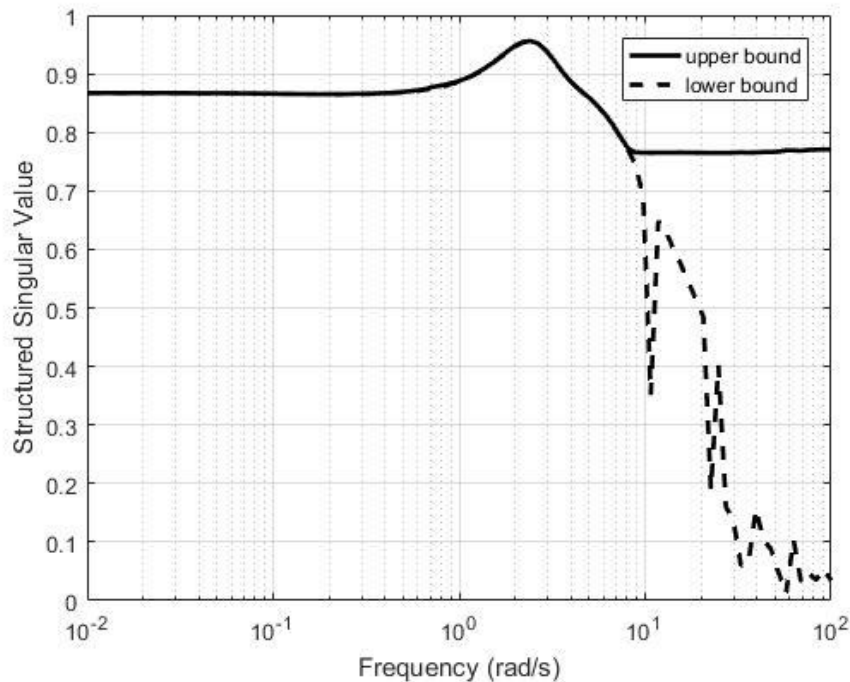


Figure 4.10 Frequency response of the  $H^\infty$  closed-loop system in the entire range vehicle forward speeds.

#### 4.2.3.4. Yaw Rate Reference Model

In many studies [36, 48, 51, 94-96], the desired yaw rate is calculated by using the steady-state yaw rate of a linear bicycle model. The linear bicycle model reflects the desired relationship between the steering input and the vehicle yaw rate [95]. The steady-state yaw rate is a function of the vehicle forward speed and the steering input [94, 95], and effectively defines the vehicle's desired yaw dynamics. However, a vehicle's yaw rate is limited by the road adhesion coefficient [51, 94-95]. Thus, the desired yaw rate should include the road adhesion coefficient to define the limits of available yaw rate [51, 94]. This ensures that the available grip is considered while generating the desired yaw rate signal.

In this research, the desired yaw rate is generated by employing the linear vehicle model presented in Section 3.2. First, the steady-state yaw-rate gain with respect to the steering input is computed by disregarding the dynamic elements in the bicycle model, and employing Cramer's rule. Thereafter, the yaw-rate gain and steering input are multiplied to generate the steady-state yaw rate signal. Suitable time delays [51] and transport delays are added to generate the desired yaw rate signals for the vehicle units. Finally, the desired yaw rates are bounded by the road adhesion coefficient. Eq. (4.7) depicts the desired and bounded yaw rate signals. Application of Cramer's rule to calculate steady-state yaw rate is provided in [96].

$$\left\{ \begin{array}{l} \dot{\psi}_{des} = \left[ \frac{1}{T_{delay}S + 1} \right] \dot{\psi}_{ssgain} \delta \\ \dot{\psi}_{lim} = \begin{cases} \dot{\psi}_{des} & \text{if } \dot{\psi}_{des} \leq 0.85 \frac{\mu g}{V_x} \\ 0.85 \frac{\mu g}{V_x} & \text{if } \dot{\psi}_{des} > 0.85 \frac{\mu g}{V_x} \end{cases} \end{array} \right. \quad (4.7)$$

where,  $\dot{\psi}_{des}$  depicts the desire yaw rate,  $T_{delay}$  the induced time-delay,  $\dot{\psi}_{ssgain}$  the steady-state yaw rate gain computed by Cramer's rule,  $\delta$  the steering angle,  $\dot{\psi}_{lim}$  the bounded yaw rate signal,  $\mu$  the road-adhesion coefficient,  $g$  the gravitational constant, and  $V_x$  the vehicle forward speed.

#### 4.2.3.5. Simulation Results

This sub-section compares the dynamic performance of the baseline vehicle and the  $H^\infty$  controlled ATS vehicle. Similar to Section 4.2.1., the SLC and DLC maneuvers are simulated to establish the efficacy of the  $H^\infty$  controller. Fig. 4.11 and 4.12 show the lateral acceleration response of the baseline vehicle and the  $H^\infty$  controlled vehicle under the SLC and DLC maneuvers respectively. Results suggest that the  $H^\infty$  controller successfully augments the dynamic performance of the vehicle under both maneuvers. Compared to the LQR controller,  $H^\infty$  successfully reduces the peak lateral acceleration for all vehicle units under the DLC maneuver. Fig. 4.13 and 4.14 illustrate the time history of yaw rates for the baseline and the controlled vehicles under the SLC and DLC maneuvers. Both figures show reduced peak yaw rates. Although, in comparison to the LQR controller, similar settling times are observed for both maneuvers.

Since the  $H^\infty$  controller tracks a reference yaw rate, the controller's tracking performance of is evaluated. Fig. 4.15 and 4.16 present the reference tracking performance of the controller under both the maneuvers. Both figures illustrate accurate reference tracking ability of the  $H^\infty$  controller. Fig. 4.11 to 4.16 aid to establish the robustness of  $H^\infty$  controller under both simple and complex maneuvers.

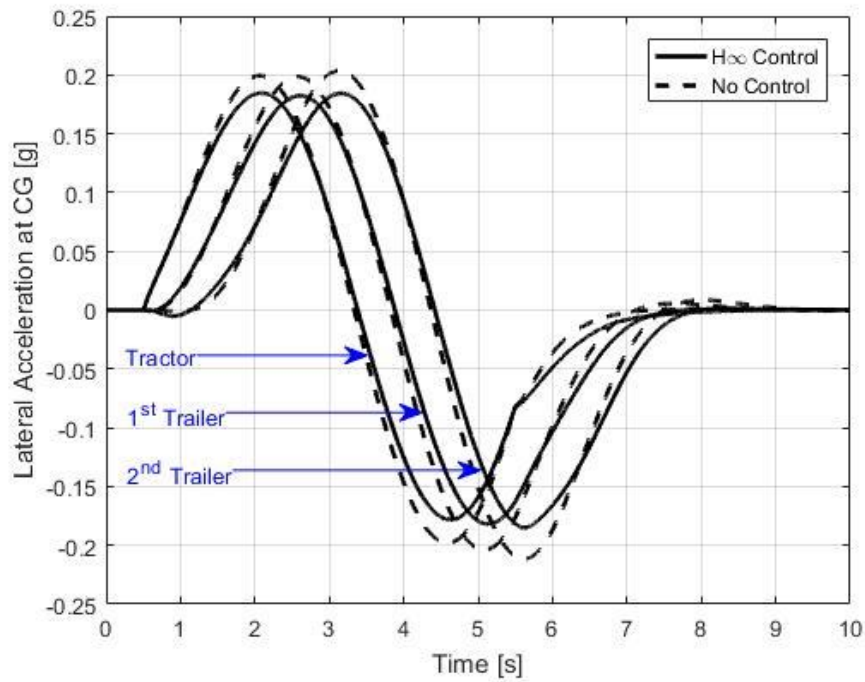


Figure 4.11 Time history of lateral accelerations for the  $H^\infty$  controlled vehicle and the baseline vehicle under the SLC maneuver.

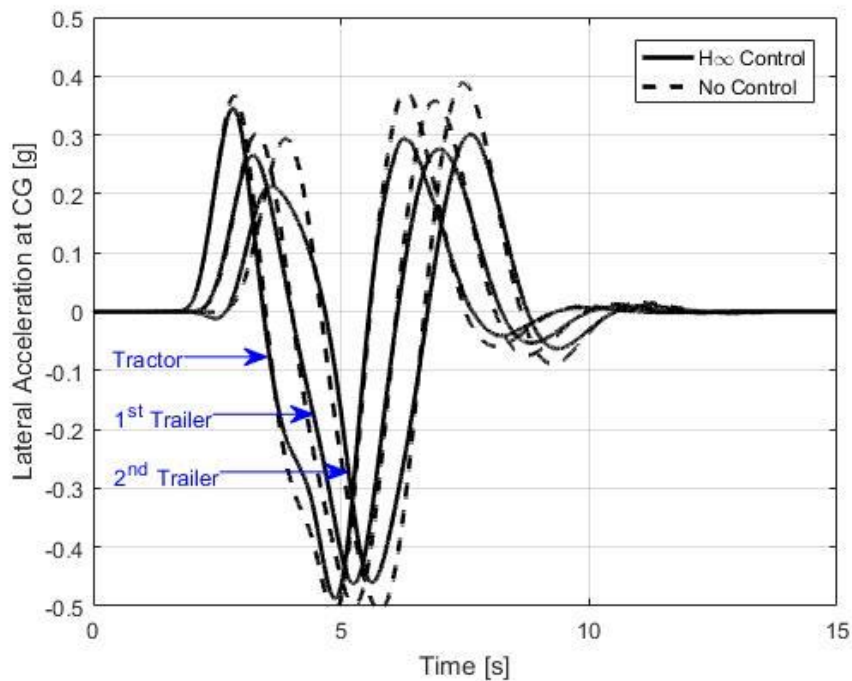


Figure 4.12 Time history of lateral accelerations for the  $H^\infty$  controlled vehicle and the baseline vehicle under the DLC maneuver.

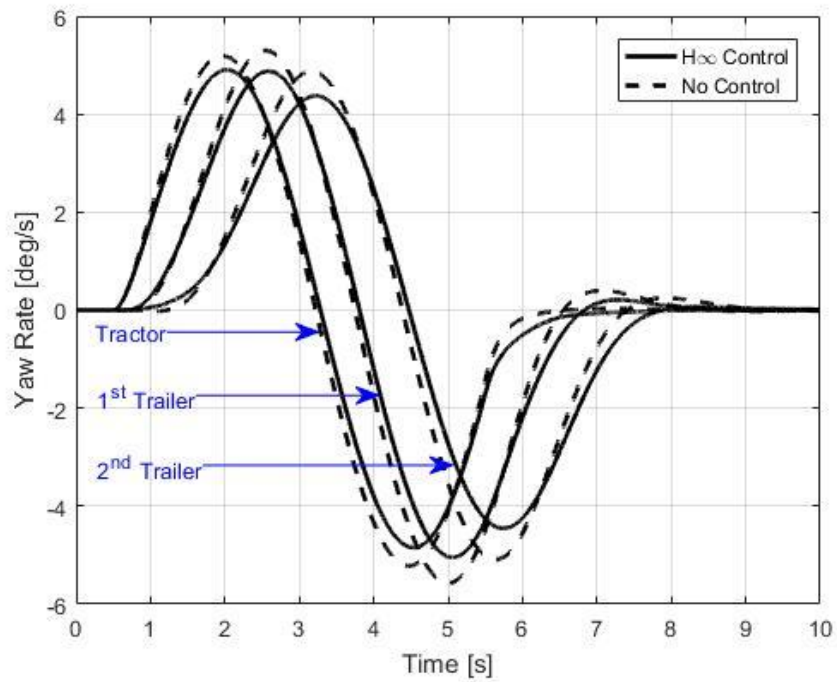


Figure 4.13 Time history of yaw rates for the  $H^\infty$  controlled vehicle and the baseline vehicle under the SLC maneuver.

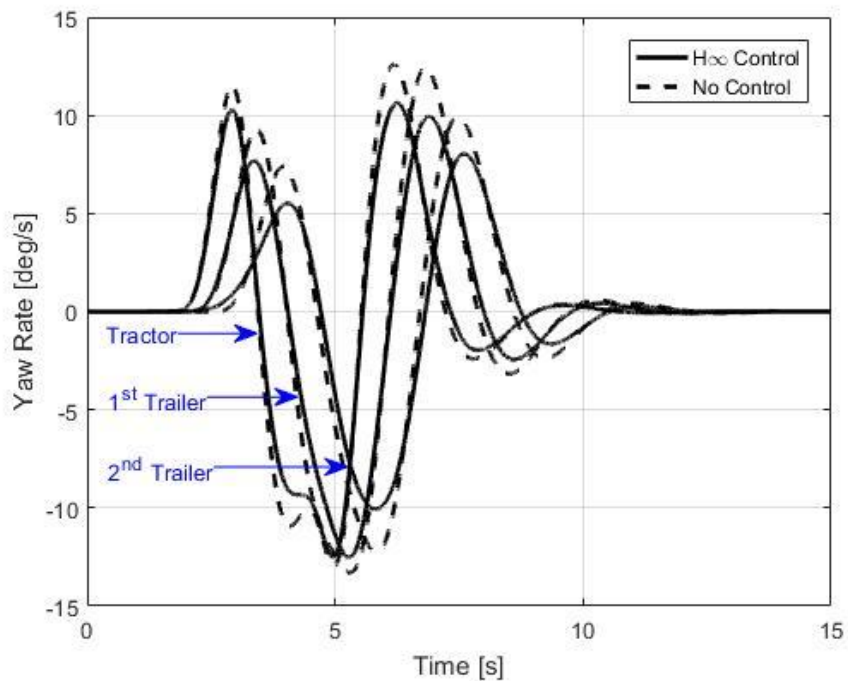


Figure 4.14 Time history of yaw rates for the  $H^\infty$  controlled vehicle and the baseline vehicle under the DLC maneuver.

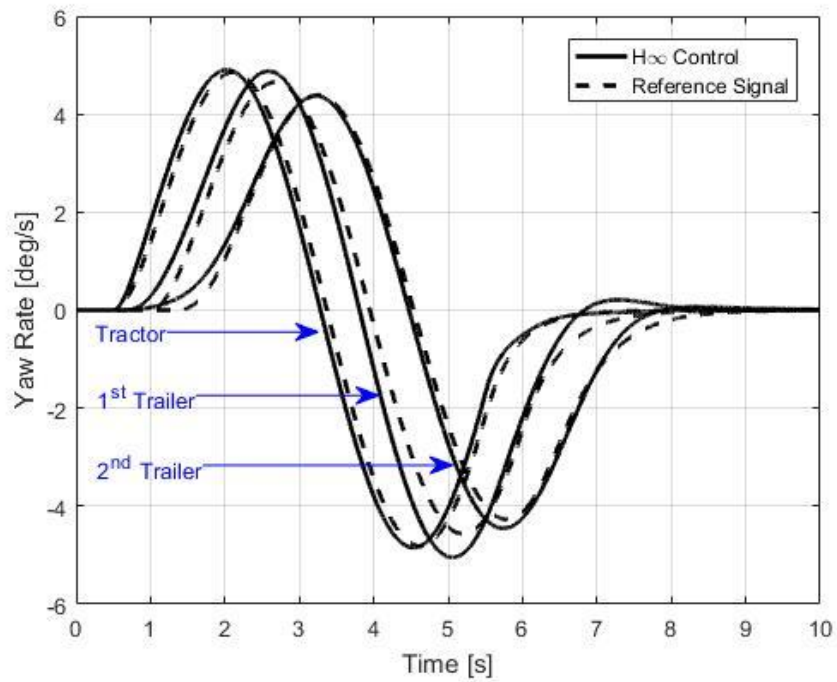


Figure 4.15 Time history of yaw rates for the  $H^\infty$  controlled vehicle, and the reference signals under the SLC maneuver.

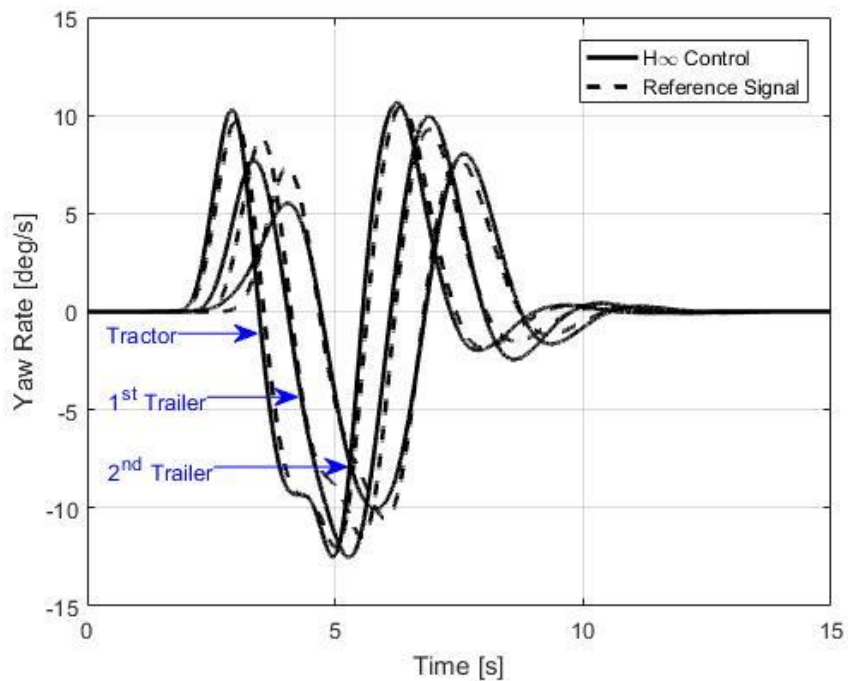


Figure 4.16 Time history of yaw rates for the  $H^\infty$  controlled vehicle, and the reference signals under the DLC maneuver.

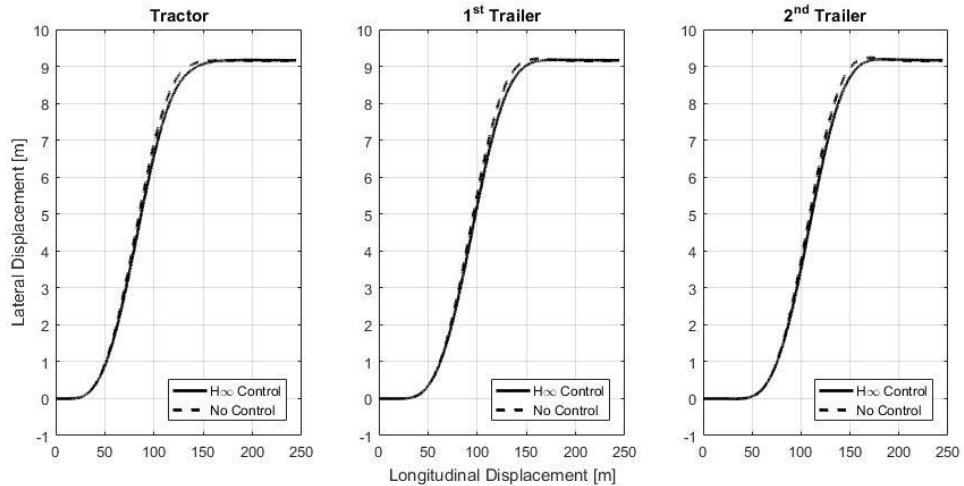


Figure 4.17 Trajectories of the H<sub>∞</sub> controlled vehicle and the baseline vehicle under the SLC maneuver.

The trajectories of the three vehicle units under the SLC and DLC maneuvers is shown in Fig. 4.17 and 4.18. Although noticeable variation in the vehicle’s path is observed under the DLC maneuver (see Fig. 4.18), it is apparent that the H<sub>∞</sub> controlled vehicle follows the intended path accurately. Moreover, the results reveal that the H<sub>∞</sub> controlled vehicle has reduced overshoot under both maneuvers. The H<sub>∞</sub> controller simultaneously enhances the vehicle’s dynamic behavior and ensures intended path following.

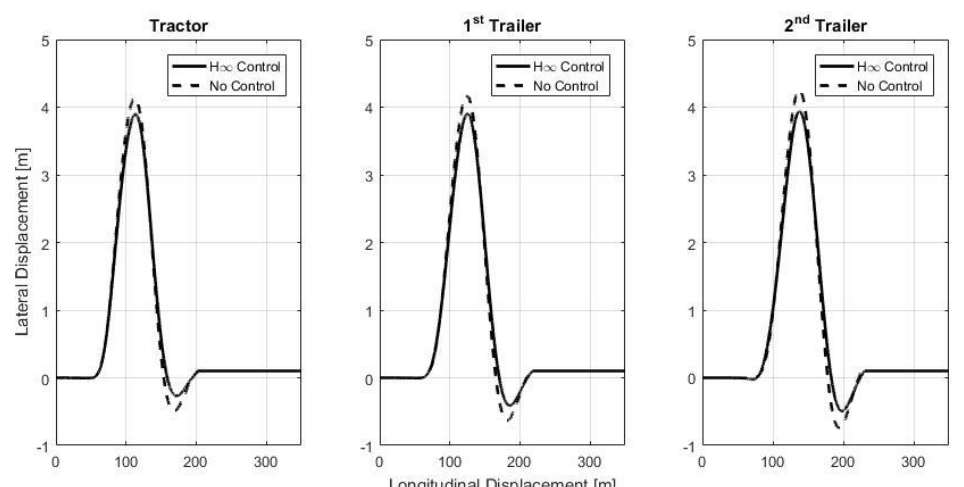


Figure 4.18 Trajectories of the H<sub>∞</sub> controlled vehicle and the baseline vehicle under the DLC maneuver.

## **4.3. ATS Hydraulic Actuation (AHA) System Integration**

### **4.3.1. Introduction**

So far, all ATS related studies have assumed that the actuation system can generate the control signals (ATS angles) desired by the controller. However, in the real world, such an assumption may be irrational. In certain complex scenarios, the demands posed by the controller on the actuation system can be beyond its physical limitations. Thus, this research accounts for the effects of actuator dynamics on the overall effectiveness of the ATS system(s) by integrating an actuator model in the control system.

The ATS Hydraulic Actuation (AHA) system developed in Section 3.4 is integrated with the controllers. A PID controller is employed to ensure that the desired ATS angles are generated by the AHA system. Moreover, the actuator response characteristics are studied for both LQR and  $H^\infty$  controllers. This approach will aid in assessing the vehicle's behavior and predicting achievable results.

### **4.3.2. PID Controller**

Since their invention in the early 1900's, Proportional-Integral-Derivative (PID) control has been the most commonly used control scheme [97]. The simplicity, functionality, and feasibility offered by PID is unparalleled. Thus, most industrial controllers are implemented using PID algorithms [97]. In this study, PID controller assists the AHA system to generate the desired ATS angles, where each active axle consists of an individual PID controller. The PID gains are tuned using the Simulink environment.

### 4.3.3. Simulation Results

This sub-section presents the simulation results for the LQR and  $H^\infty$  controlled vehicles integrated with the AHA system. The lateral acceleration and yaw rate responses of the controlled vehicle(s) are compared to analyze the effects of the actuator dynamics on the vehicle's directional performance. Moreover, the desired ATS angles and the actual ATS angles generated by the AHA system are cross-examined. Fig. 4.19 to 4.24 show the results for the LQR controller, whereas Fig. 4.25 to 4.30 illustrate the comparative results for the  $H^\infty$  controller.

Fig. 4.19 and 4.20 show the time history of lateral acceleration for the LQR controlled vehicle and AHA integrated LQR controlled vehicle under the single-lane change (SLC) and double-lane change (DLC) maneuvers. Both figures show almost identical response and excellent synchronization. Moreover, the yaw rate responses for the LQR controlled and AHA integrated vehicles, shown in Fig. 4.21 and 4.22, display similar behavior.

Fig. 4.23 and 4.24 illustrate the tracking performance of individual axles of the ATS system under both SLC and DLC maneuvers. It is evident that each active axle can accurately produce the ATS angles demanded by the LQR controller. Results suggest that actuation system is capable of meeting the demands of the controller under both the maneuvers. Hence, the desired lateral acceleration and yaw rate responses are achievable as demanded by the control system.

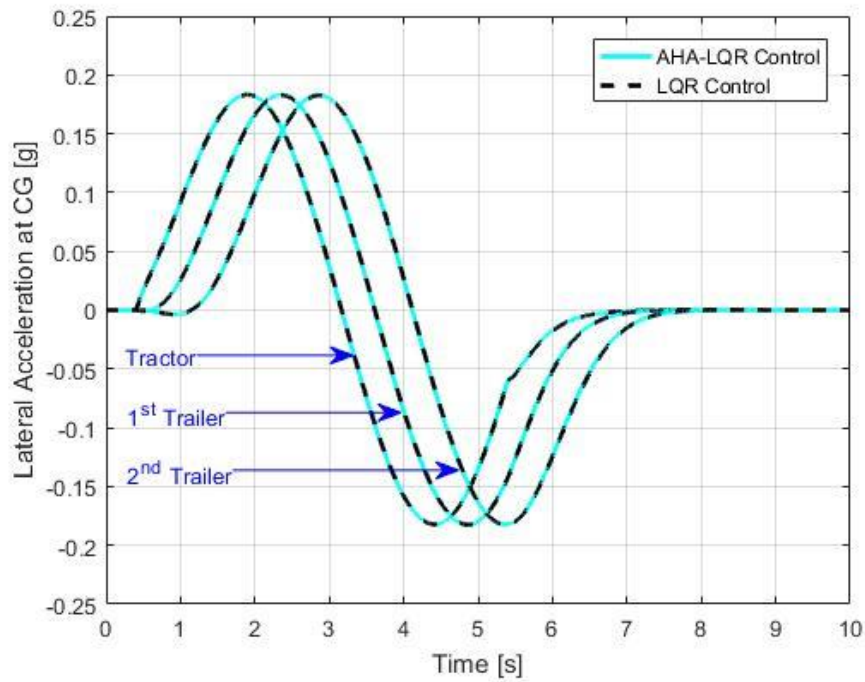


Figure 4.19 Time history of lateral accelerations for the AHA-LQR controlled vehicle and the LQR controlled vehicle under the SLC maneuver.

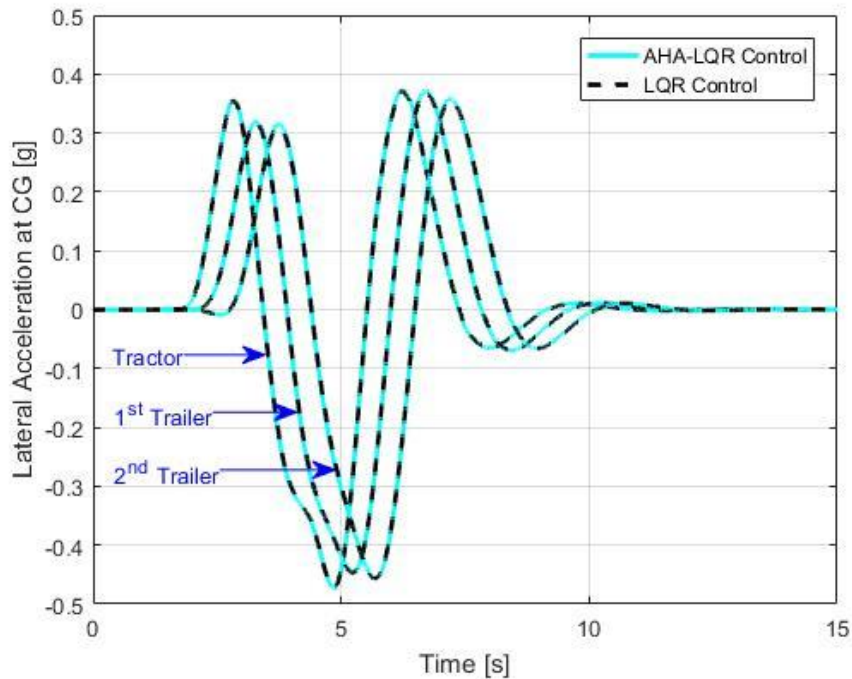


Figure 4.20 Time history of lateral accelerations for the AHA-LQR controlled vehicle and the LQR controlled vehicle under the DLC maneuver.

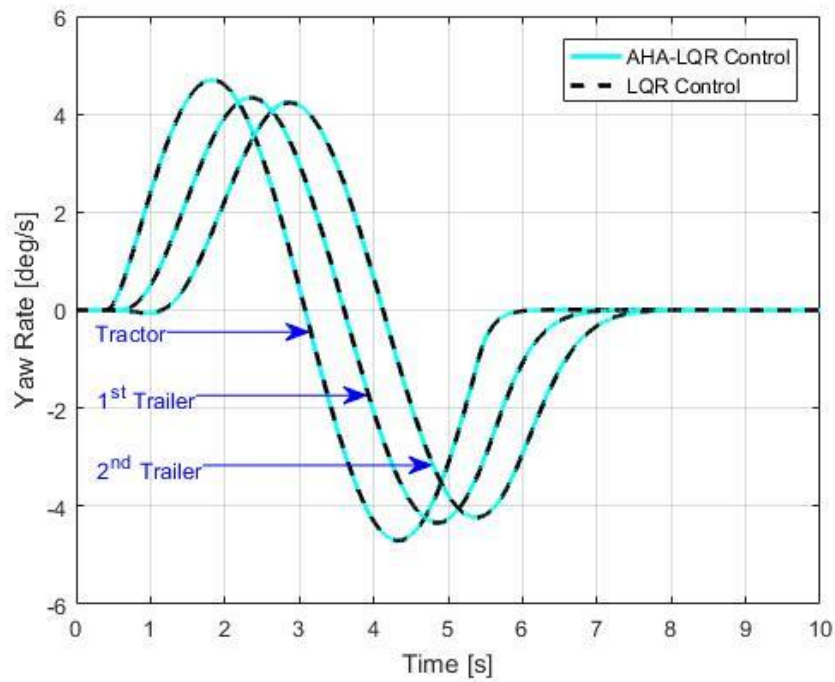


Figure 4.21 Time history of yaw rates for the AHA-LQR controlled vehicle and the LQR controlled vehicle under the SLC maneuver.

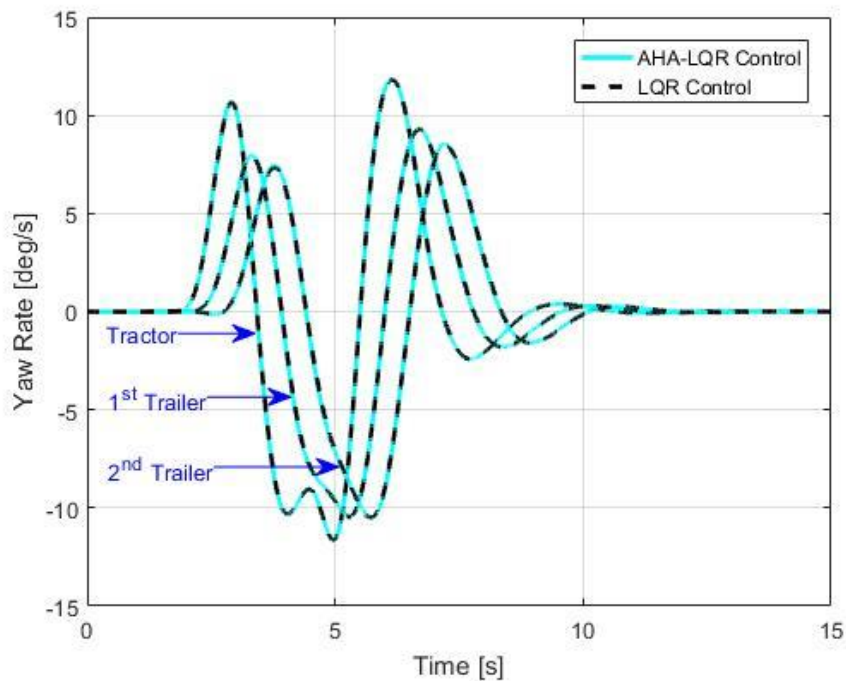


Figure 4.22 Time history of yaw rates for the AHA-LQR controlled vehicle and the LQR controlled vehicle under the DLC maneuver.

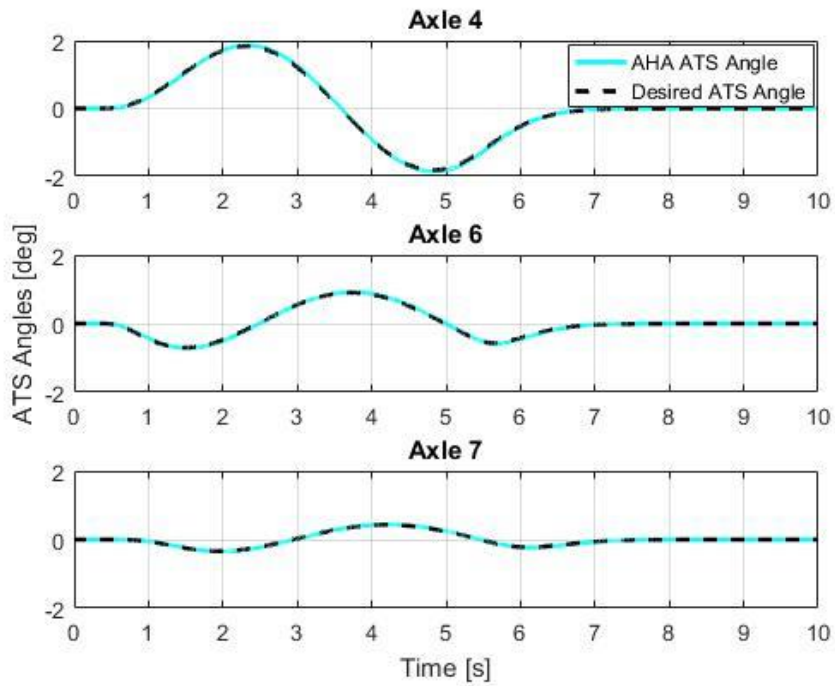


Figure 4.23 Time history of ATS angles achieved by the AHA-LQR system, and the desired ATS angles under the SLC maneuver.

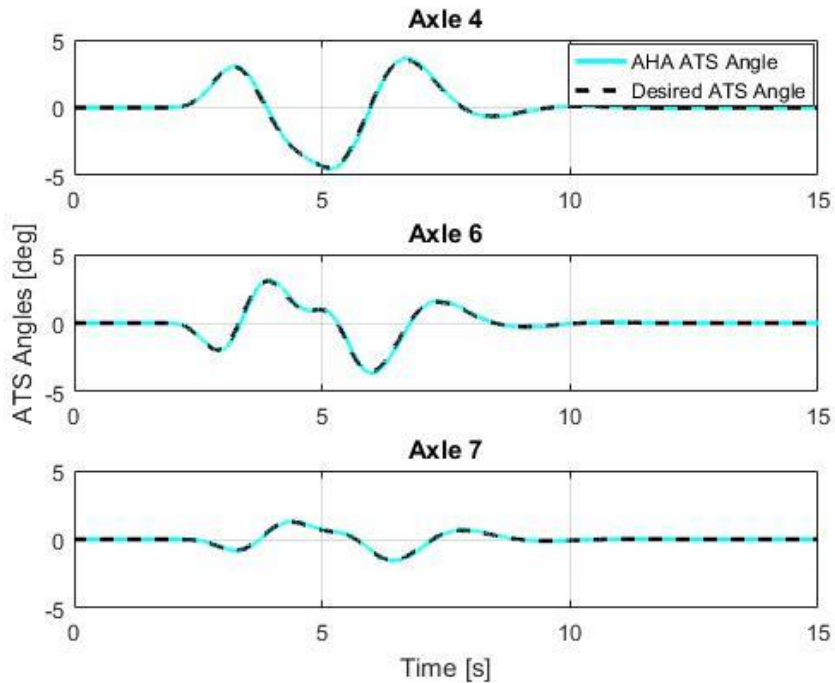


Figure 4.24 Time history of ATS angles achieved by the AHA-LQR system, and the desired ATS angles under the DLC maneuver.

Comparative results of the  $H^\infty$  controlled vehicle and the AHA integrated  $H^\infty$  controlled vehicle are shown in Fig. 4.25 to 4.30. Fig. 4.25 and 4.26 illustrate the lateral acceleration response of the vehicles under the SLC and DLC maneuvers respectively. Even though both figures indicate similar response characteristics, noticeable difference is observed under the DLC maneuver, particularly in the second trailer's response.

Yaw rate response of the vehicles under both the maneuvers, renders similar results. Fig. 4.27 suggests excellent agreement under the SLC maneuver. However, during the DLC maneuver (see Fig. 4.28), discrepancy is observed for the second trailer's response. Fig. 4.29 and 4.30 show the achieved ATS angles and desired angles demanded by the controller. Predictably, the AHA system demonstrates excellent synchronization for all active axles under the SLC maneuver. Under the DLC maneuver, however, deviations are observed.

Further analysis reveals that the deviations noticed in the lateral acceleration and yaw rate response of the second trailer are caused by Axle 4's inability to generate the desired ATS angles. Although the difference is small, it can significantly affect the dynamic performance of the vehicle. The noticeable discrepancies have been clearly marked in the relevant figures.

The dynamic responses of the AHA-integrated vehicle under the DLC maneuver help explain the limitations of a physical actuation system. Although the actuation system can precisely generate the ATS angles demanded by the complex  $H^\infty$  controller for a major duration of the DLC maneuver, it cannot meet the demands that are beyond its capability.

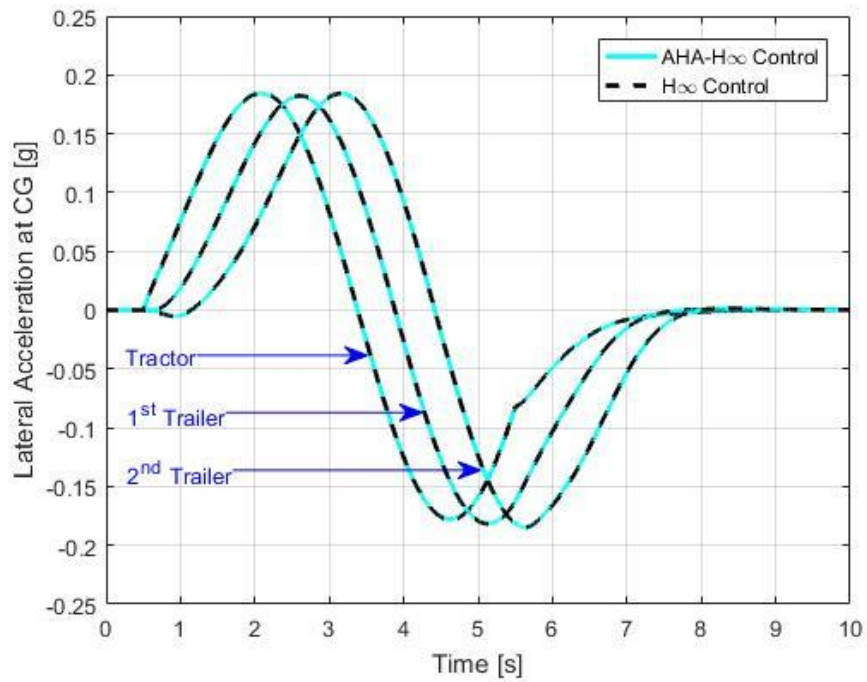


Figure 4.25 Time history of lateral accelerations for the AHA-H $\infty$  controlled vehicle and the H $\infty$  controlled vehicle under the SLC maneuver.

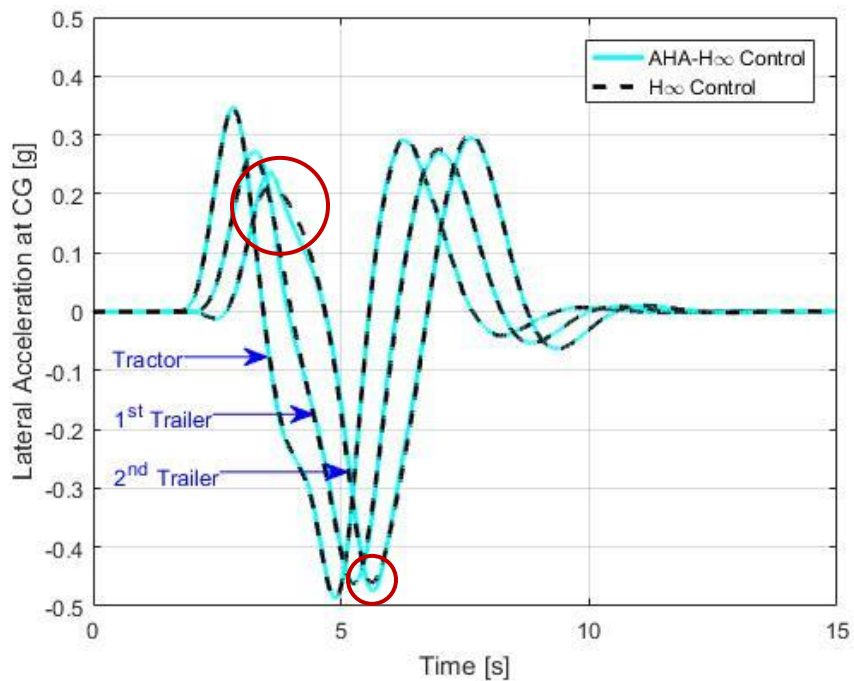


Figure 4.26 Time history of lateral accelerations for the AHA-H $\infty$  controlled vehicle and the controlled H $\infty$  vehicle under the DLC maneuver.

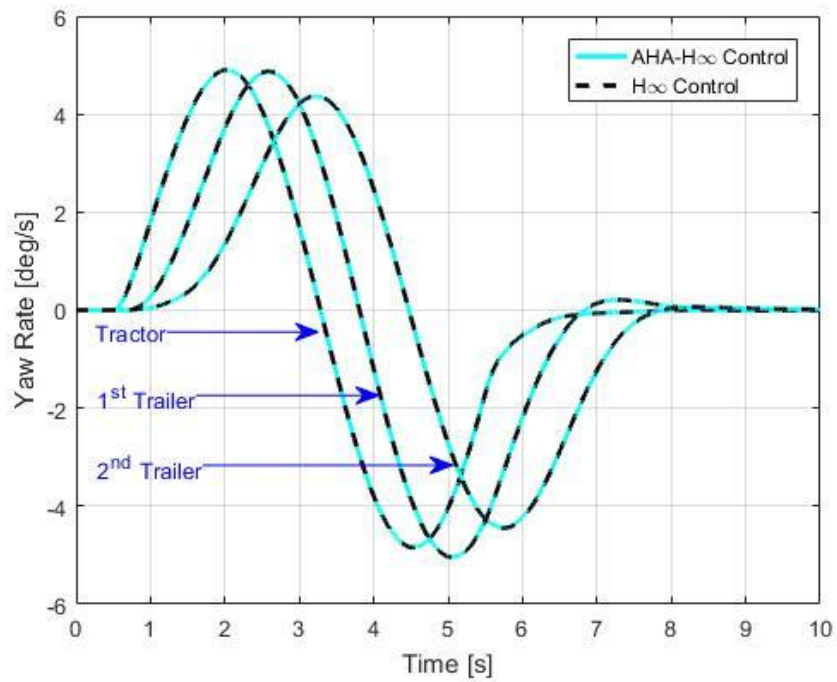


Figure 4.27 Time history of yaw rates for the AHA- $H^\infty$  controlled vehicle and the  $H^\infty$  controlled vehicle under the SLC maneuver.

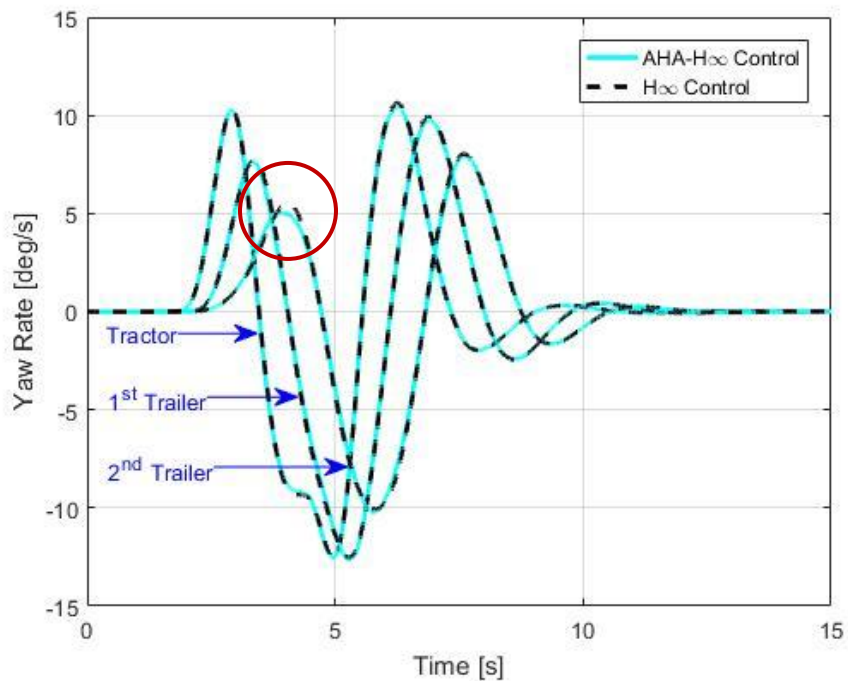


Figure 4.28 Time history of yaw rates for the AHA- $H^\infty$  controlled vehicle and the  $H^\infty$  controlled vehicle under the DLC maneuver.

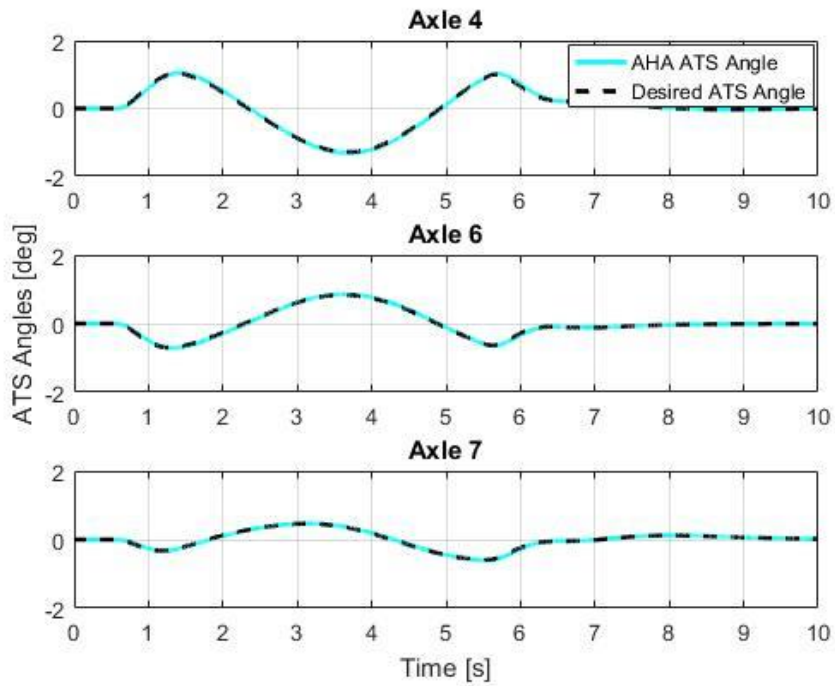


Figure 4.29 Time history of ATS angles achieved by the AHA- $H^\infty$  system, and the desired ATS angles under the SLC maneuver.

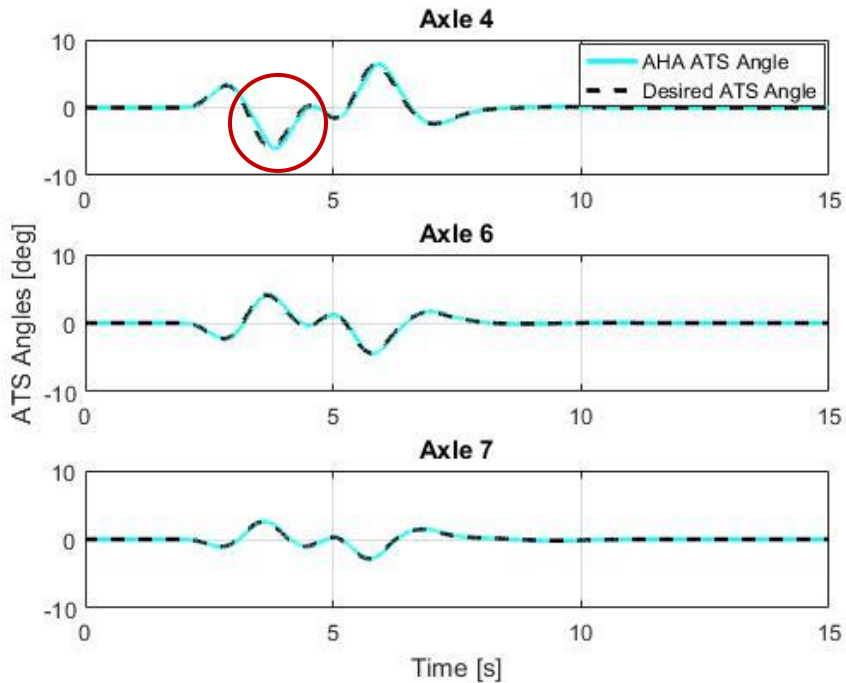


Figure 4.30 Time history of ATS angles achieved by the AHA- $H^\infty$  system, and the desired ATS angles under the DLC maneuver.

Results presented in Fig. 4.19 to 4.30 for the SLC and DLC maneuvers indicate reasonable overall agreement between the AHA system and the controller's demands. Despite the deviation observed in the AHA-integrated  $H^\infty$  controlled vehicle under the DLC maneuver, no major differences are observed in the vehicle's dynamic response. Thus, to examine the limitations of the AHA system and to investigate the effects of actuator dynamics, the demand on the AHA system is further increased. To generate this increased demand, the  $H^\infty$  controller and the DLC maneuver are selected, and the vehicle forward speed is increased from 88 km/h to 120km/h.

Fig. 4.31 and 4.32 illustrate the lateral acceleration and yaw rate responses of the  $H^\infty$  controlled and AHA-integrated vehicles under the DLC maneuver. Both figures clearly indicate large deviations in the dynamic performance characteristics of the two vehicles. It is apparent that AHA-integrated vehicle exhibits poor stability. Moreover, it is logical to expect that during such a scenario the vehicle may experience rollover.

Further investigation of the tracking performance of the individual active axles reveals that the poor stability of AHA-integrated vehicle results from diminished performance of axles 4 and 6. Large differences are observed between the achieved and desired ATS angles for both axles. Fig. 4.33 provides clear evidence that the AHA system is incapable of meeting the controller demands under the DLC maneuver and a vehicle forward speed of 120 km/h.

Since the entire ATS system is interconnected, a small deviation in the expected performance of one active axle increases the demand on the other axles. As a result, the whole vehicle experiences poor stability. Moreover, it is possible in certain scenarios with high controller demands, that the ATS controlled vehicle may exhibit inferior stability characteristics compared to the baseline vehicle without ATS.

The results presented in this section clearly stipulate that integrating the actuation system within the control system generates reliable results. Moreover, the baseline vehicle provides an incomplete picture of the achievable results, whereas by accounting the actuator limitations, the AHA-integrated controlled vehicle brings the results closer to reality.

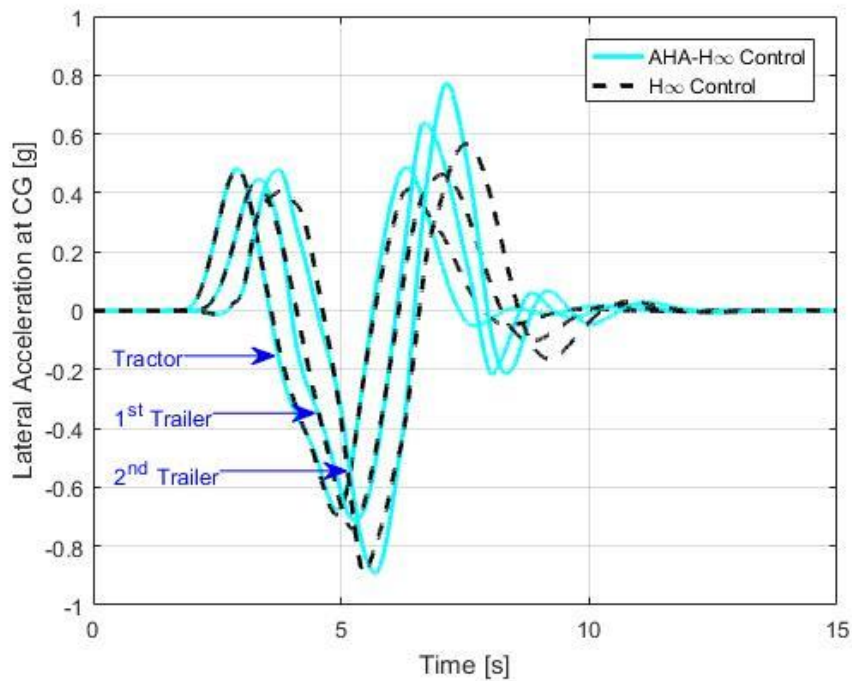


Figure 4.31 Time history of lateral accelerations for the AHA-H $\infty$  controlled vehicle and the H $\infty$  controlled vehicle under the DLC maneuver at 120 km/h.

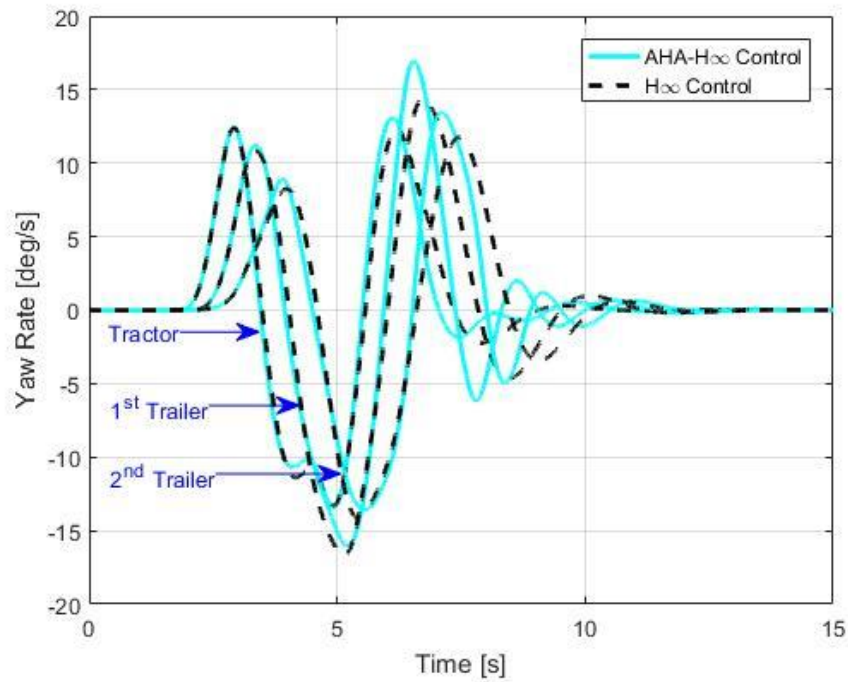


Figure 4.32 Time history of yaw rates for the AHA- $H^\infty$  controlled vehicle and the  $H^\infty$  controlled vehicle under the DLC maneuver at 120 km/h.

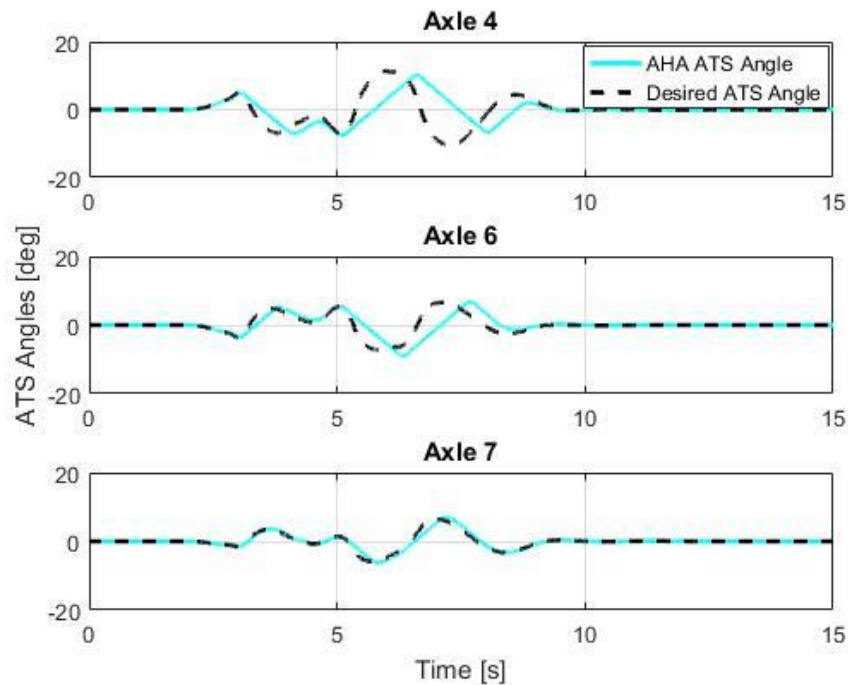


Figure 4.33 Time history of ATS angles achieved by the AHA- $H^\infty$  system, and the desired ATS angles under the DLC maneuver at 120 km/h.

## **4.4. Observer Selection**

### **4.4.1. Introduction**

Observers are primarily employed in conjunction with state-feedback (LQR) controllers. Although state-feedback control is a powerful tool, it is based on the assumption that all state variables are measurable and their measurements are available [98]. However, in reality measuring all state variables is impractical. Observers allow estimation of the state variables that are necessary to implement state-feedback control. Based on known inputs and the available output measurements, the observer can predict state variables. Despite the tendency of observer predictions to exhibit deviation from the actual outputs, the information gained from observers is valuable. Additionally, observers can be employed as redundant sensors for control or diagnostic purposes [26]. In this research, two observer techniques are explored for their effectiveness as analytical redundancy techniques for fault tolerant control.

As previously discussed (see Section 2.5.1), observer and state-estimation based techniques are widely employed to develop effective and reliable fault tolerant systems. This research extensively employs observers for defining the FTC framework of ATS systems. This section focuses on comparing the suitable observer techniques for the FTC-ATS framework, i.e. Luenberger Observer and Kalman Filter. Thus, in the subsequent sub-sections, both observer techniques are introduced. Thereafter, the effectiveness of both observer techniques is compared using simulations under varied conditions. Additionally, the effects of sensor dynamics and noise are considered.

## 4.4.2. Observer Design Techniques

### 4.4.2.1. Luenberger Observer

The observer is a dynamic system designed to asymptotically converge to the actual estimate of the state variables [98, 99]. Eq. (4.8) defines a linear state observer or Luenberger Observer [98].

$$\dot{\hat{x}}(t) = A\hat{x}(t) + Bu(t) + L[y(t) - \hat{y}(t)] \quad (4.8)$$

$$\hat{y}(t) = C\hat{x}(t) + Du(t) \quad (4.9)$$

where,  $u(t)$  and  $y(t)$  are the known inputs and measurements,  $\hat{x}(t)$  depicts the estimated states,  $A, B$  are the system matrices which define the system to be observed,  $[y(t) - \hat{y}(t)]$  is the error between the actual and estimated measurement(s), and  $L$  denotes the observer gain matrix.  $L$  is designed to asymptotically converge the state estimate  $\hat{x}(t)$  to the actual state  $x(t)$ . The final observer equation is obtained by substituting Eq. (4.9) into (4.8).

$$\dot{\hat{x}}(t) = A\hat{x}(t) + Bu(t) + L[y(t) - C\hat{x}(t) - Du(t)] \quad (4.10)$$

$$\dot{\hat{x}}(t) = A\hat{x}(t) + Bu(t) + Ly(t) - LC\hat{x}(t) - LDu(t) \quad (4.11)$$

$$\dot{\hat{x}}(t) = (A - LC)\hat{x}(t) + (B - LD)u(t) + Ly(t) \quad (4.12)$$

Eq. (4.12) defines the final observer equation. The observer will be asymptotically stable if the matrices  $(A - LC)$  and  $(B - LD)$  that governs the error dynamics have negative eigenvalues [98, 99]. The eigenvalues of the observer strictly depend on the observer gain matrix  $L$ .

The primary objective in observer design is to obtain the gain matrix. Luenberger Observer and Kalman Filter techniques follow different approaches for obtaining the observer gain matrix. In Luenberger Observer design, the gain matrix is obtained by placing the poles of the observer at the desirable locations [98, 99]. Ideally, the poles of the observer should be faster than the system it observes. Fast poles aid the observer to converge to the true states quickly [99]. However, an observer with very fast poles is susceptible to measurement noise [99]. Therefore, the observer gains are tuned based on their application. Observer gain matrix for Kalman Filter is obtained by solving the Algebraic-Riccati Equations, and is discussed in the following sub-section.

#### 4.4.2.2. Kalman Filter

A Kalman filter observer can be defined by the generalized observer equation (see Eq. (4.8)). However, the observer gain matrix is computed by using process noise and measurement noise covariance data. To establish clear distinction between Luenberger Observer and Kalman Filter, their gain matrices will be denoted by symbols  $L$  and  $K$  respectively.

Consider a continuous-time system (see Eq. (4.13)) subjected to process and measurement noise.

$$\begin{cases} \dot{x} = Ax + Bu + Gw \\ y = Cx + Du + Hw + v \end{cases} \quad (4.13)$$

where,  $w$  is the process noise, and  $v$  the measurement noise, satisfying the following conditions.

$$E(ww^T) = Q_k, \quad E(vv^T) = R_k \quad (4.14)$$

In the Kalman Filter,  $Q_k$  and  $R_k$  represent the process noise and measurement noise covariance matrices respectively.  $Q_k$  reflects the uncertainties, un-modeled dynamics or unknown inputs present in the assumed state model, and is vital to the observer design [100].  $Q_k$  is selected based on the observer's application and the effects of process noise on the system. A larger value of  $Q_k$  effectively models the process uncertainties. However, such an observer risks losing information gained from the measurements. Whereas, a small value retains the learning potential from the measurements but may leave the estimations redundant [100]. For simulation purposes,  $Q_k$  can be assumed as any value greater than 0, later the values can be adaptively updated.  $R_k$  is the covariance matrix of the measurement noise, which is assumed Gaussian distributed. Generally, the initial value for  $R_k$  is assumed close to zero. Later,  $R_k$  is fine-tuned for desired performance [100]. Conversely, a reliable estimate for  $R_k$  may be obtained from the sensor noise data.

### **4.4.3. Simulation Results**

#### **4.4.3.1. Sensor Measurements**

This sub-section presents the comparative performance of the Luenberger Observer and Kalman Filter under varied test conditions. Additionally, the results reflect the effects of sensor dynamics and noise on observer performance. To investigate the observers' performance, the linear 4DOF B-Train double model (see Section 3.2) is employed. Besides as stated in Section 4.4.1, measuring all state variables is impractical. Hence, it is assumed that only the lateral acceleration measurements of the three vehicle units are available, whereas the vehicle's yaw rates are estimated.

In real systems, the measurements are obtained using physical sensors. Since sensors themselves are physical systems with a certain time delay, variations are inevitable between true outputs and measured signals. Moreover, sensor measurements are inherently noisy. Therefore, the lateral acceleration measurements employed in this sub-section are obtained from an accelerometer's dynamic model defined by a first-order high-pass filter [79]. In the subsequent sub-sections, the measurements are further corrupted using additive noise to effectively analyze observes performance.

$$\begin{cases} \dot{x}_s = a_s(a_y - x_s) \\ a_{ys} = k_s(a_y - x_s) + v \end{cases} \quad (4.15)$$

where,  $a_s$  depicts the sensor eigenvalues,  $a_y$  the true lateral acceleration,  $x_s$  the sensor states,  $a_{ys}$  the sensor output,  $k_s$  the high-pass filter gain, and  $v$  the additive measurement noise. The sensor model is adopted from [79].

Fig. 4.34 to 4.37 illustrate the performance of the Luenberger Observer and Kalman Filter using sensor measurements in the absence of noise. The output (Lateral Acceleration) prediction of both observers under the SLC and DLC maneuvers is shown in Fig. 4.34 and 4.35 respectively. The performance variation between the two observers is evident. The Kalman Filter can accurately predict the system's true output for all vehicle units, whereas Luenberger Observer predictions illustrate notable differences. The yaw rate (state) estimation results demonstrated in Fig 4.36 and 4.37 indicate similar tendencies. Although, the Luenberger Observer can predict tractor's yaw rate, trailer's yaw rate estimation is inaccurate. Whereas, the Kalman Filter demonstrates excellent convergence to true solution.

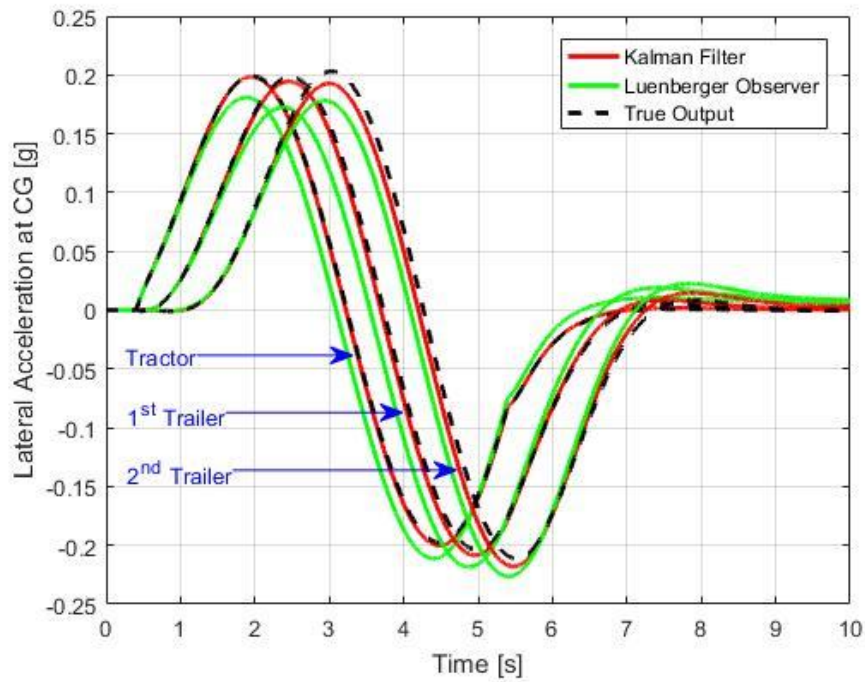


Figure 4.34 Time history of lateral acceleration predictions for the Kalman Filter and Luenberger Observer, and the true outputs under the SLC maneuver using sensor measurements.

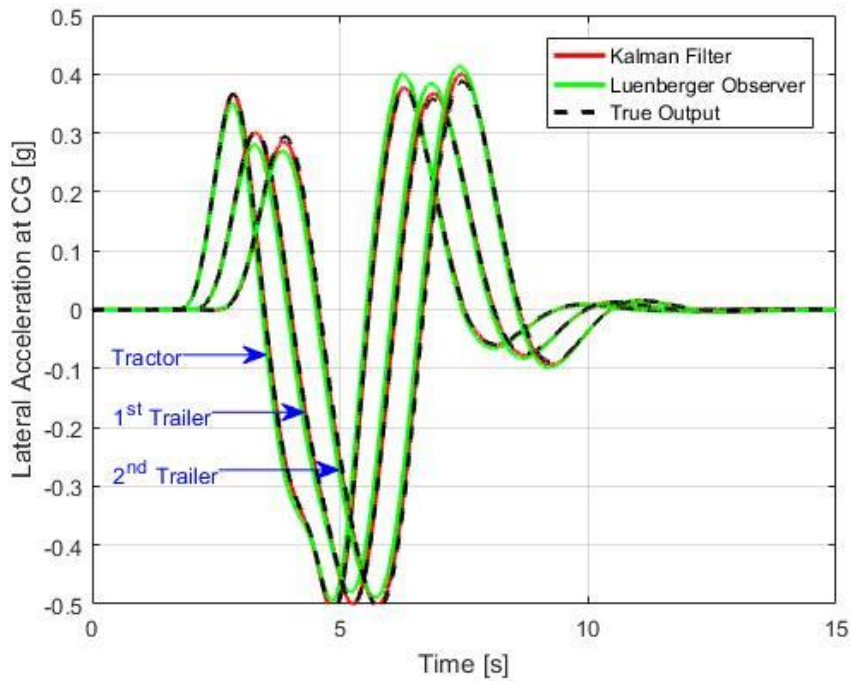


Figure 4.35 Time history of lateral acceleration predictions for the Kalman Filter and Luenberger Observer, and the true outputs under the DLC maneuver using sensor measurements.

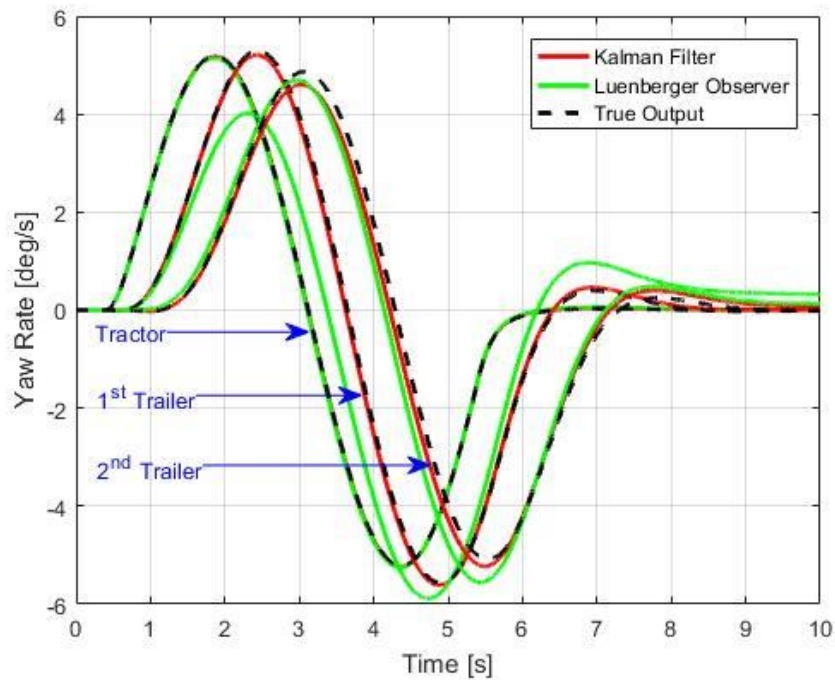


Figure 4.36 Time history of yaw rate predictions for the Kalman Filter and Luenberger Observer, and the true outputs under the SLC maneuver using sensor measurements.

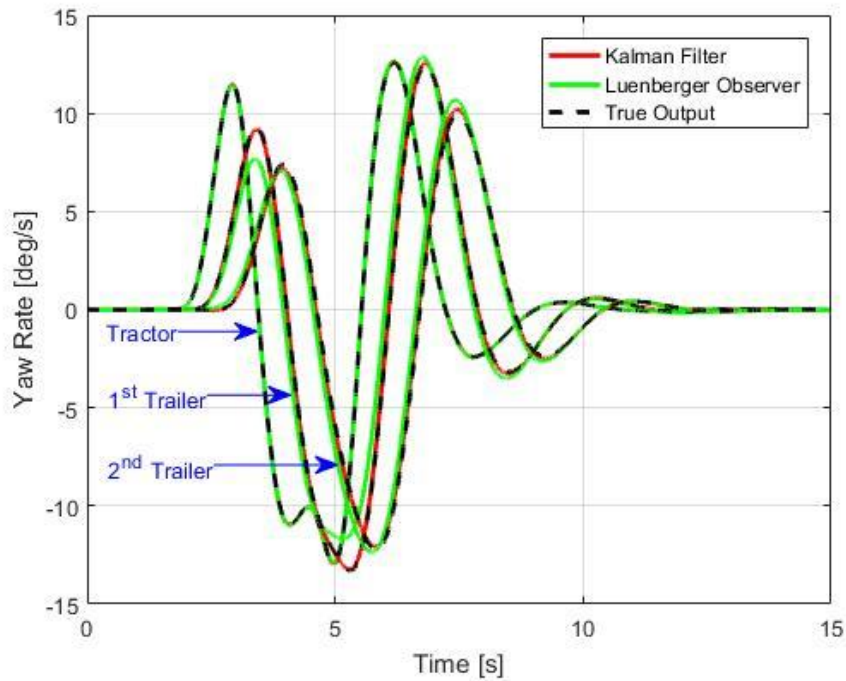


Figure 4.37 Time history of yaw rate predictions for the Kalman Filter and Luenberger Observer, and the true outputs under the DLC maneuver using sensor measurements.

#### **4.4.3.2. Sensor Measurements with Additive Noise**

An effective observer is expected to accurately predict the system's behavior in presence of noise. Thus, both Luenberger Observer and Kalman Filter are further evaluated by using the sensor measurements with additive noise. In the simulations, the sensor measurements obtained through the sensor model (see Section 4.4.3.1), are corrupted with white noise. Even though physical systems never experience white noise, it provides a useful theoretical approximation [101].

Fig. 4.38 to 4.41 display the prediction performance of both observers by using sensor measurements with additive noise. The lateral acceleration predictions under the SLC and DLC maneuvers is displayed in Fig 4.38 and 4.39 respectively. Results indicate that the Kalman Filter's predictions are accurate and display excellent agreement with the true outputs. Whereas, the Luenberger Observer's performance is significantly affected by the presence of noise.

Fig. 4.40 and 4.41 show the yaw rate estimates of the two observers under the SLC and DLC maneuvers respectively. Even though the yaw rate estimates of the Luenberger Observer, demonstrate better agreement compared to its lateral acceleration predictions, the Kalman Filter illustrates superior performance under both the maneuvers.

Altogether, the Kalman Filter displays superior noise rejection and output prediction. Moreover, it is apparent that the Luenberger Observer is more susceptible to noise. Although the Luenberger Observer's noise rejection characteristics can be enhanced by re-tuning the gain matrix, it may further deteriorate its estimation performance.

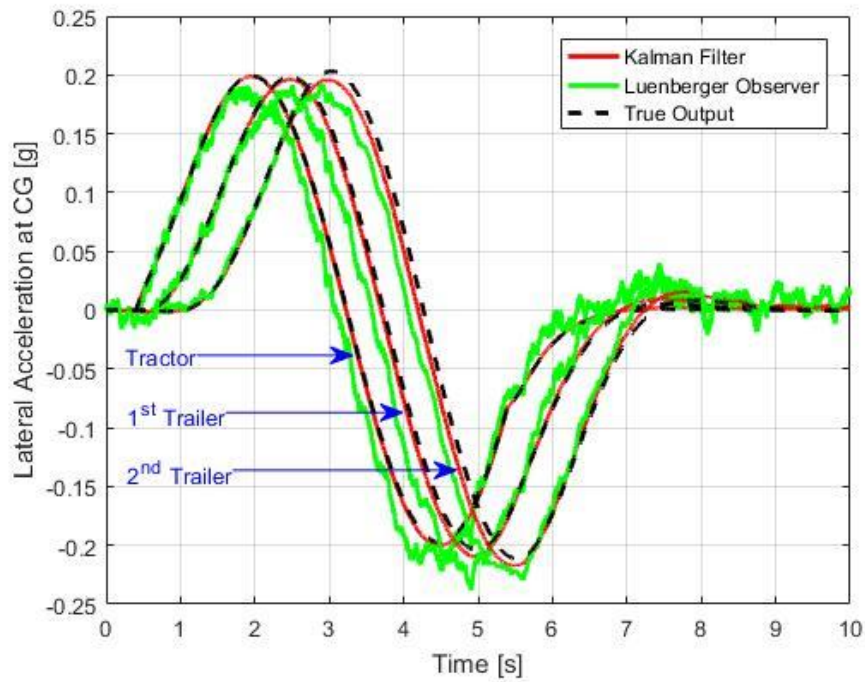


Figure 4.38 Time history of lateral acceleration predictions for the Kalman Filter and Luenberger Observer, and the true outputs under the SLC maneuver using sensor measurements with additive noise.

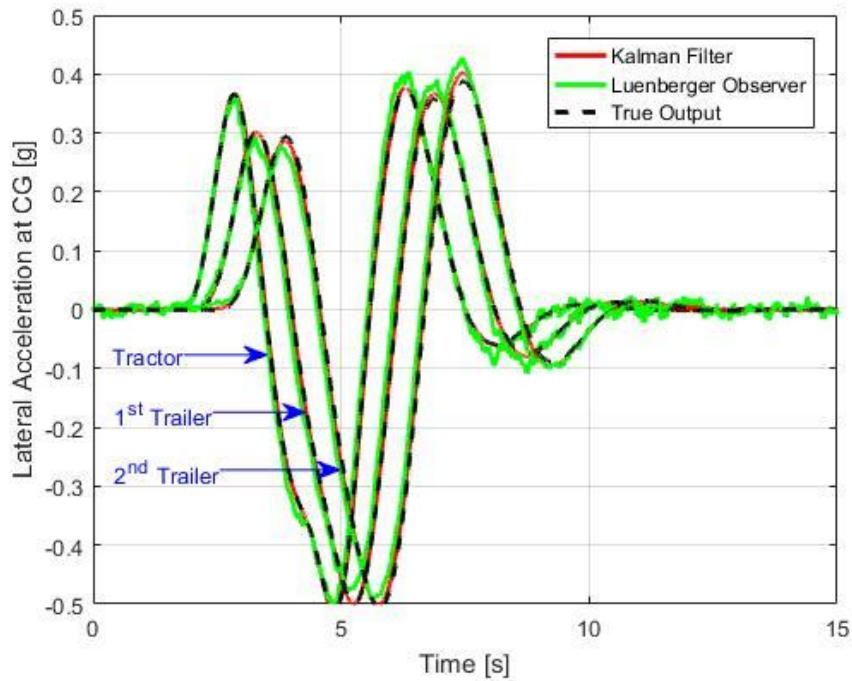


Figure 4.39 Time history of lateral acceleration predictions for the Kalman Filter and Luenberger Observer, and the true outputs under the DLC maneuver using sensor measurements with additive noise.

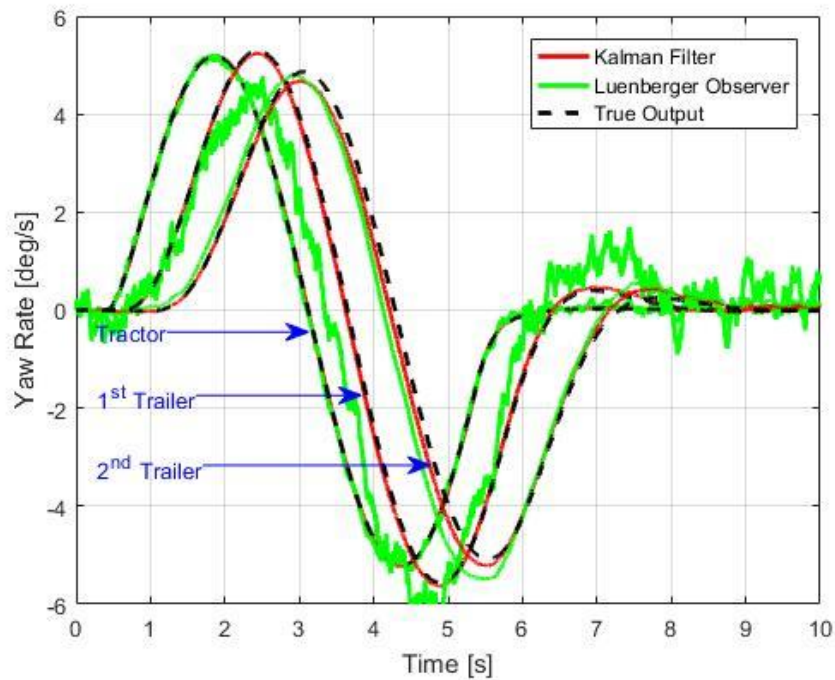


Figure 4.40 Time history of yaw rate predictions for the Kalman Filter and Luenberger Observer, and the true outputs under the SLC maneuver using sensor measurements with additive noise.

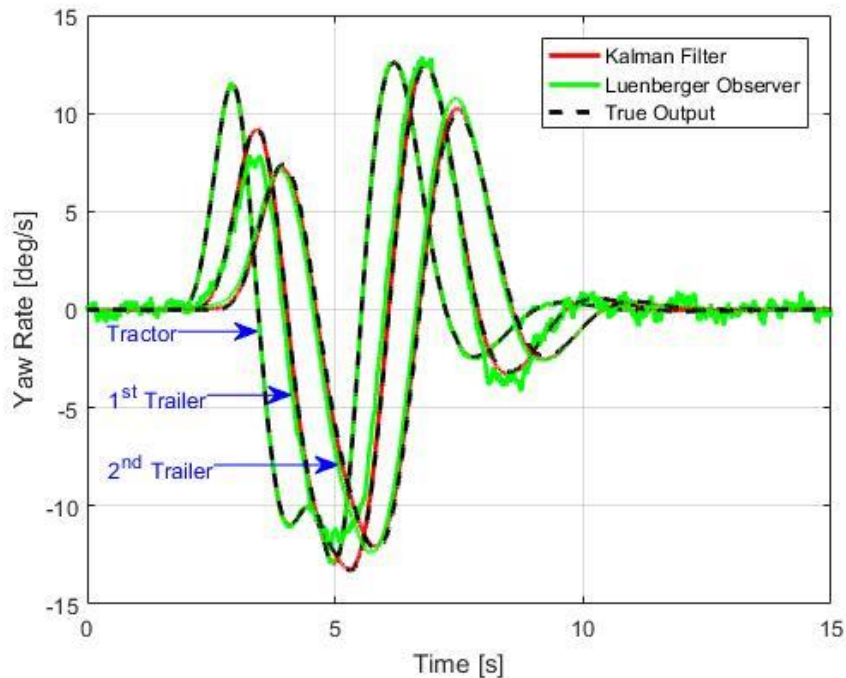


Figure 4.41 Time history of yaw rate predictions for the Kalman Filter and Luenberger Observer, and the true outputs under the DLC maneuver using sensor measurements with additive noise.

#### 4.4.3.3. Sensor Measurements with Additive Noise and different Initial Conditions

In the results presented in Sections 4.4.3.1 and 4.4.3.2, the observers and the vehicle model were simulated using the same initial states. Specifically, the initial states were zero. However, true observer performance cannot be evaluated when the observer and the observed system have the same initial states. Since, the observer is essentially a copy of the system, it is bound to produce similar results. Moreover, in practical applications, it is unlikely that the observer and physical system will have the same initial conditions. Therefore, in this sub-section, the Luenberger Observer and Kalman Filter are evaluated using different initial states than the vehicle model.

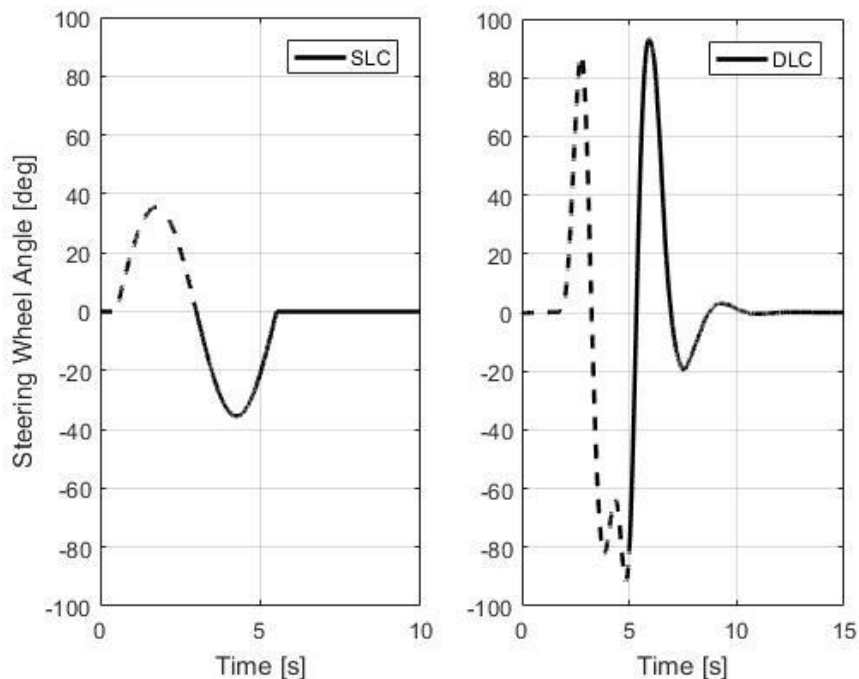


Figure 4.42 Time history of Steering Wheel Angles for the SLC and DLC maneuvers utilized for different initial conditions predictions.

Under both SLC and DLC maneuvers, the observers are initiated in the middle of the maneuver, when the vehicle model has non-zero initial states, whereas the observers have zero-initial states. Specifically, under the SLC maneuver the observers are initiated after 3 seconds, whereas for the DLC maneuver after 5 seconds. The steering input for both maneuvers is illustrated in Fig 4.42(see Section 3.3.2 for angular steering ratio). The dashed lines in the figures represent the part of the maneuver, which has already occurred. Whereas the solid-line signifies the remaining maneuver for which the observers are activated.

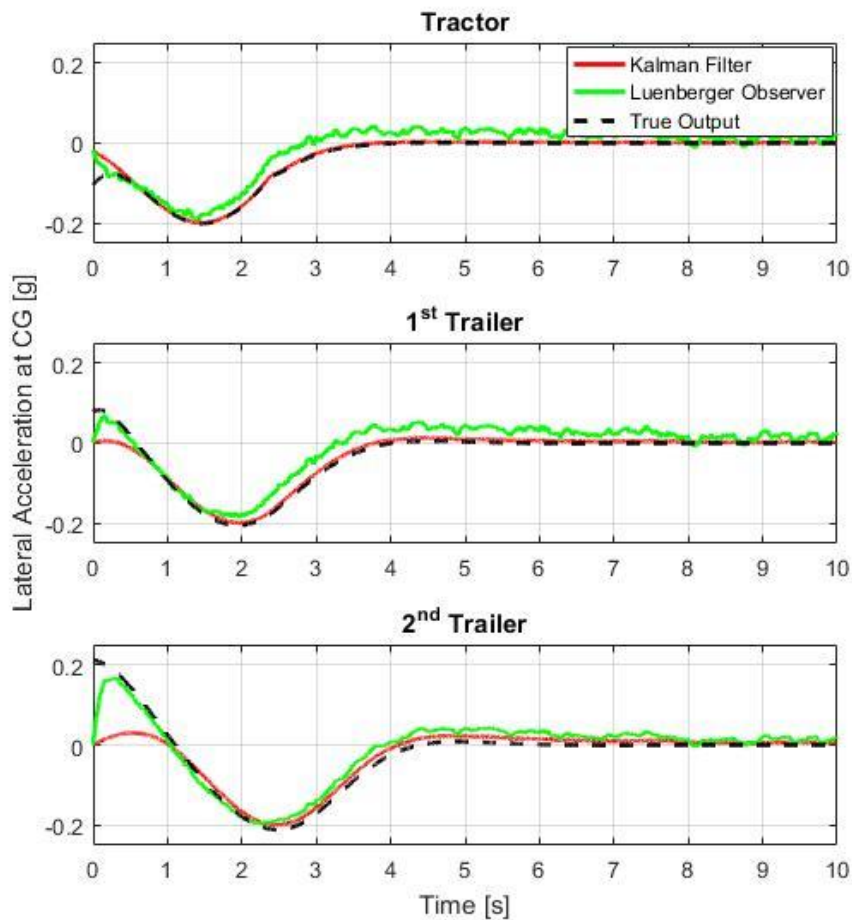


Figure 4.43 Time history of lateral acceleration predictions for the Kalman Filter and Luenberger Observer, and the true outputs under the SLC maneuver using sensor measurements with additive noise and different initial conditions.

Fig. 4.43 and 4.44 demonstrate the lateral acceleration predictions of the Luenberger Observer and Kalman Filter under the SLC and DLC maneuvers respectively. Result suggest that the Luenberger Observer rapidly converges to the true output. Conversely, the Kalman Filter is slower to reach the desired output, particularly, notable deviations are observed in the lateral acceleration prediction of both trailers during the initial seconds. Despite, the altered initial conditions both observers are able to converge to a good solution. However, the Luenberger Observer's poor noise handling capability is apparent in both figures.

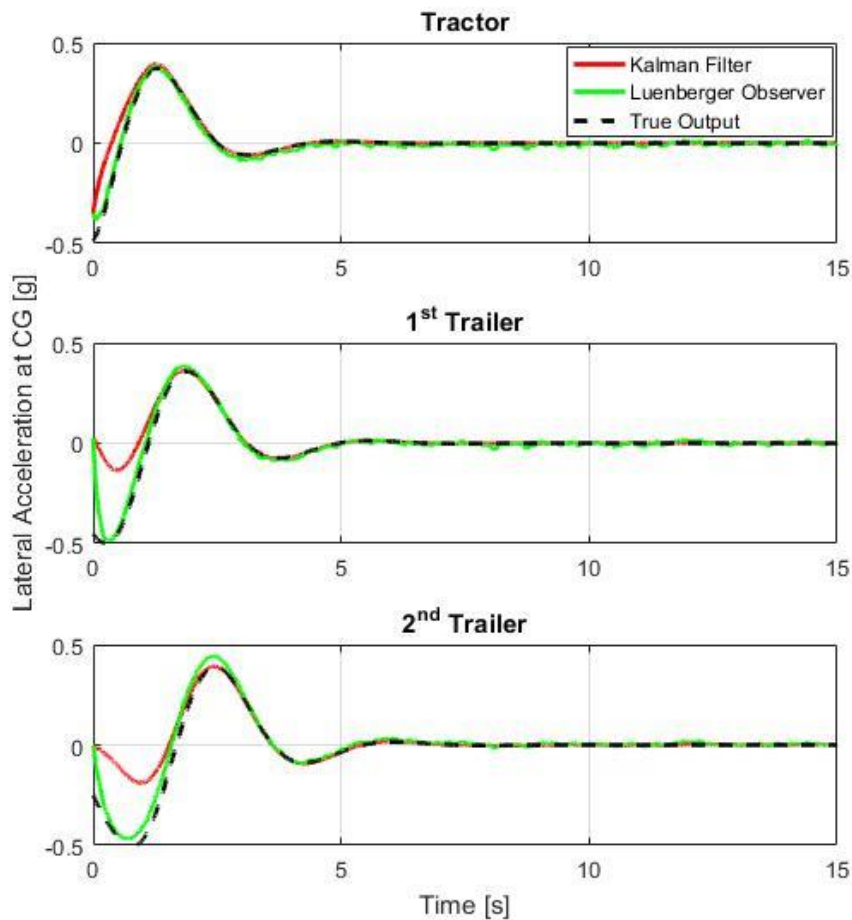


Figure 4.44 Time history of lateral acceleration predictions for the Kalman Filter and Luenberger Observer, and the true outputs under the DLC maneuver using sensor measurements with additive noise and different initial conditions.

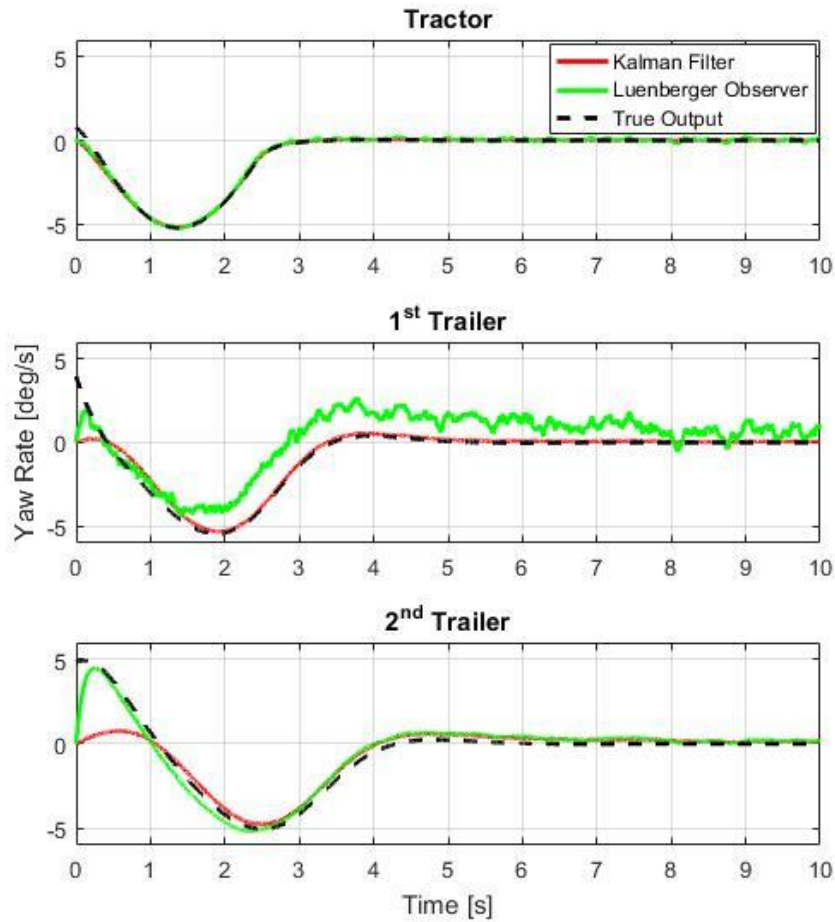


Figure 4.45 Time history of yaw rate predictions for the Kalman Filter and Luenberger Observer, and the true outputs under the SLC maneuver using sensor measurements with additive noise and different initial conditions.

Predictably, the yaw rate estimation results indicate similar behavior. Fig 4.45 and 4.46 suggest that, both Luenberger Observer and Kalman Filter can accurately estimate the tractor's yaw rate. The yaw rate estimates of the trailers suggest that Kalman Filter exhibits better overall performance. Although the Luenberger Observer responds faster, it is unable to predict the yaw rates of the trailers accurately especially under the SLC maneuver. The unreliable sensor measurements and additive noise deviate the Luenberger Observer from the system's true states.

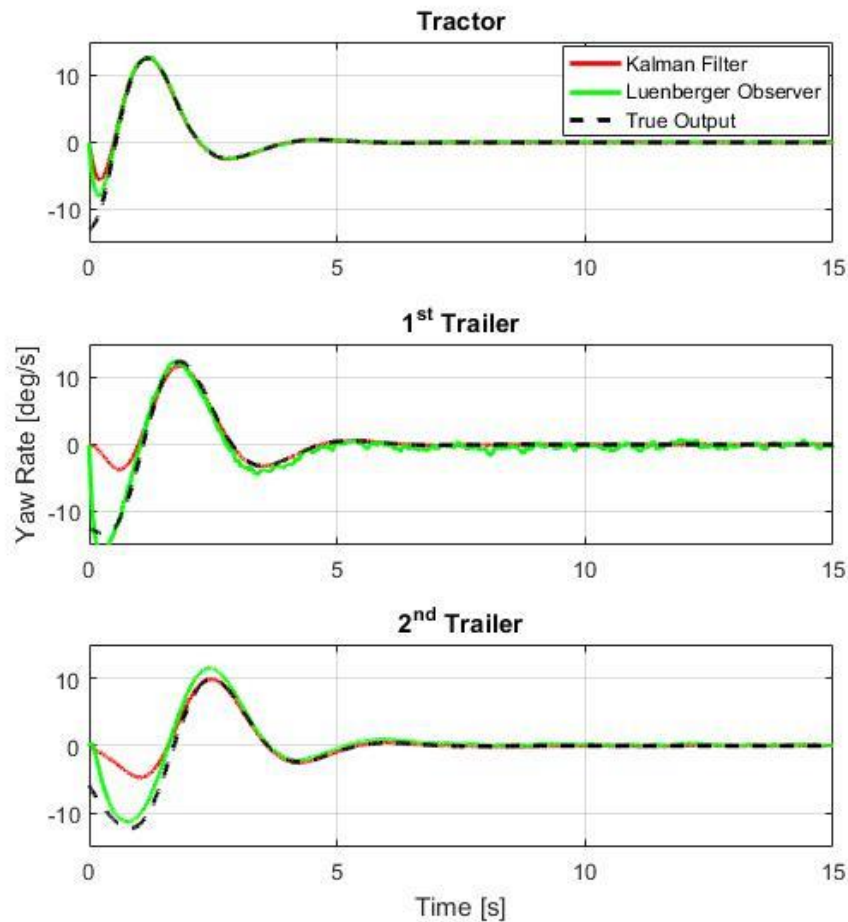


Figure 4.46 Time history of yaw rate predictions for the Kalman Filter and Luenberger Observer, and the true outputs under the DLC maneuver using sensor measurements with additive noise and different initial conditions.

Results obtained in this sub-section help establish that the Kalman Filter is superior to the Luenberger Observer. Even though, Luenberger Observer demonstrates fast error dynamics, it generates inconsistent results. Thus, with the intention to implement state-feedback control, the faster Luenberger Observer is recommended. Whereas, the Kalman Filter is suggested for generating accurate predictions especially for control and diagnosis systems.

## **4.5. FTC-ATS Framework**

### **4.5.1. Introduction**

So far, this chapter has discussed several control and diagnosis techniques. In Section 4.2, the efficacy of LQR and  $H^\infty$  control techniques for ATS systems was evaluated. Furthermore, in Section 4.4, Luenberger Observer and Kalman Filter were examined as potential diagnosis systems. Results obtained indicate that the  $H^\infty$  controller is more robust for real-life applications. The  $H^\infty$  controlled vehicle was able to negotiate both the SLC and DLC maneuvers, while demonstrating enhanced dynamic performance and path tracking. Whereas, Kalman Filter showed superior overall performance with regard to real-life scenarios, such as unreliable sensor measurements, noise etc. Since, a prime objective of this research is to aid real-life implementation of ATS systems, the  $H^\infty$  controller and Kalman Filter are chosen to formulate the fault tolerant control system.

In this section, the FTC framework for the ATS system is presented. Specifically, its salient features. First, a general overview of the FTC-ATS scheme is presented, involving the system diagram, sub-system distribution and the Fault Diagnosis and Detection (FDD) logic. Next, the design of dedicated observers for each sub-system is presented. Thereafter, the vehicle's fail-safe and fail-operational modes are discussed. Finally, the fault tolerant system is analyzed under simulated faults, such as multiple actuator malfunctions and sensor failures. The simulations are performed using TruckSim and Simulink environments.

#### 4.5.2. Overview of the FTC-ATS Framework

This sub-section presents a general overview of the FTC-ATS framework. To design the scheme, the entire vehicle, comprising of the Vehicle Model, ATS Controller, and ATS Hydraulic Actuation (AHA) system is segregated into relevant sub-systems. Each sub-system employs a dedicated observer. The sub-division considerably decreases the computational load on the FDD system, and allows implementation of the robust generalized observer scheme. The FTC-ATS scheme is inspired by Jeppesen and Cebon [69, 70]. Fig. 4.47 illustrates the vehicle as a set of sub-systems.

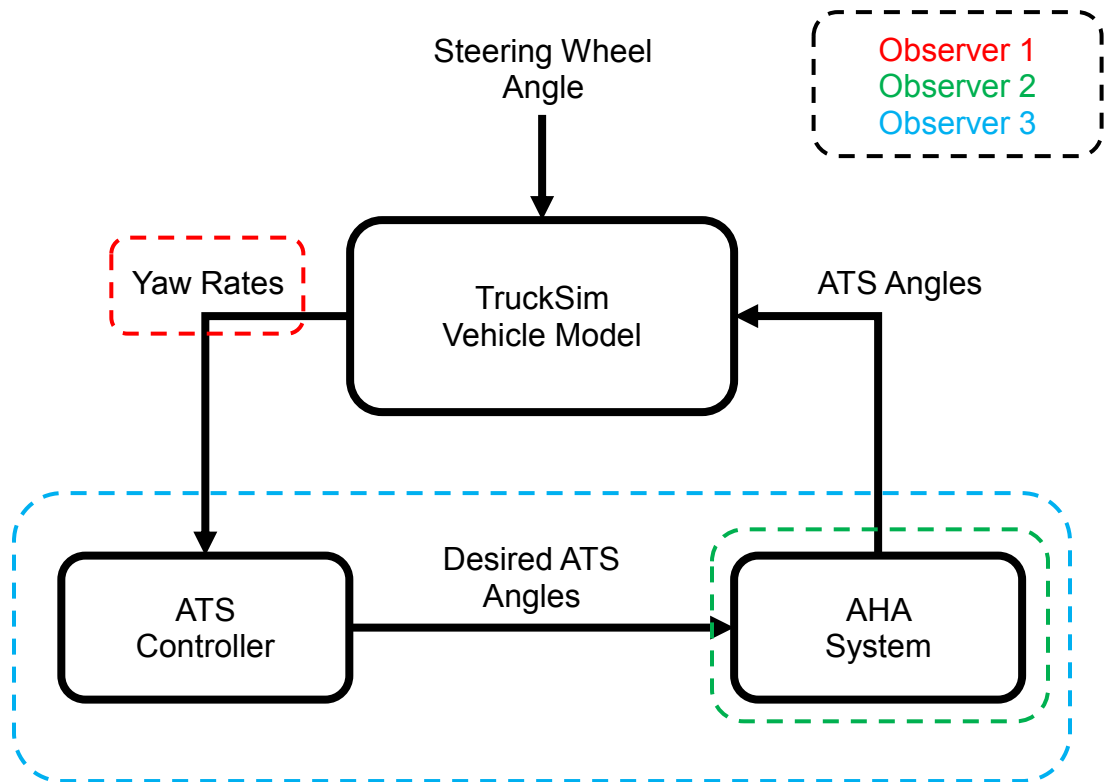


Figure 4.47 The schematic representation of the sub-systems structure of the vehicle.

As illustrated in Fig. 4.47 the entire vehicle is observed using three independent observers. Each observer is responsible for a dedicated sub-system. Observer 1 redundantly computes the yaw rate of the three vehicle units. Observer 2 is responsible for fault detection and diagnosis of the actuation (AHA) system. Whereas, Observer 3 observes the ATS Controller and the AHA system simultaneously. Mathematical models of all observers and their tracking performance is presented in Section 4.5.3.

### **4.5.3. Fault Detection and Diagnosis**

#### **4.5.3.1. Observer 1**

As explained in Section 4.2.2, the  $H^\infty$  ATS controller regulates the vehicle's yaw rates by minimizing the errors between the actual and desired yaw rates obtained from the reference model. Therefore, it is crucial to obtain an accurate measurement of the vehicle's yaw rates. Usually, a yaw rate sensor provides the required measurements. However, if the sensor(s) malfunctions or shuts down, the error signal sent to the controller will become large. The controller will try to compensate and reduce this error by applying additional ATS angles, which may lead to degraded system performance. Thus, it is necessary to generate a reliable estimation of the vehicle's yaw rates that can be employed in such a failure scenario. A kinematic estimate of vehicle's yaw rate can be obtained by using the left and right wheel speeds [85, 86]. Nowadays, most vehicles including MTAHVs contain ABS (Antilock Braking System) modules, which already tracks these signals. Thus, no additional hardware is required for this procedure. Eq. (4.16) defines the kinematic relationship between the yaw rate and wheel speeds.

$$\dot{\psi} = \frac{(\Omega_{fr} - \Omega_{fl})}{T_{wf} \cos \delta} R_{dyn} \quad (4.16)$$

where,  $\dot{\psi}$  denotes the yaw rate,  $\Omega_{fr}$  and  $\Omega_{fl}$  the rotational speeds of front right and front left wheels respectively,  $R_{dyn}$  the dynamic tire radius,  $T_{wf}$  the track width of the front axle, and  $\delta$  the steering angle. Even though Eq. (4.16), defines the yaw rate relationship using front wheel speeds, rear wheel speeds can be employed in a similar manner.

Observer 1 estimates the vehicle's yaw rates based on the available wheel speed measurements from the TruckSim model. However, the wheel speeds measurement are inherently noisy [85], thus it is beneficial to utilize a Kalman Filter for rejecting noise and generating accurate yaw rate estimates. Since the B-Train double is an interconnected system of three vehicle units (tractor and two semi-trailers); it is advisable that the Kalman Filter has a full knowledge of the vehicle geometry. Therefore, the linear 4DOF B-Train double model is employed to model the Kalman Filter. The controller requires individual yaw rates of each vehicle unit, i.e. tractor, first trailer and second trailer. Thus, for generating the kinetic estimate of yaw rates, wheel speed measurements of tractor's 1<sup>st</sup> axle, first trailer's 2<sup>nd</sup> axle and second trailer's 2<sup>nd</sup> axle are utilized. Hereon, the axles are denoted as Axle 1, Axle 5 and Axle 8 respectively. Furthermore, the tire sideslip angles influence the individual wheel speeds [85]. Thus, to compensate the variations in individual wheel speeds due to the tire side-slip angle, the tire side-slip angles for Axle 1, Axle 5 and Axle 8 are modelled using a first-order transient tire model inspired by [85]. Eq. (4.17) defines the tire sideslip angles for the axles.

$$\left\{ \begin{array}{l} \dot{\alpha}_1 = \frac{V_{y1} + S_1 \dot{\psi}_1 + |V_x| \alpha_1 - V_x \delta}{\sigma_1} \\ \dot{\alpha}_5 = \frac{V_{y2} - S_5 \dot{\psi}_2 + |V_x| \alpha_5}{\sigma_5} \\ \dot{\alpha}_8 = \frac{V_{y3} - S_8 \dot{\psi}_3 + |V_x| \alpha_8}{\sigma_8} \end{array} \right. \quad (4.17)$$

where,  $\alpha_i$  denotes the tire side-slip angle,  $V_{y_j}$  the lateral velocity,  $\dot{\psi}_j$  the yaw rate,  $V_x$  the vehicle forward speed, and  $\delta$  the steering angle,  $i$  denotes the axle, and  $j$  the vehicle unit.  $\sigma$  is the tire's relaxation length, and defines the tire's time-delay in attaining its steady-state value of lateral force [49].

The linear B-Train double model is modified by using the tire side-slip equations (see Eq. (4.17)). This modified model describes Observer 1, which utilizes wheel speeds and steering angle as inputs. Eq. (4.18) defines the measurement equations for Kalman Filter based Observer 1.

$$\left\{ \begin{array}{l} \dot{\psi}_1 = \frac{(\Omega_{1r} - \Omega_{2l})}{T_{1w} \cos \alpha_1} R_{dyn} \cos(\delta - \alpha_1) \\ \dot{\psi}_2 = \frac{(\Omega_{5r} - \Omega_{5l})}{T_{5w} \cos \alpha_5} R_{dyn} \\ \dot{\psi}_3 = \frac{(\Omega_{8r} - \Omega_{8l})}{T_{8w} \cos \alpha_8} R_{dyn} \end{array} \right. \quad (4.18)$$

where,  $\dot{\psi}_j$  denotes the yaw rate,  $\Omega_{ir}$  and  $\Omega_{il}$  the rotational speeds of right and left wheels respectively,  $T_{iw}$  the track width of the axle,  $i$  depicts the axle, and  $j$  the vehicle unit. Tracking performance of Observer 1 using TruckSim model under the SLC and DLC maneuvers is shown in Fig. 4.48 and 4.49 respectively. It is evident that the Kalman Filter based Observer 1 can predict the yaw rates of all vehicle units with reasonable accuracy.

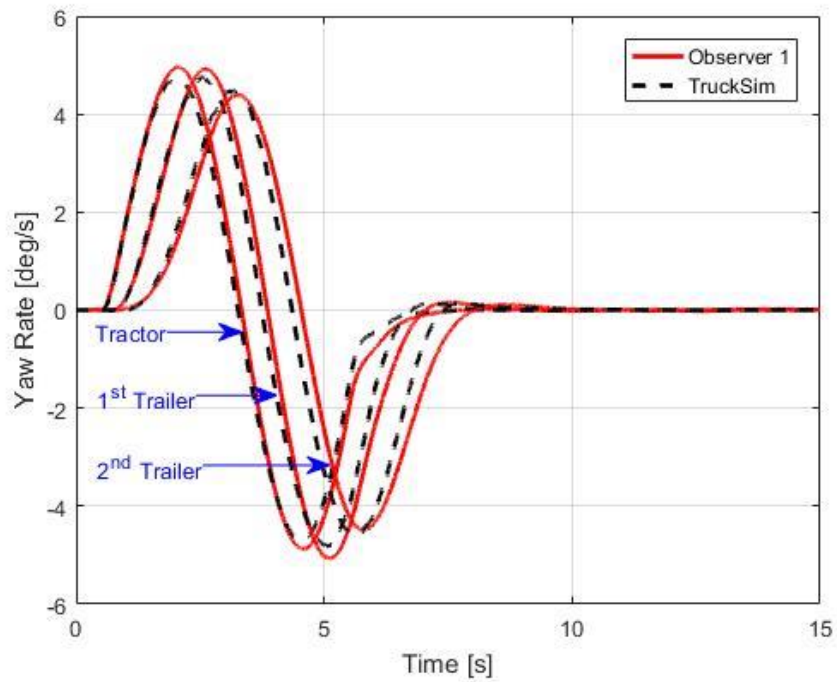


Figure 4.48 Time history of yaw rate estimates by Observer 1, and the actual TruckSim outputs under the SLC maneuver.

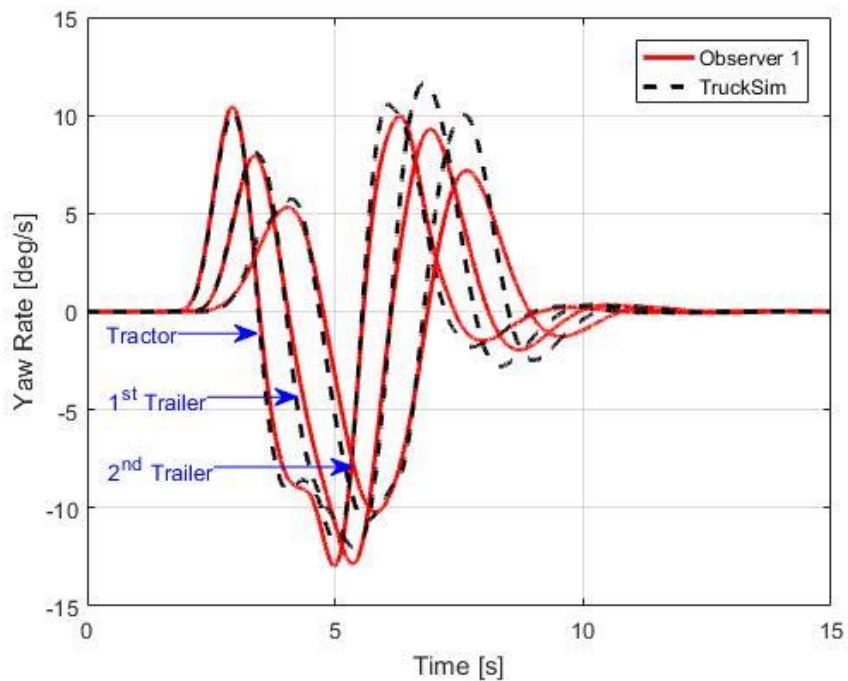


Figure 4.49 Time history of yaw rate estimates by Observer 1, and the actual TruckSim outputs under the DLC maneuver.

#### **4.5.3.2. Observer 2**

The ATS Hydraulic Actuation (AHA) system generates the desired ATS angles determined by the  $H^\infty$  controller. Since, hydraulic systems are complex in nature, faults or failures may occur. Therefore, it is necessary to implement fault diagnosis for the AHA system. Hydraulic systems are highly dependent on the system pressure, and loss of pressure can cause slow response or even total failure. In this research, only the faults that may arise due to pressure loss are considered.

Since the primary objective of the actuators is to generate the desired ATS angles, the only measured outputs in the AHA system are the actuators' positions. Besides, in this study the actuators are not a physical system. Thus, it is difficult to design an observer by using only one measurement. In addition, during simple maneuvers, such as SLC, it is noted that the generated ATS angles are very small (less than 2 degrees). Moreover, the AHA system employs a PID controller to ensure that the actuators generate the desired ATS angles specified by the controller. Thus, in the presence of actual malfunctions caused by slight pressure drop, such as minor oil leakage, loss of pump rotation speed etc., there will be unnoticeable fluctuations in the system's performance. As the actuator has to move a very limited distance, the faults may go undetected.

Considering the aforementioned concerns, the observer for the AHA system cannot be based exclusively on the positions measurements. Therefore, Observer 2 performs fault detection and diagnosis by estimating the force output of the system. Since, the force output is very sensitive to minor fluctuations in pressure, this procedure should reliably detect any impending faults in the AHA system.

The AHA system model defined in Section 3.4 assumes that a constant pressure supply of 20 MPa is available. However, in real-life, a hydraulic pump generates the pressure. Moreover, to simulate faults in the AHA system, the pressure of the system needs to vary. Therefore, during simulations the supply pressure ( $P_s$ ) is considered as a function of pump rotation speed defined in Eq. (4.19) [85].

$$V_p = \frac{2K_c P_s}{\eta_{pv} \omega} \quad (4.19)$$

where,  $V_p$  defines the pump's displacement,  $K_c$  the pressure flow coefficient,  $P_s$  supply pressure of the system,  $\eta_{pv}$  pump's volumetric efficiency, and  $\omega$  the pump rotation speed. The force output of the actuation system is estimated using Eq. 4.20, which is a modified version of the equation(s) published in [86].

$$\begin{cases} \frac{V_t}{4\beta_e} \Delta \dot{P} + K_c \Delta P = K_q x - A_A \dot{y} \\ F = \Delta P A_A \end{cases} \quad (4.20)$$

where,  $V_t$  is the trapped volume of oil in the cylinder,  $\beta_e$  the fluid bulk modulus, and  $\Delta P$  the pressure difference between the two sides of the piston.  $x$  and  $\dot{y}$  are the spool displacement and the actuator's velocity respectively, and also the inputs to the system.  $F$  denotes the system's force output, and  $A_A$  the cross-sectional area of the piston. The remaining constants are already defined in the previous sections.

The system defined by Eq. (4.20) requires two inputs, the spool displacement and actuator's velocity. Spool displacement is the input to the AHA system and already known (see Eq. (3.27)). However, the AHA system only measures position. Hence, the actuator's velocity is unknown.

To estimate the actuator's velocity a discrete-time Kalman Filter is employed (see Eq. (4.21)). In addition to estimating the velocity, the Kalman Filter provides a redundant position measurement to maintain functionality if the actuator's position sensor malfunctions.

$$\frac{\hat{y}[n+1] - \hat{y}[n]}{T_s} = \frac{\hat{y}[n+1] + \hat{y}[n]}{2} \quad (4.21)$$

where,  $\hat{y}$  is the estimated position,  $\hat{v}$  the estimated velocity,  $n$  the discrete time index, and  $T_s$  the time-step size.

Contrary to the system model defined in Section 3.3, the supply pressure in the modified system defined by Eq. (4.20) is variable and defined by the pump rotation speed. Since the fundamental constants of the modified system such as pressure sensitivity, flow-coefficient, bulk modulus etc., are dependent on the supply pressure. The system is expected to show notable variations in the force output in cases of fault occurrences. Thus, Observer 2 employs the modified-AHA system for FDD purposes.

However, for fault detection and diagnoses, a system is required, which estimates the force output of the nominal system. Hence, a simple first-order system is modeled to mimic to the force output of the modified-AHA system.

$$T_d \dot{F} + F = K_f i \quad (4.22)$$

where,  $T_d$  depicts the time constant of the system,  $F$  the force output,  $K_f$  the system gain, and  $i$  the input current.

FDD is implemented by assessing the performance variation in the nominal system, and the modified-AHA system defined by Eq. (4.20) and (4.22) respectively. The nominal system estimates the force output using the known input. Whereas, the modified AHA system estimates the force output by utilizing the solenoid's current input and actuator's velocity prediction by the discrete-time Kalman Filter.

To establish the presence of faults, the maximum variation in force output between the nominal and modified-AHA system is calculated. Specifically, a residual signal is generated, which signifies the presence of faults. Moreover, the described procedure is implemented for all the active trailer axles. Thus, detection and diagnosis of individual ATS axles is possible.

Fig. 4.50 and 4.51 illustrate the tracking performance for Observer 2 under the SLC and DLC maneuvers respectively. Observer 2 signifies the nominal system and the actual force output signifies the modified-AHA system. Both figures indicate excellent agreement between Observer 2's estimation and the actual force output. The simple first-order system can accurately track the system's force output during fault-free conditions.

Fig. 4.52 to 4.55 illustrate the tracking performance of the discrete-time Kalman Filter. The Kalman Filter aids the modified-AHA system to estimate the force output. Fig. 4.52 and 4.53 show the velocity tracking performance of the Kalman Filter. Moreover, as previously mentioned that the Kalman Filter also acts as a redundant position sensor. The position tracking performance is illustrated in Fig. 4.54 and 4.55. All results indicate good agreement.

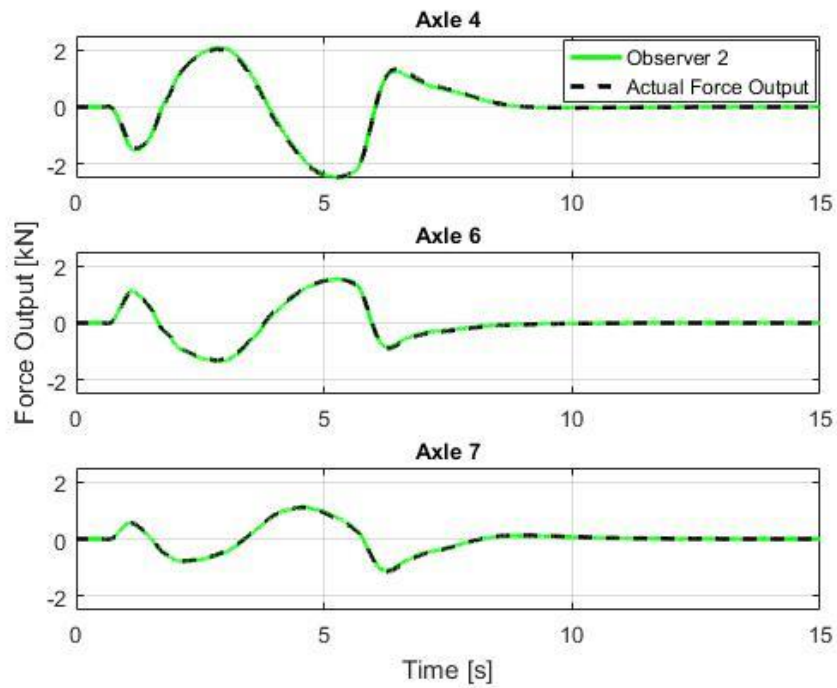


Figure 4.50 Time history of force output estimates by Observer 2, and the actual force outputs under the SLC maneuver.

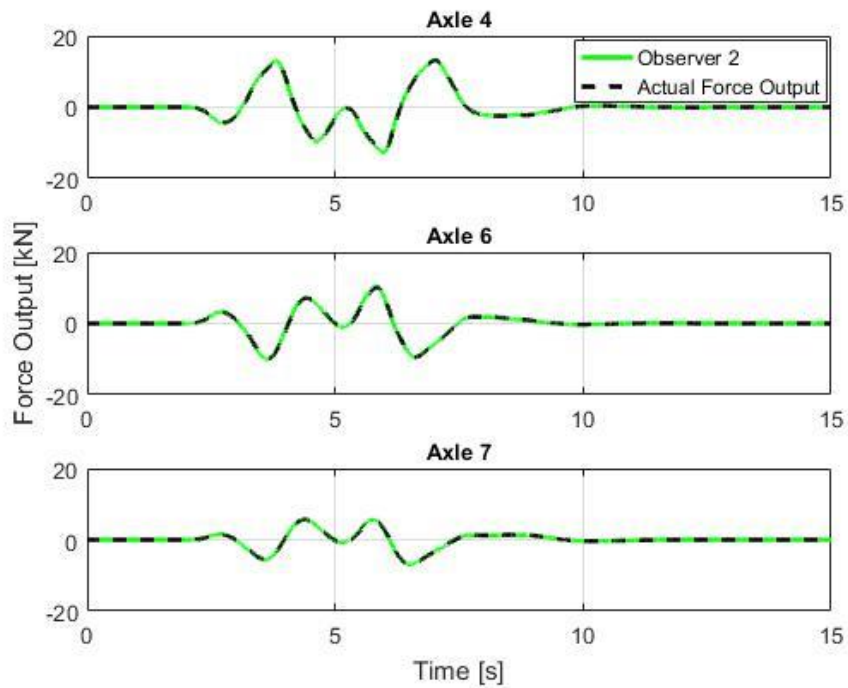


Figure 4.51 Time history of force output estimates by Observer 2, and the actual force outputs under the DLC maneuver.

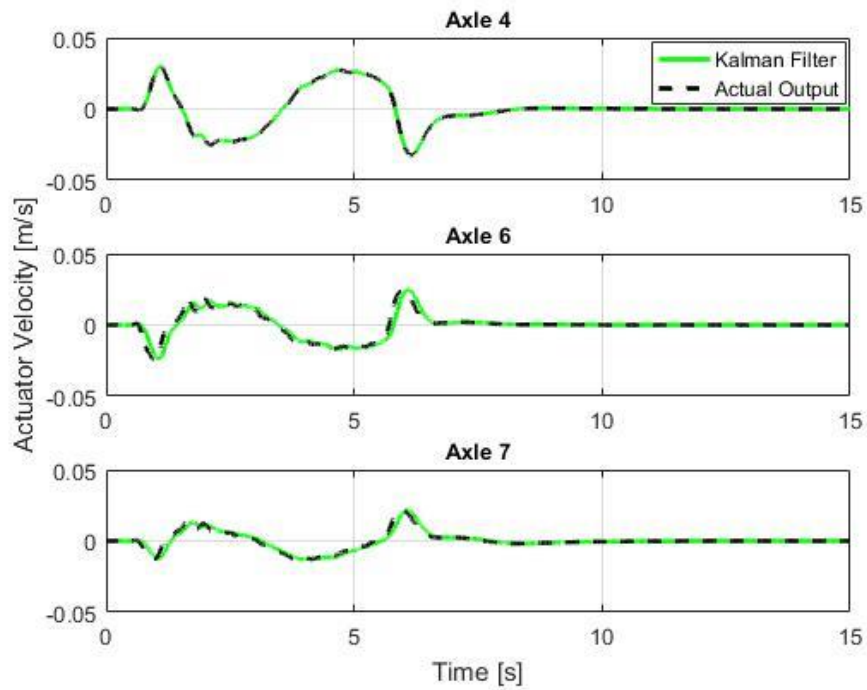


Figure 4.52 Time history of actuator velocity estimates by the Kalman Filter (Observer 2), and the actual velocity outputs under the SLC maneuver.

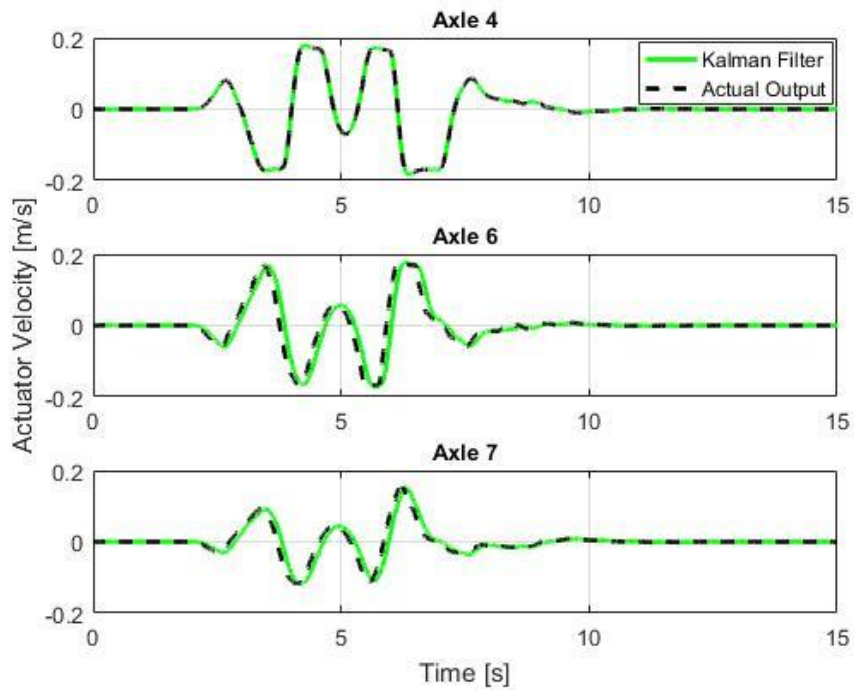


Figure 4.53 Time history of actuator velocity estimates by the Kalman Filter (Observer 2), and the actual velocity outputs under the DLC maneuver.

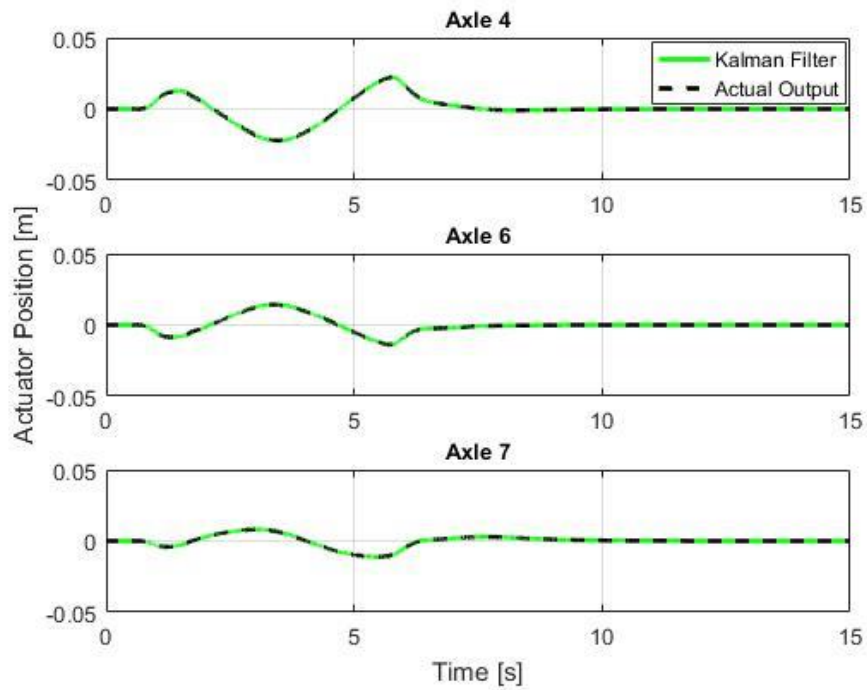


Figure 4.54 Time history of actuator position estimates by the Kalman Filter (Observer 2), and the actual position outputs under the SLC maneuver.

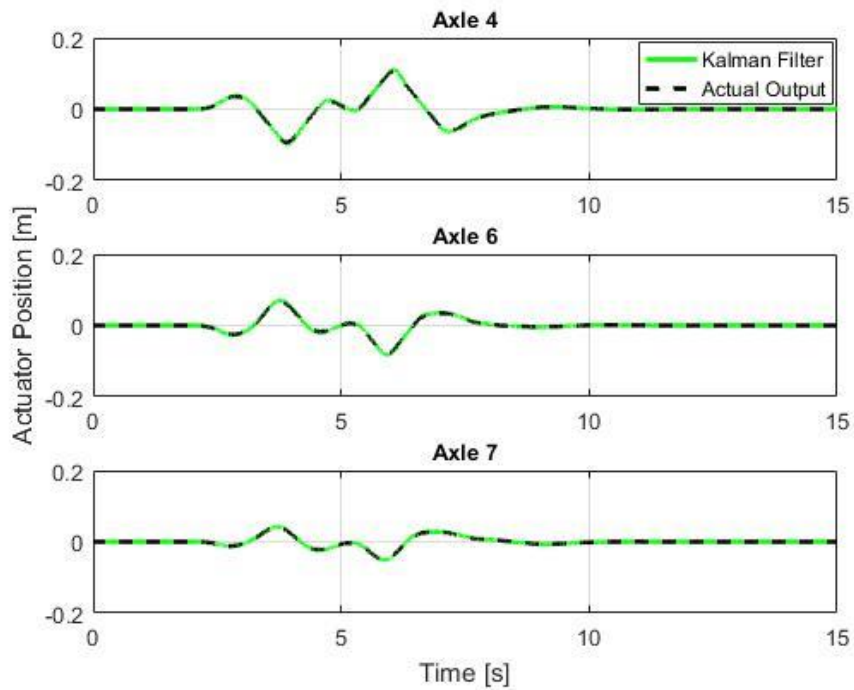


Figure 4.55 Time history of actuator position estimates by the Kalman Filter (Observer 2), and the actual position outputs under the DLC maneuver.

#### 4.5.3.3. Observer 3

A controller such as the  $H^\infty$  controller is very complex. Hence, it is not viable to compute the controller calculations separately. This contributes towards increased computational efforts. Conversely, a simple model allows monitoring and provides a reasonable indication of the desired system performance. Observer 3 observes the ATS controller and the AHA system simultaneously. Eq. (4.23) defines the observer based on a first-order transient model approximation.

$$\begin{cases} T_{sys}\dot{\delta}_4 + \delta_4 = K_{\delta_4 1}Y_{e1} + K_{\delta_4 2}Y_{e2} \\ T_{sys}\dot{\delta}_6 + \delta_6 = K_{\delta_6 1}Y_{e1} + K_{\delta_6 2}Y_{e2} \\ T_{sys}\dot{\delta}_7 + \delta_7 = K_{\delta_7 1}Y_{e1} + K_{\delta_7 2}Y_{e2} + K_{\delta_7 3}Y_{e3} \end{cases} \quad (4.23)$$

where,  $T_{sys}$  denotes the time constant of the system,  $\delta_i$  the ATS angles of the respective axle,  $K_{\delta_{ij}}$  the respective gain(s),  $Y_{ej}$  the error between the desired and actual yaw rate of the respective unit,  $i$  depicts the axle, and  $j$  the vehicle unit.

The input to the observer is the error between desired and actual yaw rate whereas the outputs are the desired ATS angles. A Kalman Filter is used to construct this observer, where the noisy position measurements from the AHA system are fed into the observer to obtain correct readings. Logical combination of Observer 2 and Observer 3 can detect and isolate faults within the controller or the actuation system. Fig. 4.56 and 4.57 illustrate the tracking performance of Observer 3 under SLC and DLC maneuvers simultaneously. Although, deviations are evident specifically for Axle 7's prediction, Observer 3 provides a reasonable estimation of the desired ATS angles.

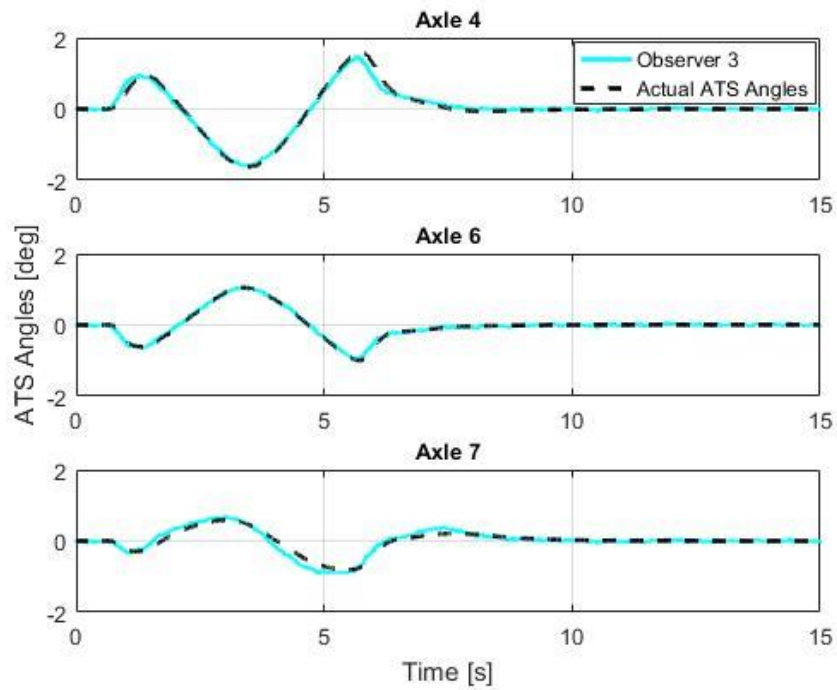


Figure 4.56 Time history of ATS angle estimates by Observer 3, and the actual ATS angles under the SLC maneuver.

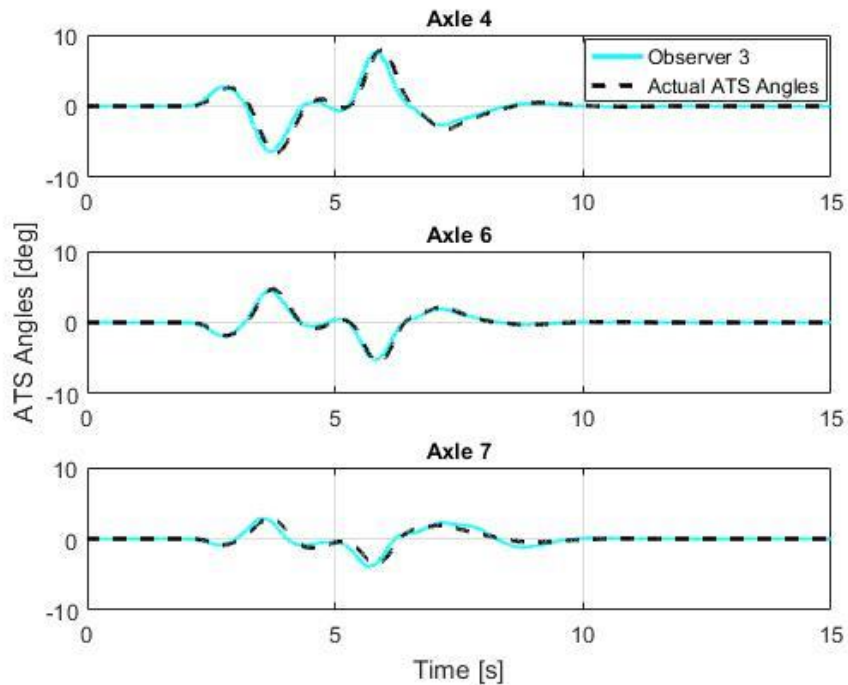


Figure 4.57 Time history of ATS angle estimates by Observer 3, and the actual ATS angles under the DLC maneuver.

## **4.5.4. Fault Tolerance**

### **4.5.4.1. Residual Generation**

In the previous sub-section, Observer 1, Observer 2 and Observer 3 for FTC-ATS scheme were presented, and their capability to predict fault occurrence was established. However, to enhance computational efficiency, the observers are based on simple mathematical models, and minor differences exist between the observer outputs and the systems they observe. These differences between the observers and the systems may lead to false fault detections by the FTC system. Therefore, to accurately predict fault occurrence, the residual generation technique is employed, where the difference between the observer and the system output is calculated, and compared to the predefined threshold residual limits to assess fault occurrence. In this study, for all observers, the term “residual” indicates the maximum error achieved between the observer and the actual system.

Fig. 4.58 to 4.63 illustrate the residual signal and the residual limits for the observers under the SLC and DLC maneuvers. The figures display the residual signals and the residual limits during nominal operation. It is evident that during nominal operation, the residual signals remain below their respective limits for Observer 1, Observer 2 and Observer 3. However, it is observed that the residual signals for all observers indicate comparatively higher peak values under the DLC maneuver.

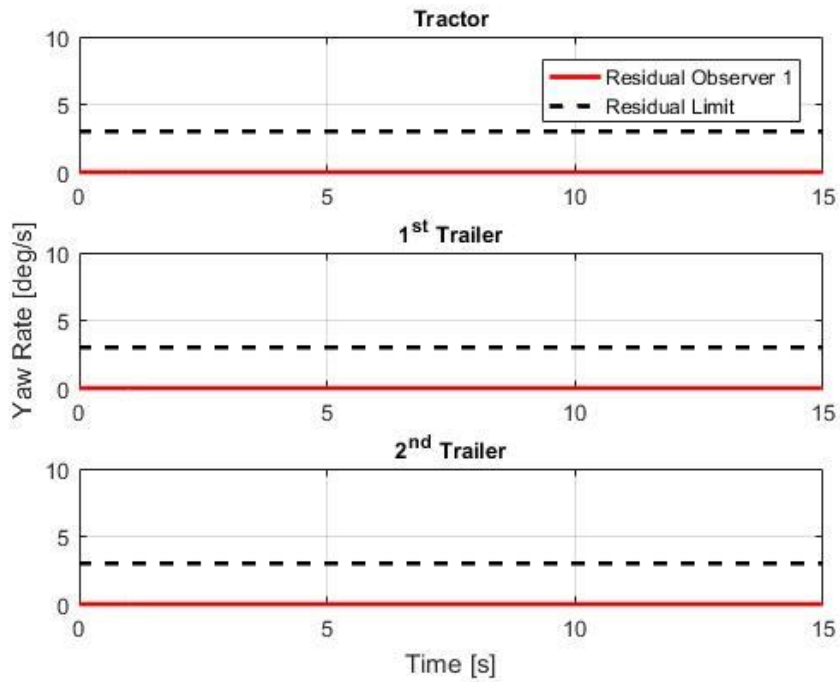


Figure 4.58 Time history of Observer 1's residual signals, and the threshold limits under the SLC maneuver.

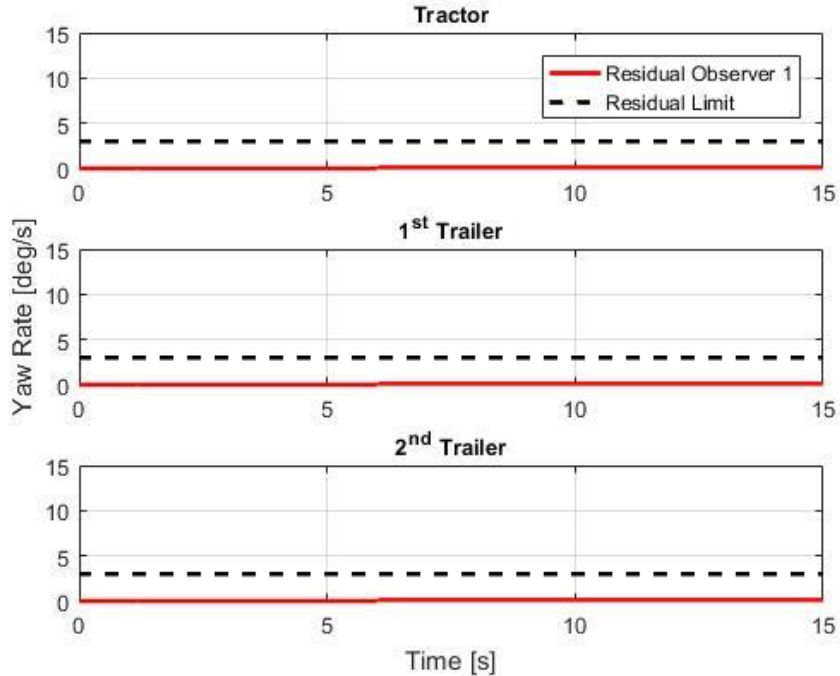


Figure 4.59 Time history of Observer 1's residual signals, and the threshold limits under the DLC maneuver.

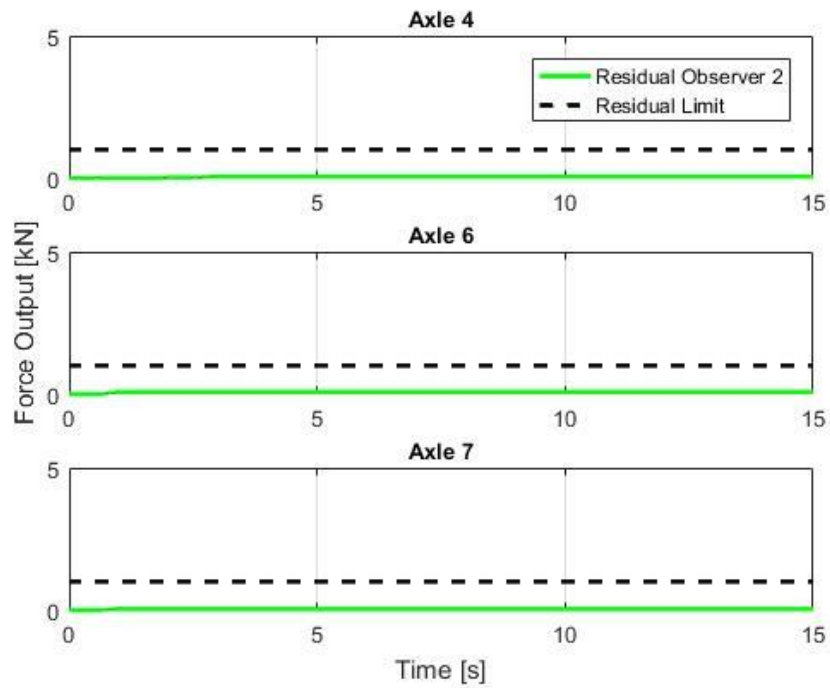


Figure 4.60 Time history of Observer 2's residual signals, and the threshold limits under the SLC maneuver.

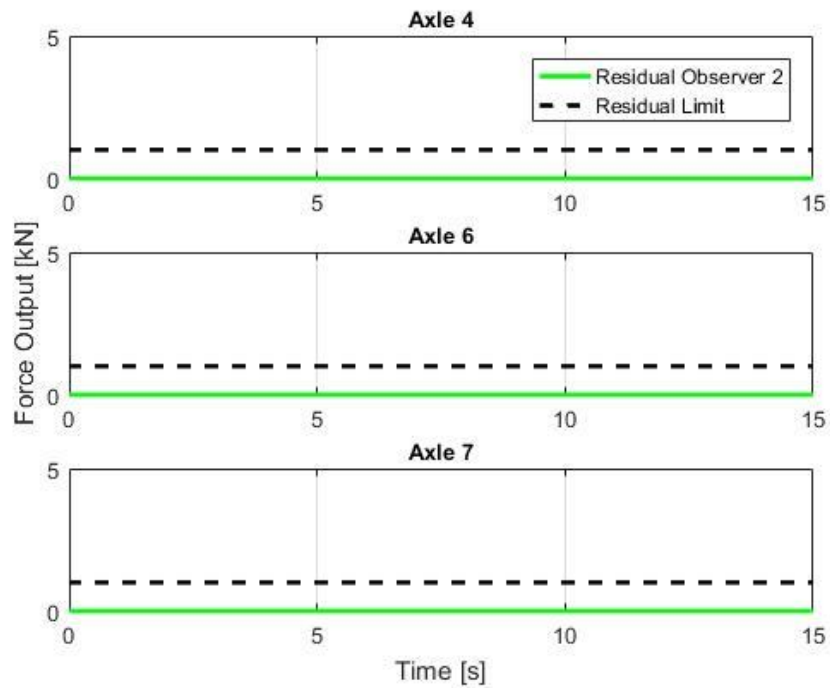


Figure 4.61 Time history of Observer 2's residual signals, and the threshold limits under the DLC maneuver.

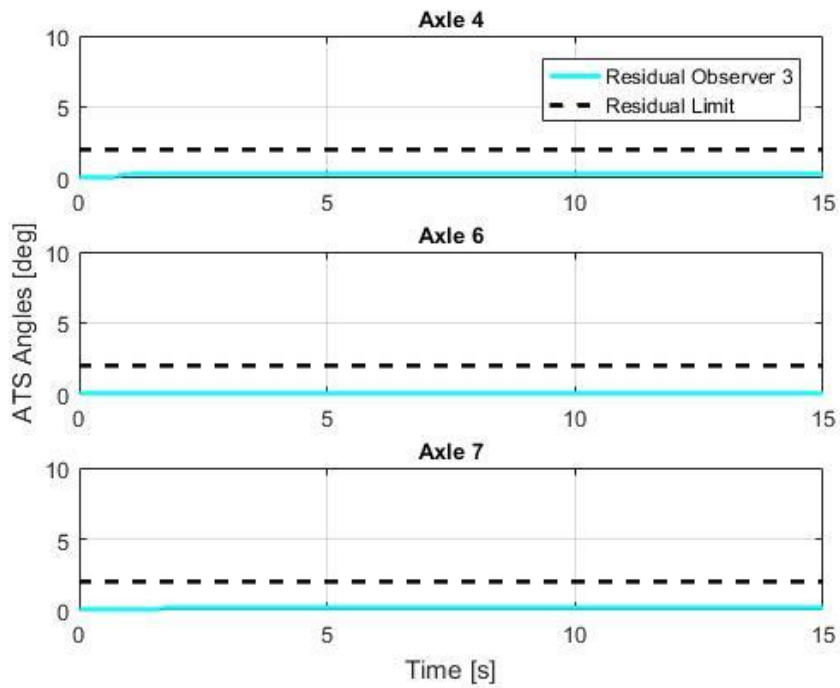


Figure 4.62 Time history of Observer 3's residual signals, and the threshold limits under the SLC maneuver.

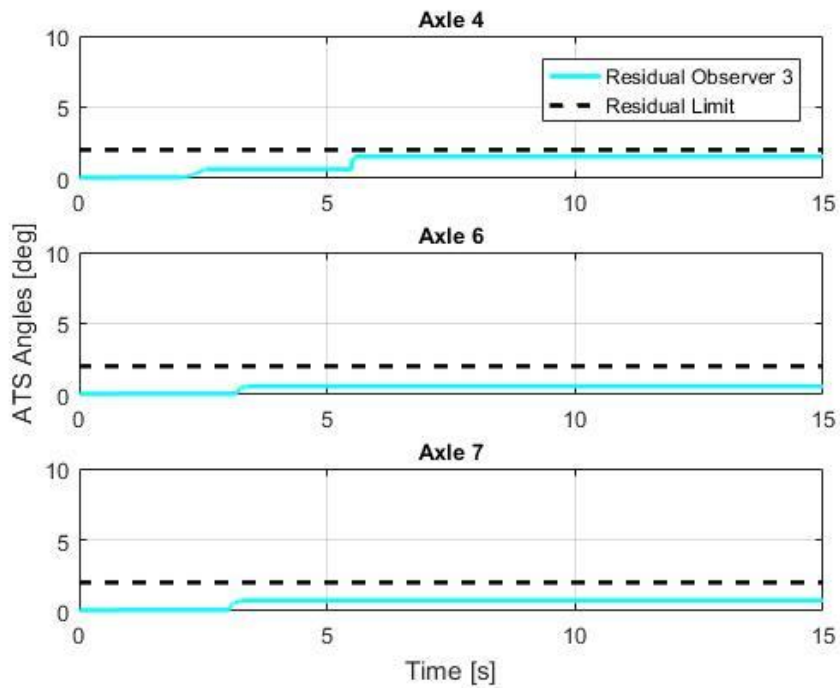


Figure 4.63 Time history of Observer 3's residual signals, and the threshold limits under the DLC maneuver.

#### **4.5.4.2. Fail-Operational and Fail-Safe Modes**

The previous sections have demonstrated the Fault Detection and Diagnosis methods for the FTC-ATS scheme. However, to complete a fault tolerant system, fail-operational and fail-safe modes are defined, which dictate the system to return to a safe state in the case of failures. Fail-operational and fail-safe modes are applied sequentially. Fail-operational mode tolerates one failure, and allows the active system to remain operational [26]. However, in the case of multiple failures, the fail-safe mode is activated, where the active system is brought to a passive state using external power [26].

The ATS systems are employed to enhance the vehicle's dynamic performance. However, in the case of faults, these systems may deteriorate the vehicle's performance. Thus, in such situations where the ATS-assisted vehicle's performance is worse than the baseline vehicle, it is logical to lock the active axles. In this research the fault tolerant modes, specifically the FS mode, is activated when the residual signal between the baseline vehicle and ATS-assisted vehicle exceeds the threshold limit. The residual signal is a comparison of the peak lateral acceleration achieved by the B-Train double's second trailer. Since in MTAHVs the rearmost trailer exhibits the worst stability, a further increase in its peak lateral acceleration induced by a faulty ATS system may result in rollover or other unsafe situations. The lateral acceleration of the baseline vehicle's second trailer is generated using the linear B-Train double model. If the residual exceeds the threshold limit, the system is instructed to lock all active axles. Table 4.2 displays the fail-operational and fail-safe modes.

Table 4.2 FDD and FTC Modes.

Faults	Fault Detection by			FTC Decision
	Observer 1	Observer 2	Observer 3	
Yaw Rate Sensor Failure	Y	N	Y*	Switch to redundant Component (FO)
Axle 4 Malfunction	N	Y	Y*	Lock all Axles (FS)
Axle 6 Malfunction	N	Y	Y*	Lock only Axle 6 (FO)
Axle 7 Malfunction	N	Y	Y*	Lock only Axle 7 (FO)
Controller Failure	N	N	Y	Lock all Axles (FS)

In Table 4.2, FO signifies fail-operational, and FS denotes fail-safe. Asterisk (\*) indicates that the observer may or may not be able to detect the respective fault. The fault tolerant modes are defined by considering the simulation results presented in the next sub-section. In addition to the aforementioned faults, the FTC system will lock all active axles (FS mode), if the residual signal between the baseline vehicle and ATS-assisted vehicle exceeds the threshold limit.

#### 4.5.4.3. Simulation Setup

This sub-section presents the simulation setup employed for the FTC-ATS scheme. As previously mentioned, TruckSim and Simulink software packages are combined to generate the FTC system. Fig. 4.64 depicts the system diagram built in Simulink. The system shown is a basic version of the actual Simulink diagram simplified to present the salient components. As illustrated in Fig. 4.64, measurements, such as wheel speeds, yaw rates, and steering input are obtained from TruckSim. The controller computes the desired ATS angles and sends this information to the actuation system. Here, the AHA system generates the desired ATS angles and sends them to the subsequent block, where the individual angles of left and right wheel(s) are computed using a lookup table. The simulations are performed under the SLC and DLC maneuvers, where the SLC is an open-loop maneuver, and the DLC is a closed-loop maneuver with TruckSim's driver model.

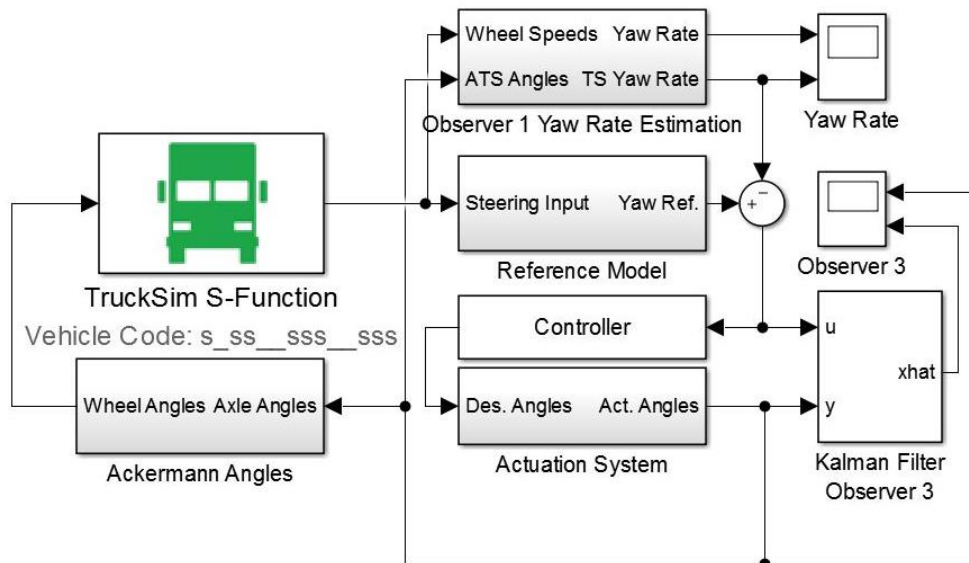


Figure 4.64 Simplified Simulink diagram signifying the FTC system built using TruckSim and Simulink software.

## **4.5.5. Simulation Results**

### **4.5.5.1. Sensor Failure**

This sub-section presents the simulation results for a simulated yaw-rate sensor failure under the SLC and DLC maneuvers. Moreover, the impact on the vehicle's dynamic performance during the sensor failure is evaluated. Furthermore, the efficacy of the yaw rate estimation by Observer 1 is assessed by employing its estimation as an input to the  $H^\infty$  ATS controller.

To simulate the failure, the yaw rate sensor is switched-off. Fig. 4.65 and 4.66 display the residual signals of the respective vehicle units under the SLC and DLC maneuver respectively. Since the yaw rate sensor has failed, the residual signal surpasses the limits, clearly indicating fault occurrence.

Fig. 4.67 to 4.70 illustrates the dynamic performance of vehicle under both the maneuvers. It is apparent that the system performance degrades considerably due to sensor failure. Moreover, the lateral acceleration and yaw rate responses are worse than the baseline vehicle without ATS system. It is logical to assume that in the absence of a FTC system, the vehicle will experience dangerous motion modes, such as rollover, jack-knifing etc. However, the system can regain its controlled nature by utilizing the yaw rate estimation from Observer 1. Fig. 4.71 to 4.74 show the vehicle's dynamic performance achieved by employing Observer 1's yaw rate estimation as the input to the controller. Results strongly suggest that by utilizing Observer 1's yaw rate estimation, vehicle's desired closed-loop performance can be ensured even during sensor failure.

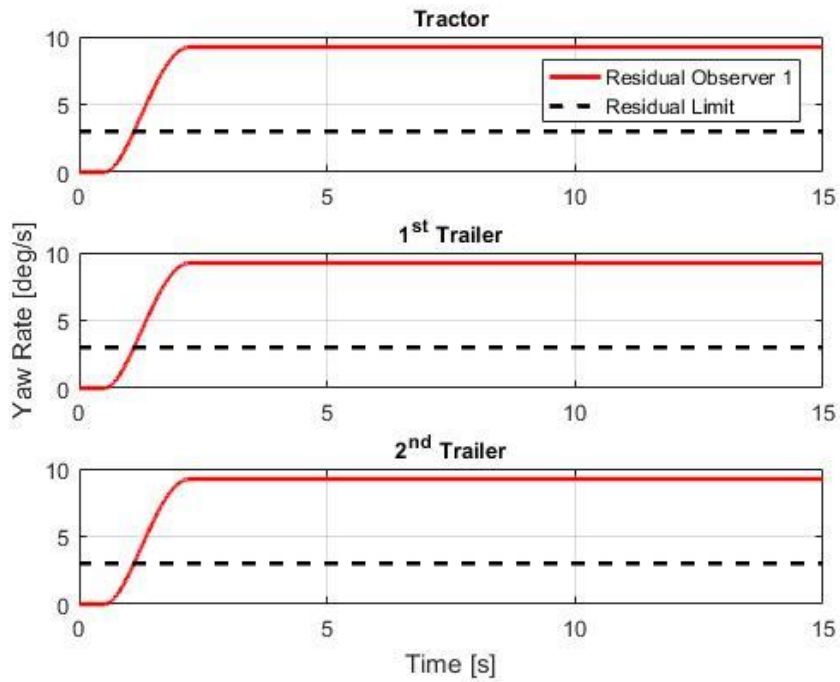


Figure 4.65 Time history of Observer 1's residual signals, and the threshold limits under the SLC maneuver for the yaw-rate sensor failure.

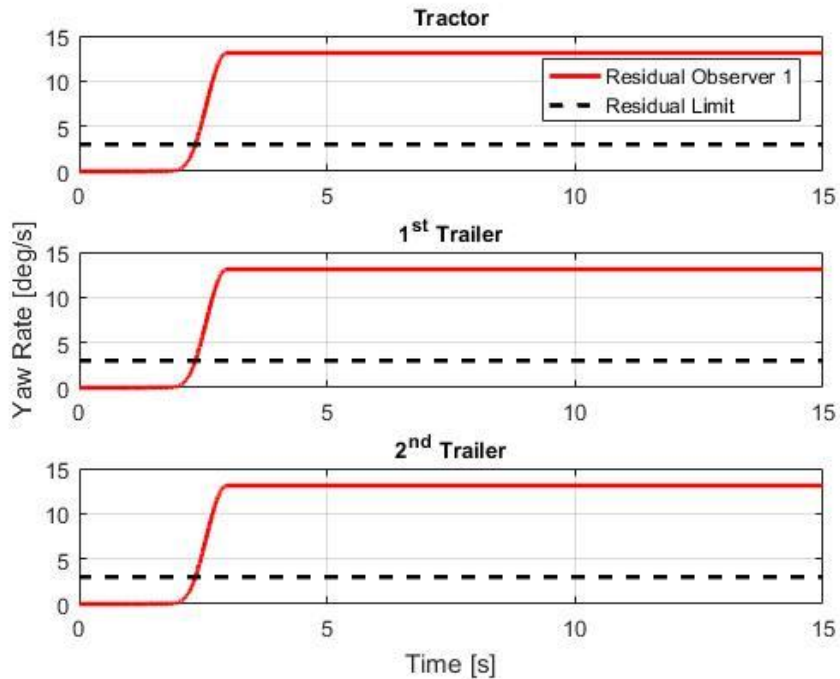


Figure 4.66 Time history of Observer 1's residual signals, and the threshold limits under the DLC maneuver for the yaw-rate sensor failure.

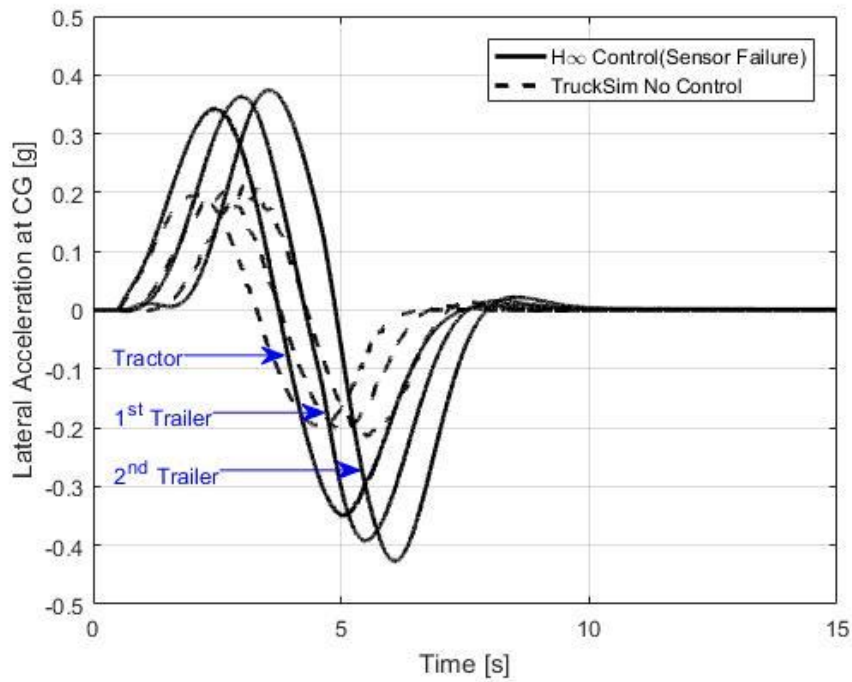


Figure 4.67 Time history of lateral accelerations for the  $H^\infty$  controlled vehicle and the baseline TruckSim vehicle under the SLC maneuver for the yaw-rate sensor failure.

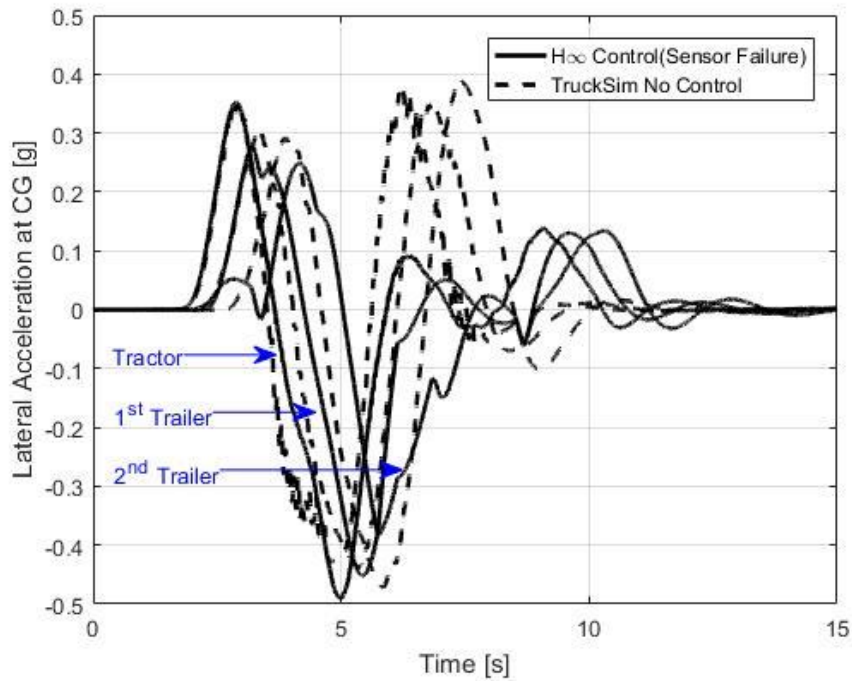


Figure 4.68 Time history of lateral accelerations for the  $H^\infty$  controlled vehicle and the baseline TruckSim vehicle under the DLC maneuver for the yaw-rate sensor failure.

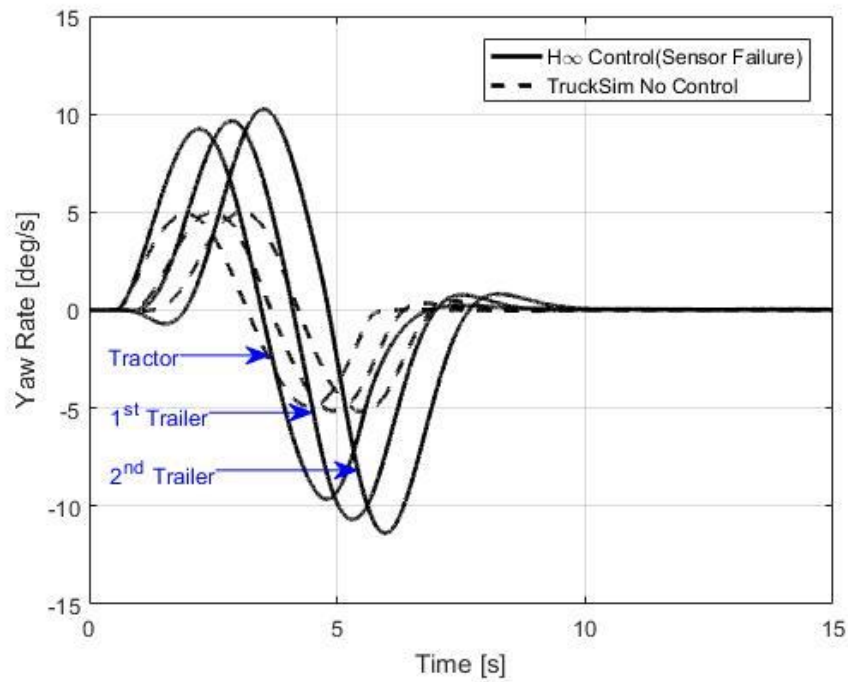


Figure 4.69 Time history of yaw rates for the  $H^\infty$  controlled vehicle and the baseline TruckSim vehicle under the SLC maneuver for the yaw-rate sensor failure.

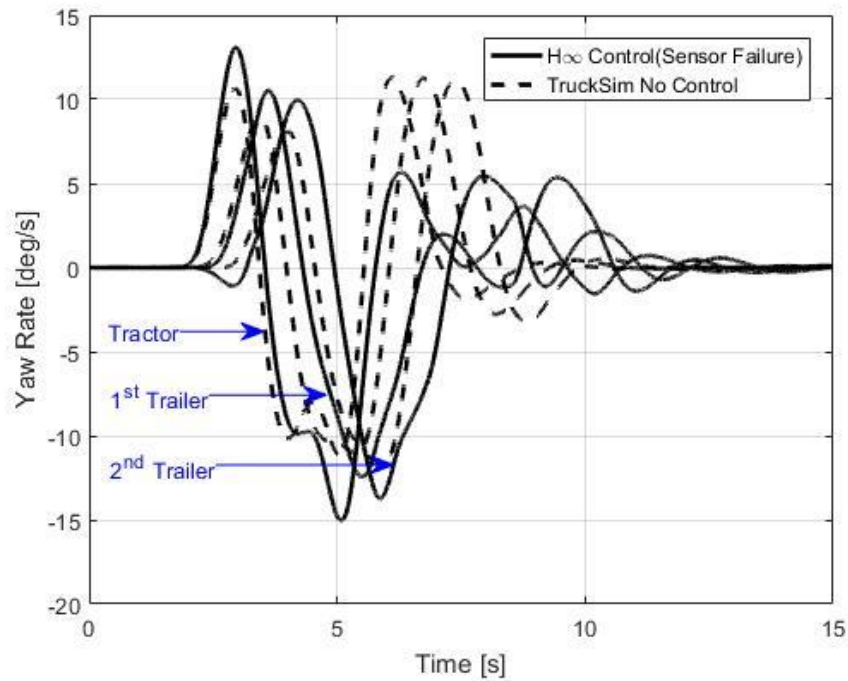


Figure 4.70 Time history of yaw rates for the  $H^\infty$  controlled vehicle and the baseline TruckSim vehicle under the DLC maneuver for the yaw-rate sensor failure.

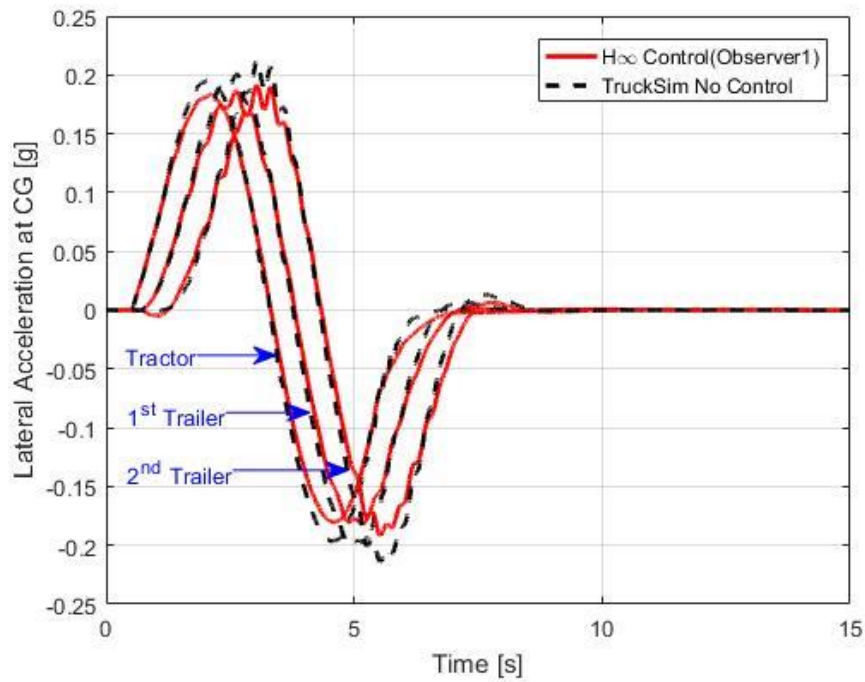


Figure 4.71 Time history of lateral accelerations for the  $H^\infty$  controlled (Observer 1) vehicle and the baseline TruckSim vehicle under the SLC maneuver for the yaw-rate sensor failure.

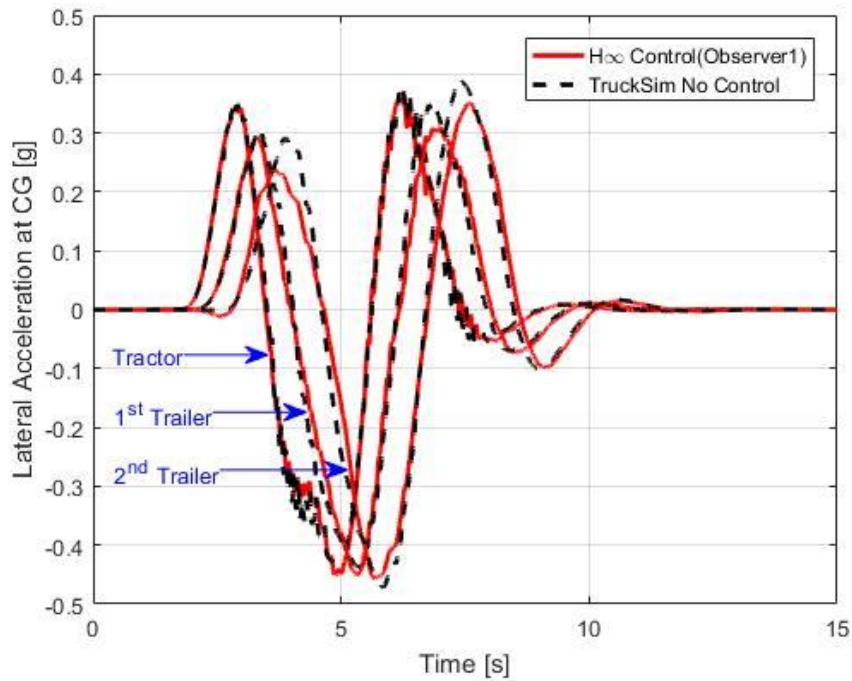


Figure 4.72 Time history of lateral accelerations for the  $H^\infty$  controlled (Observer 1) vehicle and the baseline TruckSim vehicle under the DLC maneuver for the yaw-rate sensor failure.

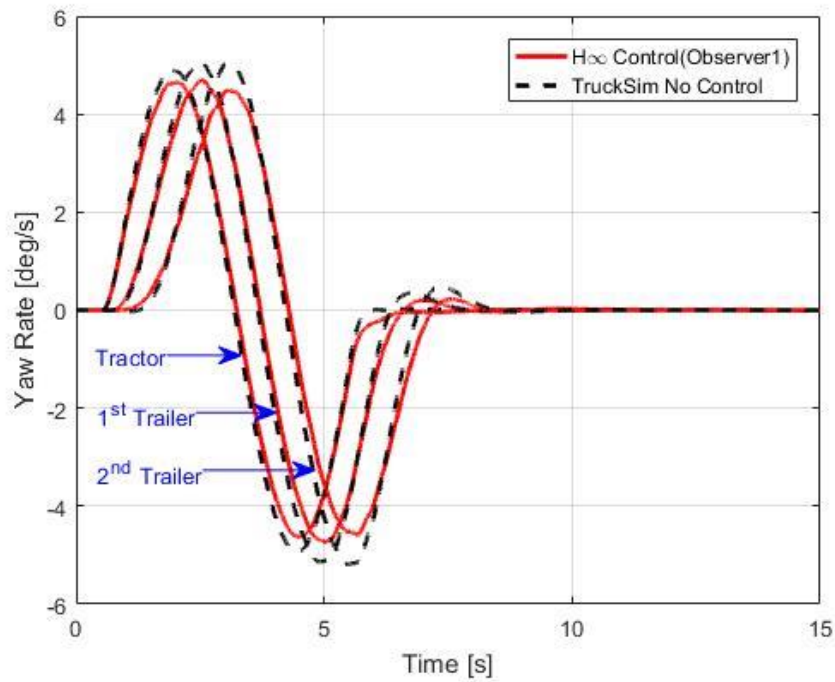


Figure 4.73 Time history of yaw rates for the  $H^\infty$  controlled (Observer 1) vehicle and the baseline TruckSim vehicle under the SLC maneuver for the yaw-rate sensor failure.

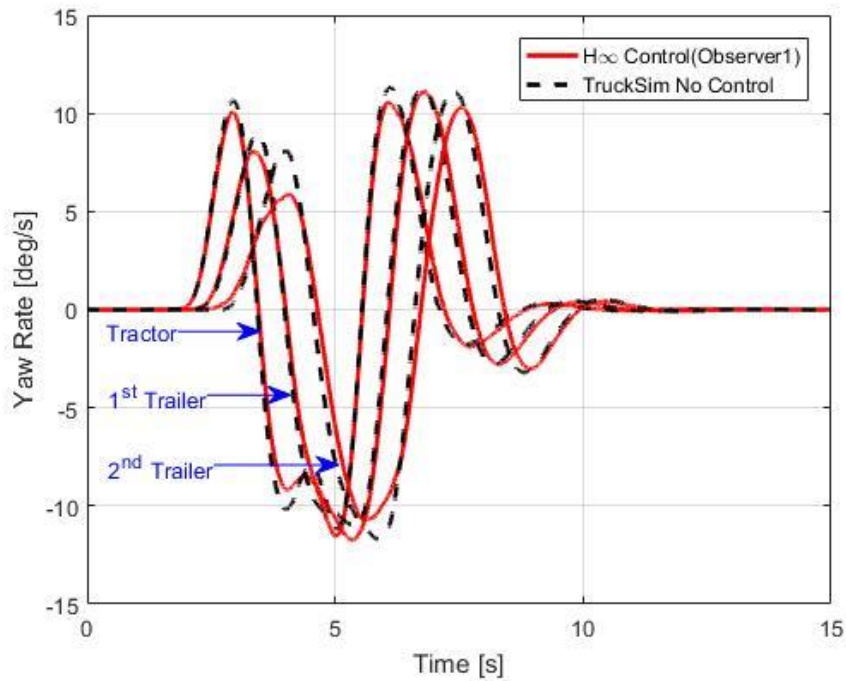


Figure 4.74 Time history of yaw rates for the  $H^\infty$  controlled (Observer 1) vehicle and the baseline TruckSim vehicle under the DLC maneuver for the yaw-rate sensor failure.

#### 4.5.5.2. Actuator Malfunction(s)

This sub-section presents the simulation results for actuator malfunctions under the SLC and DLC maneuvers. Since it is unlikely that actuators will fail simultaneously, in the simulations each actuator is “failed” individually. Unlike the sensor-failure fault scenario, here the actuators do not fail completely. To simulate actuator malfunction, the system pressure in the actuator model is reduced by reducing the motor speed as defined in Eq. (4.19).

Fig. 4.75 to 4.78 illustrate the simulation results for actuator failure in Axle 4. The figures depict the estimation of Observer 2 and Observer 3, and their residual signals. It is apparent that under both SLC and DLC maneuvers, Observer 2 is able to predict the fault occurrence in the actuator. Fig. 4.75 and 4.76 show notable deviation between the system, and the residual signals are beyond the threshold limits. Conversely, Observer 3 can only predict the fault occurrence under the DLC maneuver (see Fig. 4.77 and 4.78).

Similar results are obtained for actuator malfunctions in Axle 6 and Axle 7 under the SLC and DLC maneuvers. Fig. 4.79 to 4.86 show the simulation results. Predictably, Observer 2 can detect fault-occurrence under both the maneuvers, whereas Observer 3 is suitable only during the DLC maneuver.

Since the generated ATS angles under the SLC maneuver are very small, there is negligible difference between the actuator output and Observer 3’s estimate. However, during the DLC maneuver, the ATS angles are large, and notable difference is observed. The results corroborate the presumption made in Section 4.5.3.2 that force estimation is necessary to predict actuator faults.

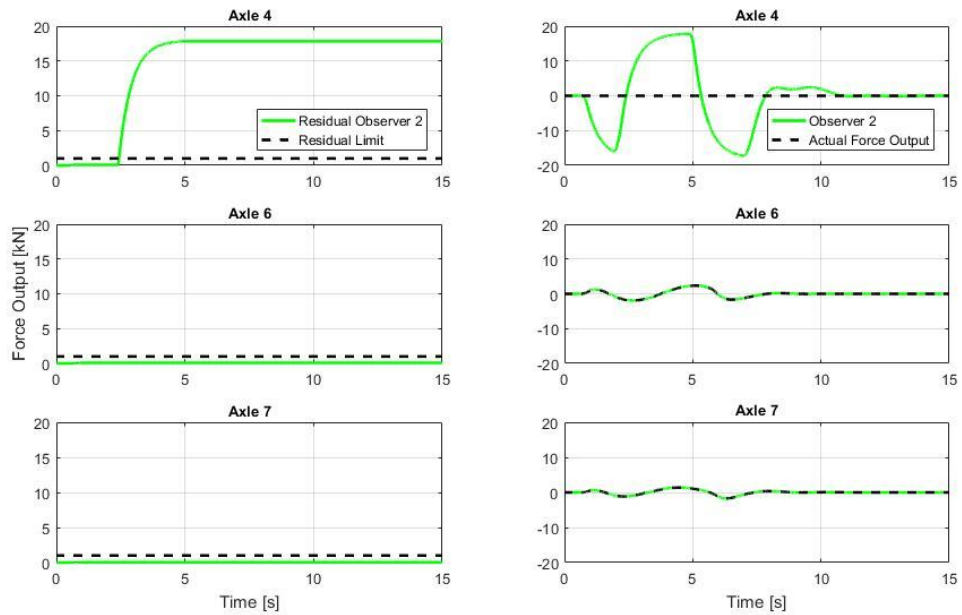


Figure 4.75 Time history of Observer 2's residual signals, the threshold limits, force output estimates, and the actual force outputs under the SLC maneuver for Axle 4's actuator malfunction.

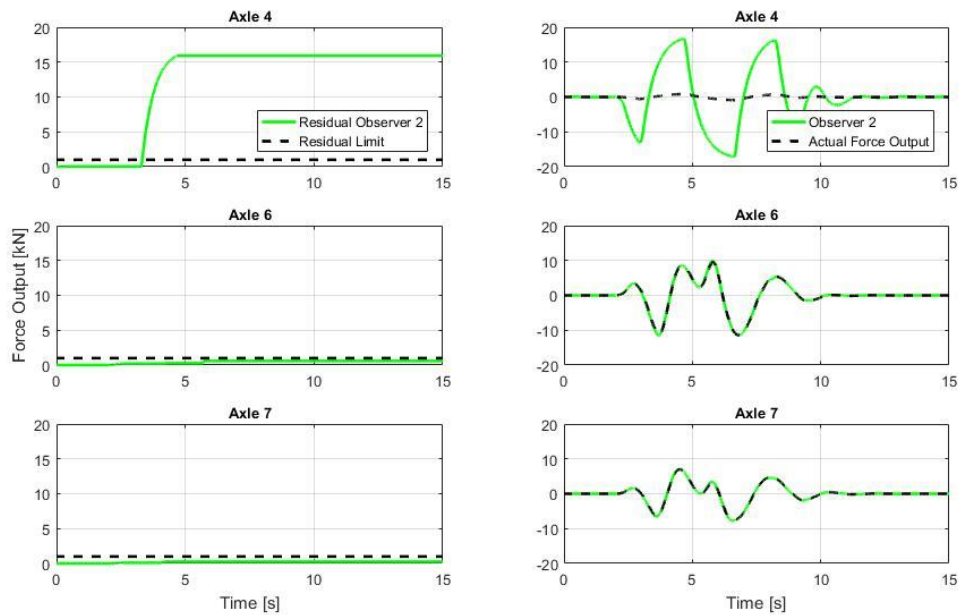


Figure 4.76 Time history of Observer 2's residual signals, the threshold limits, force output estimates, and the actual force outputs under the DLC maneuver for Axle 4's actuator malfunction.

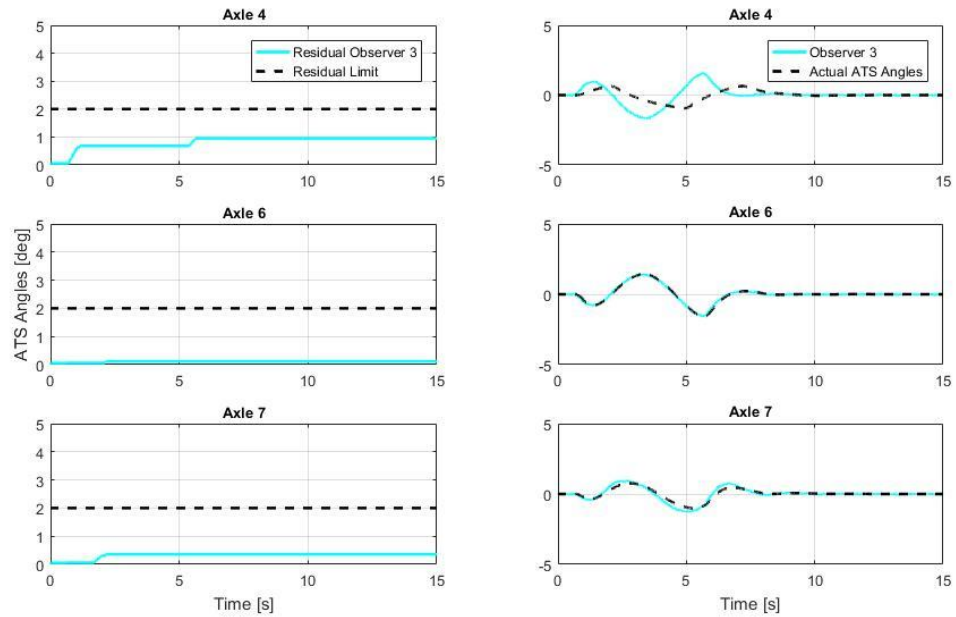


Figure 4.77 Time history of Observer 3's residual signals, the threshold limits, ATS angle estimates, and the actual ATS angles under the SLC maneuver for Axle 4's actuator malfunction.

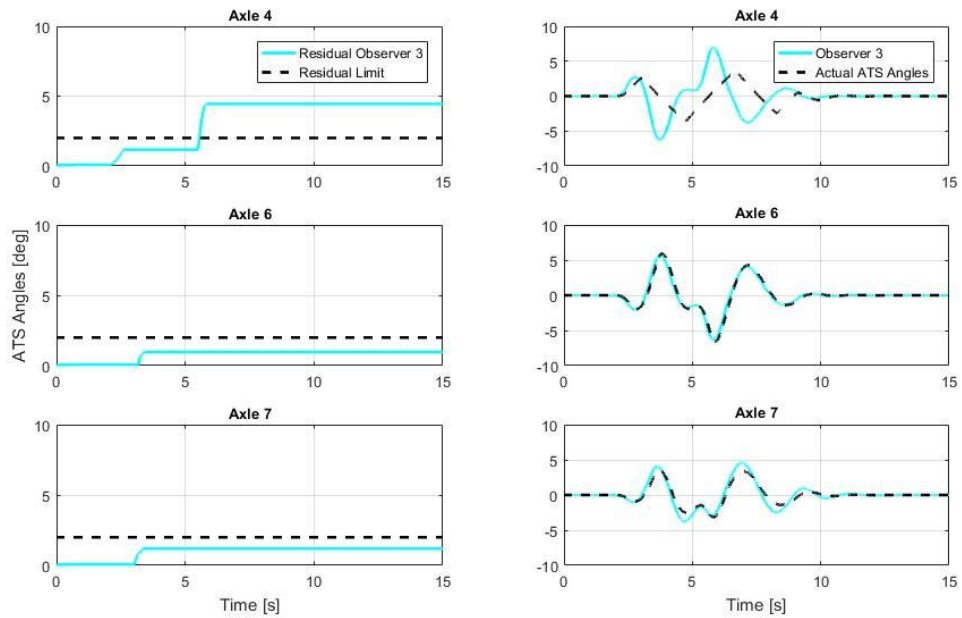


Figure 4.78 Time history of Observer 3's residual signals, the threshold limits, ATS angle estimates, and the actual ATS angles under the DLC maneuver for Axle 4's actuator malfunction.

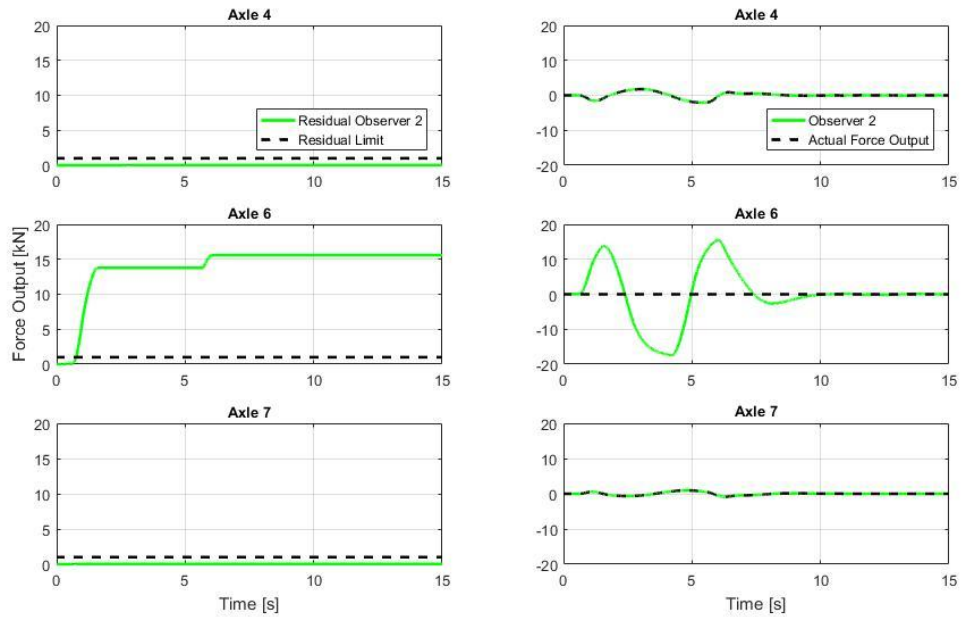


Figure 4.79 Time history of Observer 2's residual signals, the threshold limits, force output estimates, and the actual force outputs under the SLC maneuver for Axle 6's actuator malfunction.

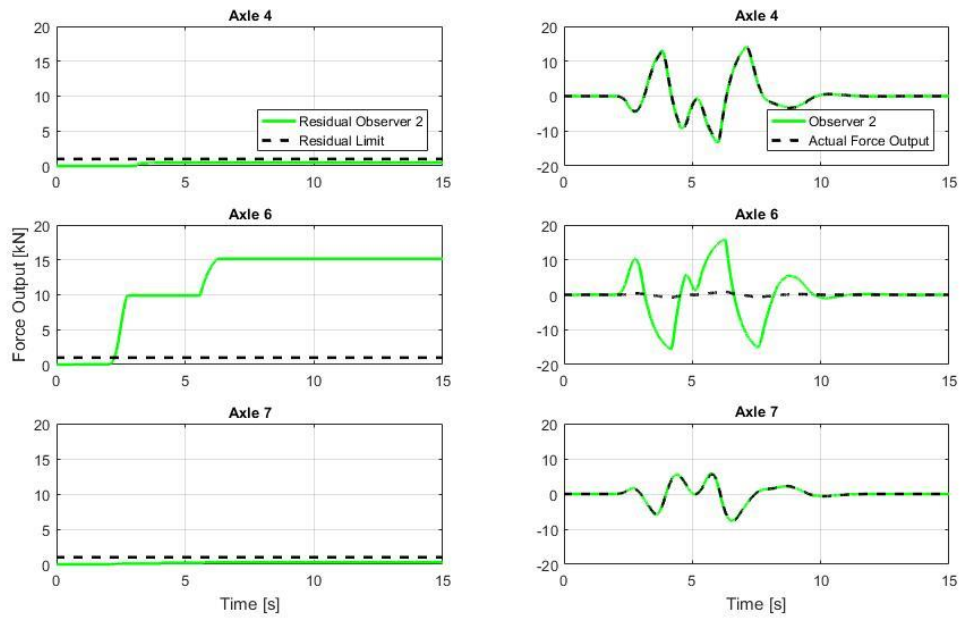


Figure 4.80 Time history of Observer 2's residual signals, the threshold limits, force output estimates, and the actual force outputs under the DLC maneuver for Axle 6's actuator malfunction.

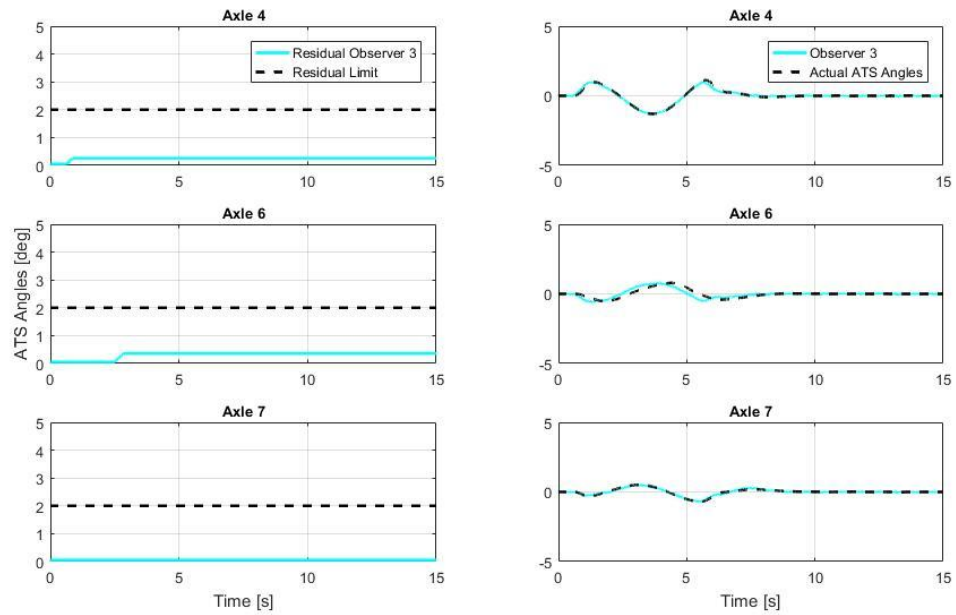


Figure 4.81 Time history of Observer 3's residual signals, the threshold limits, ATS angle estimates, and the actual ATS angles under the SLC maneuver for Axle 6's actuator malfunction.

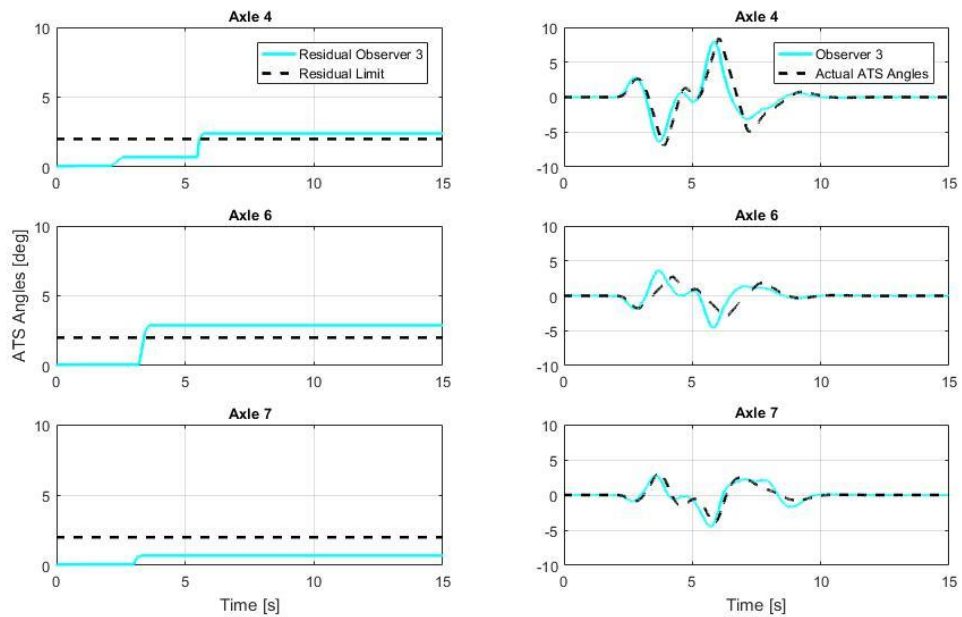


Figure 4.82 Time history of Observer 3's residual signals, the threshold limits, ATS angle estimates, and the actual ATS angles under the DLC maneuver for Axle 6's actuator malfunction.

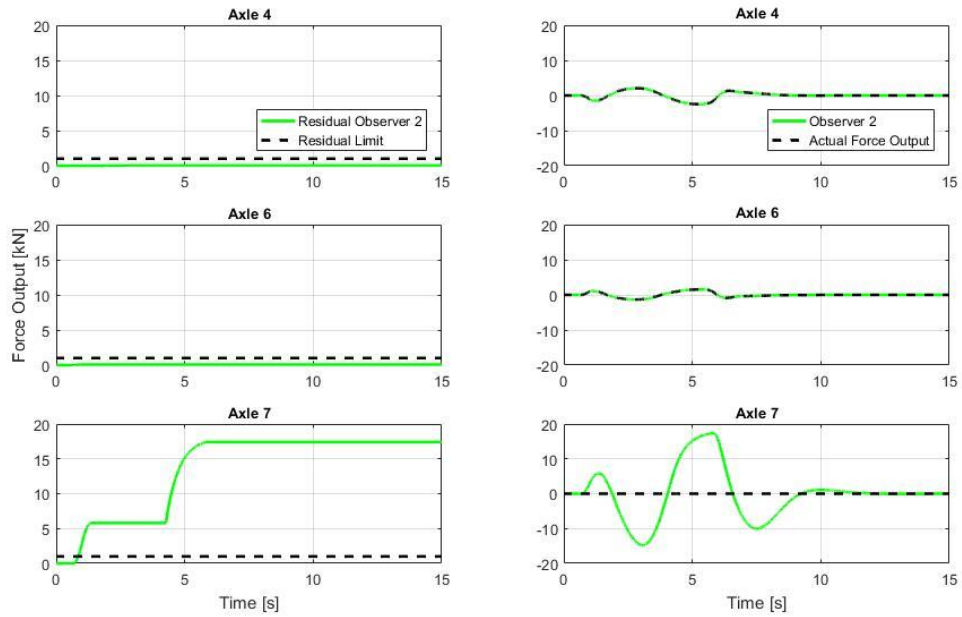


Figure 4.83 Time history of Observer 2's residual signals, the threshold limits, force output estimates, and the actual force outputs under the SLC maneuver for Axle 7's actuator malfunction.

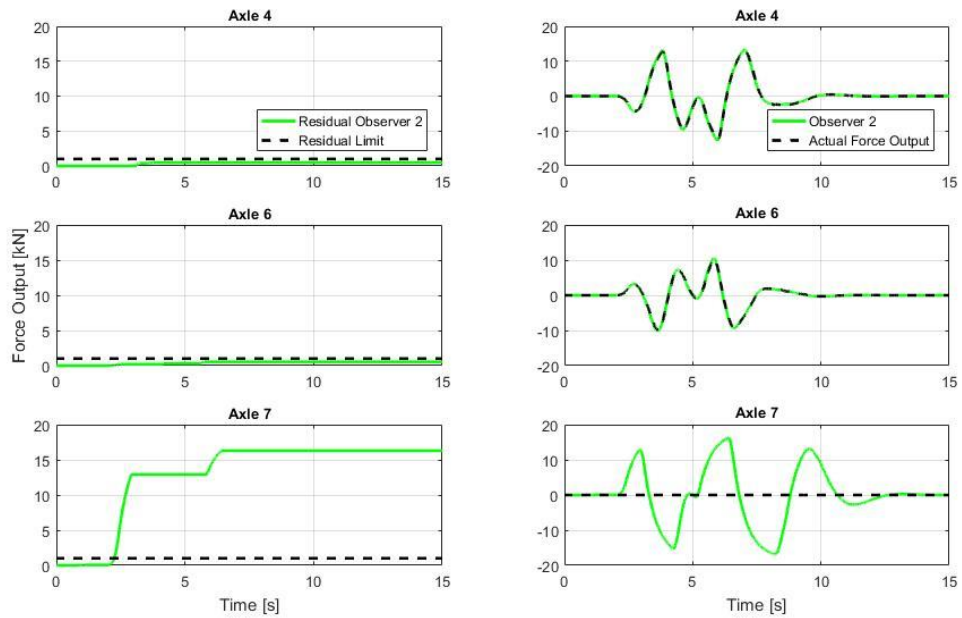


Figure 4.84 Time history of Observer 2's residual signals, the threshold limits, force output estimates, and the actual force output under the DLC maneuver for Axle 7's actuator malfunction.

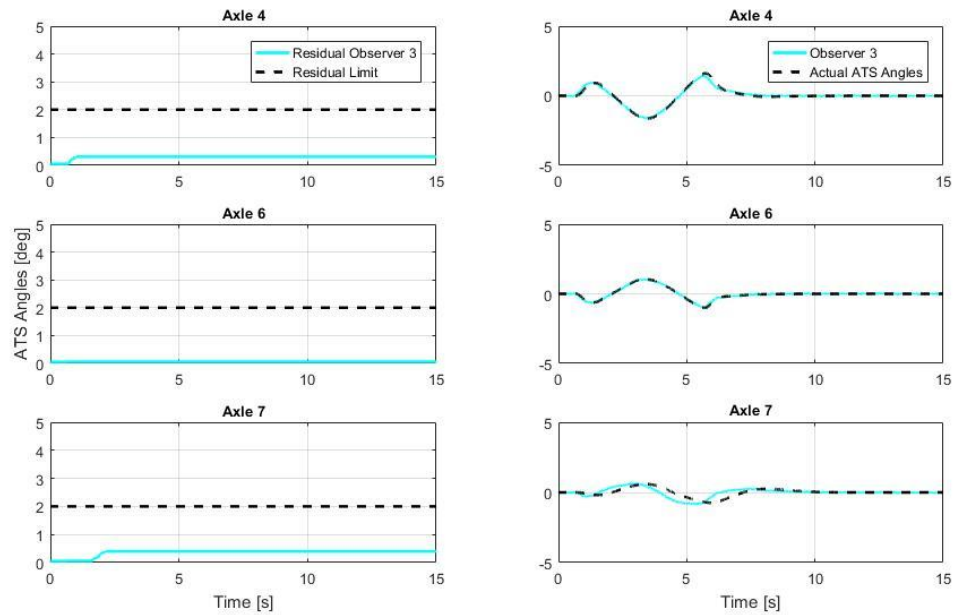


Figure 4.85 Time history of Observer 3's residual signals, the threshold limits, ATS angle estimates, and the actual ATS angles under the SLC maneuver for Axle 7's actuator malfunction.

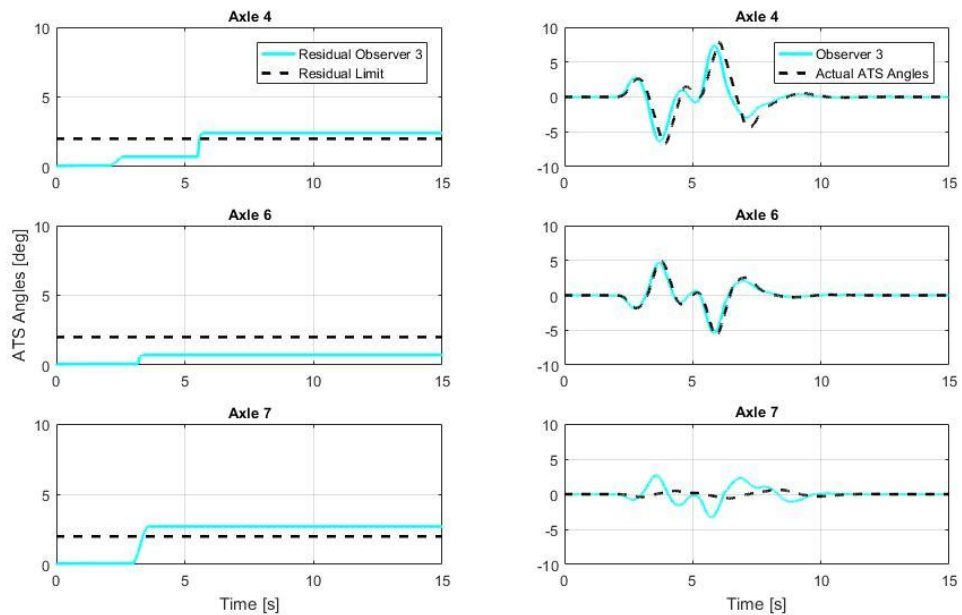


Figure 4.86 Time history of Observer 3's residual signals, the threshold limits, ATS angle estimates, and the actual ATS angles under the DLC maneuver for Axle 7's actuator malfunction.

#### **4.5.5.3. Fail-Safe Operation**

As mentioned in Section 4.5.4.3, the ATS axles are locked (fail-safe mode) if the difference in peak lateral acceleration achieved by the second trailer for the baseline and ATS vehicle exceeds the threshold. During the numerous fault conditions simulated in the above sub-sections, the analytical redundancy in the FTC-ATS scheme was able to maintain acceptable performance.

However, during Axle 4's simulated malfunction, the residual exceeded the prescribed limit. This sub-section illustrates the functioning of the fail-safe operation during Axle 4's malfunction. In Fig. 4.87, the lateral acceleration response of the controlled vehicle with the faulty Axle 4 and the vehicle without ATS are compared. The degraded performance is noticeable, specifically for the second trailer. This is further highlighted in Fig. 4.88, which illustrates the residual signal.

To compensate for the degraded performance of the second trailer, the FTC system initiates the Axle locking. Fig. 4.89 and 4.90 illustrate the results. Fig. 4.89 shows the effects of FTC intervention. It is clear that FTC ensures that the performance does not deteriorate. Whereas, Fig. 4.90 shows the generated ATS angles with and without FTC intervention. The figure clearly indicates the functioning of the FTC system, where the ATS axles are locked if the residual signal surpasses the limits. The initiation of Axle locking is marked in the figures.

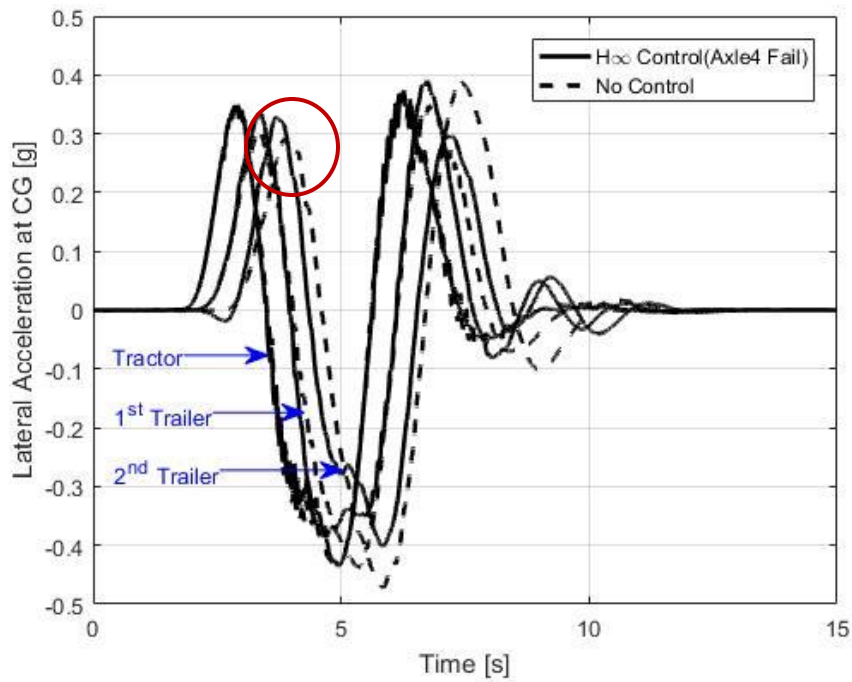


Figure 4.87 Time history of lateral accelerations for the  $H^\infty$  controlled vehicle and the baseline TruckSim vehicle under the DLC maneuver for Axle 4's actuator malfunction.

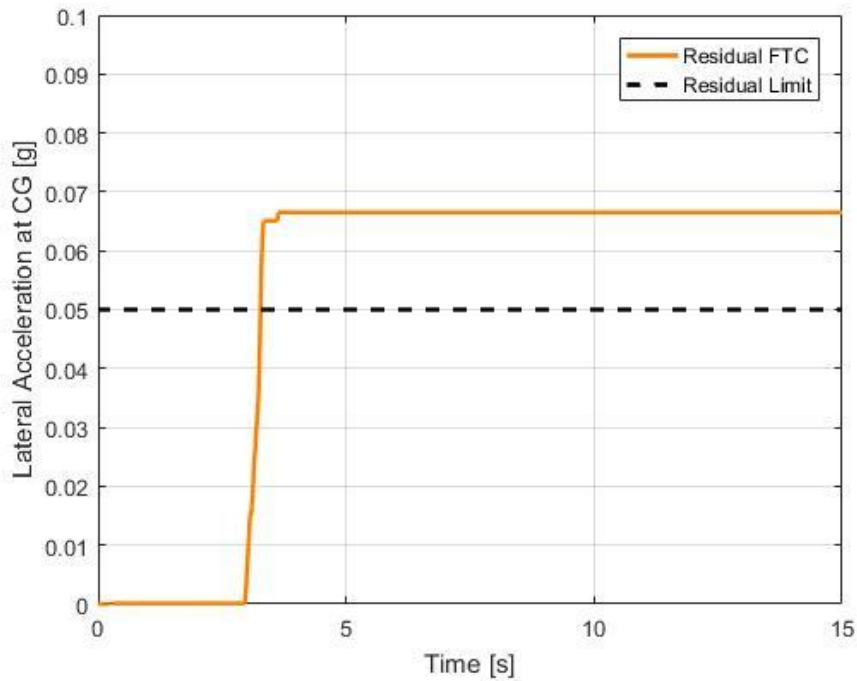


Figure 4.88 Time history of FTC system's residual signal and the threshold limit under the DLC maneuver for Axle 4's actuator malfunction.

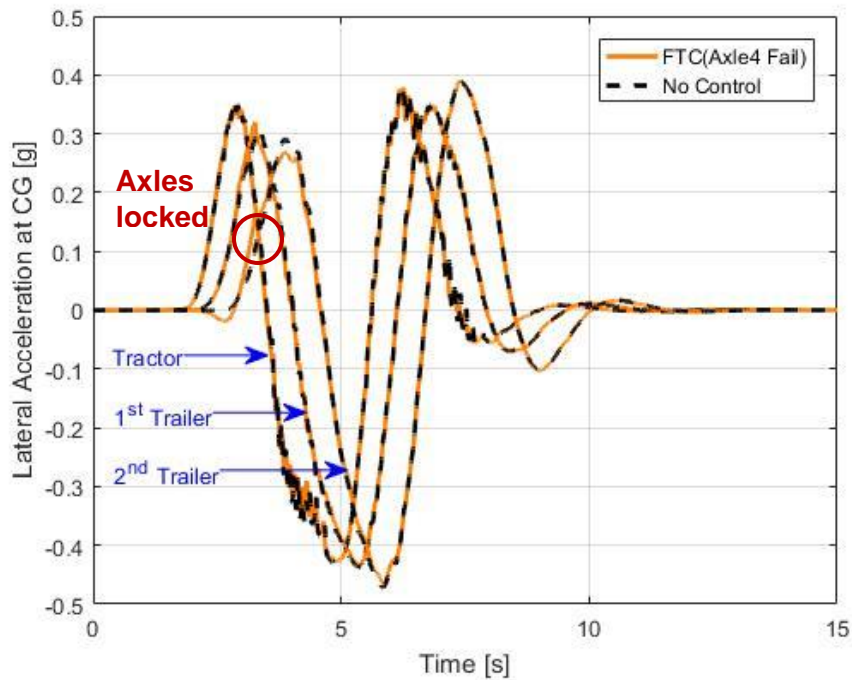


Figure 4.89 Time history of lateral accelerations for the FTC vehicle and the baseline TruckSim vehicle under the DLC maneuver for Axle 4's actuator malfunction.

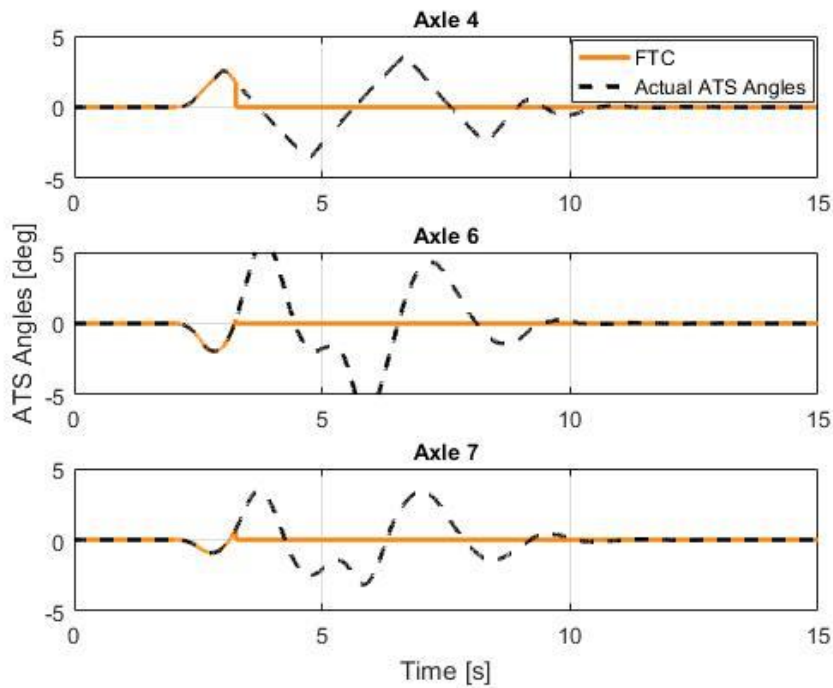


Figure 4.90 Time history of ATS angles generated by the FTC system, and the actual ATS angles under the DLC maneuver for Axle 4's actuator malfunction.

## 4.6. Summary

This chapter presented the FTC-ATS framework. The framework comprises of three fundamental elements, the ATS controller, the FDD system, and the FTC system. For the ATS controller design, LQR and  $H^\infty$  techniques were examined as the potential control techniques. Compared to the baseline vehicle, both control techniques illustrated enhanced vehicle performance. However, the  $H^\infty$  based controller demonstrated superior performance, and was chosen as the appropriate ATS controller. Further, the effects of actuator dynamics on the ATS controller's performance were evaluated. The results affirmed the actuator's capability to meet the controller's demands during most operating conditions.

Luenberger Observer and Kalman Filter estimation techniques were analyzed as prospective observer techniques. Compared to the Luenberger Observer, the Kalman Filter demonstrated better overall performance. Hence, the Kalman Filter technique was selected as the suitable observer technique for FDD system development.

Thereafter, the FDD and the FTC systems were presented. The FDD system employs three independent observers, where each observer monitors a dedicated sub-system. All observers illustrated good tracking performance. Then, the FTC system and the fault tolerance logic was described. Finally, the simulation results for a variety of instigated faults and malfunctions were presented. Scenarios such as yaw rate sensor failure and actuator malfunction were emulated. The FTC system demonstrated excellent performance during all simulated fault scenarios.

# CHAPTER 5

## CONCLUSIONS and RECOMMENDATIONS FOR FUTURE RESEARCH

### 5.1. Conclusions

MTAHVs are essential to the trucking industry. However, their limitations overshadow their advantages. To allow MTAHV's widespread applications, it is necessary to address these limitations. Thus, in this research, a Fault Tolerant Control of Active Trailer Steering (FTC-ATS) scheme was developed. The scheme constitutes primarily of the control system, the Fault Detection and Diagnosis (FDD) system, and the FTC system.

The LQR and  $H^\infty$  control techniques were investigated for their suitability in the FTC-ATS scheme. Although, the LQR control system was effective in enhancing the vehicle's dynamics under the SLC maneuver, the controller could not provide desired results under the DLC maneuver. Moreover, the path-following of the LQR controlled vehicle was erroneous. Based on the results, it is suggested that the LQR controller must be revised. Techniques, such as gain-scheduling and reference tracking, are suggested to enhance the suitability of a LQR controller for ATS systems. Considering the limitations of the LQR control, a robust  $H^\infty$  controller was synthesized. The  $H^\infty$  controller for the ATS system demonstrated enhanced vehicle performance under both SLC and DLC maneuvers. The yaw rate reference model enabled the  $H^\infty$  control system to exhibit excellent path following. Moreover, the controller exhibited excellent yaw reference tracking.

To include actuators' dynamics in the control system, the ATS Hydraulic Actuation (AHA) system was integrated with the LQR and  $H^\infty$  controllers. Based on the simulation results, it is suggested that an actuator model should be incorporated during control system design. This helps establish the system's physical limitations.

To develop a comprehensive FDD system, the commonly used observer techniques, Luenberger Observer and Kalman Filter, were cross-examined. Both observer techniques were compared under different simulation conditions. Results suggest that the Luenberger Observer is suitable for application in state feedback control as a state estimator. Whereas, the Kalman Filter is suggested for generating accurate predictions especially for control and diagnosis systems.

The FDD system comprises of three individual observers, which monitor the designated sub-systems. Observer 1 estimates the yaw rate of the vehicle based on the available individual wheel speeds. Observer 2 predicts the force output of the system and is responsible for fault diagnosis of the actuation system, whereas Observer 3 monitors the controller and hydraulic actuation system simultaneously. Observer 1 and 3 employ the Kalman Filter for accurate prediction of the system's states in the presence of measurement noise. Simulation results conclude that Observer 1 is capable of accurately predicting the yaw rates. While Observer 2 is equipped to diagnose the faults concerning the actuation system, and can predict the faults in individual axles. Observer 3 effectively diagnoses the faults in actuation system and controller. The combination of these observers generates an effective FDD system.

By combining the robust  $H^\infty$  controller and the FDD system, the FTC system was synthesized. The FTC system compares the ATS-enabled vehicle's performance with the baseline vehicle to determine the degree of intervention. Specifically, a residual signal formulated by comparing the second trailer's peak lateral acceleration response of the controlled and the uncontrolled vehicles quantifies the variation in performance. The FTC system's Fail-Operational (FO) and Fail-Safe (FS) modes define the different degrees of intervention. The ATS system remains operational in the FO mode, until a system failure causes the vehicle to exhibit worse dynamics than the uncontrolled vehicle. However, in the FS mode, if the controlled vehicle shows worse dynamics, all ATS axles are locked. Simulation results suggest that the FTC system prevents the vehicle from exhibiting worse dynamic performance. Moreover, the FTC system's intervention allows the vehicle to maintain safe operation.

A primary objective of this research was to allow the transition of ATS systems from laboratory experiments to real world systems. This mandated the study to analyze the performance of such systems in presence of fault and failures. In this research, the performance of the ATS systems was analyzed under numerous simulated fault and failure scenarios. In addition, the impact of failures on the vehicle's dynamic characteristics was examined. To permit the ATS system to remain operational in presence of such faults, a novel FTC scheme was developed. The results indicate that the combination of the robust  $H^\infty$  controller and FDD system generates a capable FTC scheme. It can be concluded that this study will aid the ATS systems to achieve widespread implementation in MTHAVs.

## 5.2. Recommendations for Future Research

Based on the obtained results and conclusions, the following recommendations are provided for future work.

In this research, the  $H^\infty$  control system utilizes a yaw rate reference model based on a simple steady-state bicycle model. More complex reference models maybe explored. Additionally, Driver-In-the-Loop (DIL) simulation is suggested to study the impact of human behavior on the system's performance. DIL will allow the study of human-hardware interaction during faults. Furthermore, Hardware-In-the-Loop (HIL) simulation is suggested to corroborate the ATS Hydraulic Actuation (AHA) system.

Observer 1 estimates the vehicle's yaw rates by utilizing a linear vehicle model. Although the model provides reasonable yaw rate predictions, complex non-linear models may be explored. Moreover, extended Kalman Filter may be employed for the non-linear model. This strategy would provide accurate predictions by accounting the nonlinearities of the system. In this study, the sensor noise was approximated using Simulink. In the future studies, realistic sensor noise data from real sensors can be considered. This will allow better understanding of the noise rejection abilities of the Kalman Filter.

The presented FTC-ATS framework exhibited good performance under the numerical simulation environment. However, its effectiveness cannot be adequately evaluated without analyzing it in the real world. The physical implementation of such a complex system will involve additional efforts, specifically

in the areas of design and testing. For example, to facilitate ATS system's implementation, the controller may require use of different control strategies for high-speed and low-speed operations.

It is well established that ATS systems involve high costs, which usually leads to their limited applications. Thus, alternative methods may be explored for implementing a low cost ATS system. A low cost ATS system may be developed by reducing the number of required ATS axles, and developing a design that requires minimum modification to the current hardware.

In relation to the proposed FTC scheme, a quantitative analyses of the computational requirements of the presented analytical model(s) should be conducted. Moreover, to analyze the effectiveness of the presented FTC-ATS scheme adequately, rigorous road testing is required. Specifically, by using the automotive industry standard, CAN bus communication architecture. This study will assist in analyzing the limitations of the FTC-ATS scheme.

Furthermore, the proposed FTC-ATS ensures that the controlled vehicle's performance never degrades below the uncontrolled vehicle's performance. However, FTC systems are capable of ensuring desired (controlled) performance despite of the occurrence of faults. This may be achieved by generating individual controllers for each fault scenario, such that the functional actuators compensate for the loss of the faulty actuator(s).

## PUBLICATIONS

1. Lee E., Kapoor S., Sikder T., and He Y. "An optimal robust controller for active trailer differential braking systems of car-trailer combinations" *International Journal of Vehicle Systems Modelling and Testing* (2017) (In Press)
2. Kapoor S., Sikder T., and He Y. "Fault-Tolerant Control of Active Trailer Steering Systems for Multi-Trailer Articulated Heavy Vehicles". *Proceedings of the 25th Symposium of the International Association for Vehicle System Dynamics (IAVSD 2017)* (2017) (Submitted).

## REFERENCES

- [1] Fancher, P., and Winkler, C. "Directional performance issues in evaluation and design of articulated heavy vehicles." *Vehicle System Dynamics* 45, no. 7-8 (2007): 607-647.
- [2] Gul, T., Ahad S., Jacqui S., and Shawn W. "Transport Statistics Great Britain: 2006 Edition." (2006)
- [3] Oberoi, D. "Enhancing roll stability and directional performance of articulated heavy vehicles based on anti-roll control and design optimization." *Master Thesis University of Ontario Institute of Technology* (2011).
- [4] Bienkowski, B., and Walton, M. "The economic efficiency of allowing longer combination vehicles in Texas, No. SWUTC/11/476660-00077-1." *Southwest Region University Transportation Center, Center for Transportation Research, University of Texas at Austin* (2011).
- [5] Woodrooffe, J., and Ash, L. "Economic Efficiency of Long Combination Transport Vehicles in Alberta", *Final Report. Woodrooffe & Associates*, 2001.
- [6] Zhu, S. "Coordinated control of active safety systems for multi-trailer articulated heavy vehicles." *PhD Thesis University of Ontario Institute of Technology* (2016).
- [7] Wang, Q. "Design and validation of active trailer steering systems for articulated heavy vehicles using driver-hardware-in-the-loop real-time simulation". *Master Thesis University of Ontario Institute of Technology* (2015).
- [8] Islam, M.M. "Design synthesis of articulated heavy vehicles with active trailer steering systems." *Master Thesis University of Ontario Institute of Technology* (2010).
- [9] Adams, T., Kleinmaier, D., Marach, A., Helfrich, G., Levine, J., and Bittner, J. "Longer Combination Vehicles: An Estimation of their Benefits and Public Perception of Their Use." No. *CFIRE 05-01* (2012).

- [10] Ni, Z. "Design and validation of high speed active trailer steering system for articulated heavy vehicle." *Master Thesis University of Ontario Institute of Technology* (2016).
- [11] Uffelmann, F. "Automotive stability and handling dynamics in cornering and braking maneuvers." *Vehicle System Dynamics* 12, no. 4-5 (1983): 203-223.
- [12] Winkler, C., Blower, D., and Ervin, R. "Rollover of Heavy Commercial Vehicles." *No. UMTRI-99-19* (1999).
- [13] Islam, M.M. "Parallel design optimization of multi-trailer articulated heavy vehicles with active safety systems." *PhD Thesis University of Ontario Institute of Technology* (2013).
- [14] Edgar, J. "Development of performance standards for Australian heavy vehicles." In *Eighth International Symposium on Heavy Vehicle Weights and Dimensions* (2004).
- [15] Winkler, C. "Rollover of heavy commercial vehicles." *UMTRI Research Review*, 31(2001), pp. 1-17
- [16] El-Gindy, M., Tong, L., and Tabarrok, B. "Frequency Response Analysis of Canadian Logging Trucks." *Vehicle System Dynamics* 23, no. 1 (1994): 325-349.
- [17] Palkovics, L., and El-Gindy, M. "Design of an active unilateral brake control system for five-axle tractor-semitrailer based on sensitivity analysis." *Vehicle System Dynamics* 24, no. 10 (1995): 725-758.
- [18] El-Gindy, M., Mrad, N., and Tong, X. "Sensitivity of rearward amplification control of a truck/full trailer to tyre cornering stiffness variations." *Proceedings of the Institution of Mechanical Engineers, Part D: Journal of Automobile Engineering* 215, no. 5 (2001): 579-588.
- [19] Braghin, F., Cheli, F., Corradi, R., Tomasini, G., and Sabbioni, E. "Active anti-rollover system for heavy-duty road vehicles." *Vehicle System Dynamics* 46, no. S1 (2008): 653-668.

- [20] Dahlberg, E., and Stensson, A. "The dynamic rollover threshold-a heavy truck sensitivity study." *International journal of vehicle design* 40, no. 1-3 (2005): 228-250.
- [21] Fancher, P. "The static stability of articulated commercial vehicles." *Vehicle System Dynamics* 14, no. 4-6 (1985): 201-227.
- [22] Rakheja, S. "Estimation of rollover threshold of partially filled tank trucks." *Proceedings of the Institution of Mechanical Engineers, Part D: Journal of Automobile Engineering* 205, no. 1 (1991): 69-71.
- [23] Gertsch, J., and Eichelhard, O. "Simulation of dynamic rollover threshold for heavy trucks." *SAE Technical Paper*, no. 2003-01-3385 (2003).
- [24] Lee, E. "Design optimization of active trailer differential braking systems for car-trailer combinations." *Master Thesis University of Ontario Institute of Technology* (2016).
- [25] Blanke, M., Kinnaert, M., Lunze, J., Staroswiecki, M. and Schröder, J. "Diagnosis and Fault-Tolerant Control." *Springer-Verlag Berlin Heidelberg* (2016).
- [26] Isermann, R., Schwarz, R., and Stolzl S. "Fault-tolerant drive-by-wire systems." *IEEE Control Systems* 22, no. 5 (2002): 64-81.
- [27] Yin, S., Hao L., and Ding, S. "Real-time implementation of fault-tolerant control systems with performance optimization." *IEEE Transactions on Industrial Electronics* 61, no. 5 (2014): 2402-2411.
- [28] He, Y., and Islam M.M. "An automated design method for active trailer steering systems of articulated heavy vehicles." *Journal of Mechanical Design* 134, no. 4 (2012): 041002.
- [29] Wang, Q., and He, Y. "Design validation of active trailer steering systems for improving the low-speed manoeuvrability of multi-trailer articulated heavy vehicles using driver-hardware/software-in-the-loop real-time simulations." *International Journal of Vehicle Performance* 2, no. 1 (2015): 58-84.

- [30] He, Y., Islam M.M., and Webster, T. "An integrated design method for articulated heavy vehicles with active trailer steering systems." *SAE Int. J. of Passenger Cars-Mechanical Systems* (2010): 158-174.
- [31] Ding, X., Mikaric, S. and He, Y. "Design of an active trailer-steering system for multi-trailer articulated heavy vehicles using real-time simulations." *Proceedings of the Institution of Mechanical Engineers, Part D: Journal of automobile engineering* 227, no. 5 (2013): 643-655.
- [32] Jujnovich, B. "Active steering of articulated vehicles." *PhD Thesis, University of Cambridge* (2006).
- [33] Cheng, C., Roebuck, R., Odhams, A. and Cebon, D. "High-speed optimal steering of a tractor–semitrailer." *Vehicle system dynamics* 49, no. 4 (2011): 561-593.
- [34] Cheng, C., and Cebon, D. "Improving roll stability of articulated heavy vehicles using active semi-trailer steering." *Vehicle System Dynamics* 46, no. S1 (2008): 373-388.
- [35] Rangavajhula, K., and Tsao, J. "Command steering of trailers and command-steering-based optimal control of an articulated system for tractor-track following." *Proceedings of the Institution of Mechanical Engineers, Part D: Journal of Automobile Engineering* 222, no. 6 (2008): 935-954.
- [36] Rangavajhula, K., and Tsao, J. "Active trailer steering control of an articulated system with a tractor and three full trailers for tractor-track following." *International Journal of Heavy Vehicle Systems* 14, no. 3 (2007): 271-293.
- [37] Kim, K.I., Guan, H., Wang, B., Guo, R., and Liang, F. "Active steering control strategy for articulated vehicles." *Frontiers of Information Technology & Electronic Engineering* 17 (2016): 576-586.
- [38] Abroshan, M., Taiebat, M., Goodarzi, A., and Khajepour, A. "Automatic steering control in tractor semi-trailer vehicles for low-speed maneuverability enhancement." *Proceedings of the Institution of Mechanical Engineers, Part K: Journal of Multi-body Dynamics* (2016).

- [39] Odhams, A.M.C., Roebuck, R.L. and Cebon, C. "Implementation of active steering on a multiple trailer long combination vehicle." *Cambridge University, Engineering Department*, (2010): 1-13.
- [40] Kang, J.Y., Burkett, G., Bennett, D. and Velinsky, S.A. "Nonlinear Vehicle Dynamics and Trailer Steering Control of the TowPlow, a Steerable Articulated Snowplowing Vehicle System." *Journal of Dynamic Systems, Measurement, and Control*, 137, no. 8 (2015): 081005.
- [41] Mary, A.D., Mathew, A.T. and Jacob, J. "A Robust H-infinity Control Approach of Uncertain Tractor Trailer System." *IETE Journal of Research*, Vol. 59, Issue 1 (2013).
- [42] Yang, X. "Optimal reconfiguration control of the yaw stability of the tractor-semitrailer vehicle." *Mathematical Problems in Engineering* 2012 (2012).
- [43] Mokhiamar, O. "Stabilization of car-caravan combination using independent steer and drive/or brake forces distribution." *Alexandria Engineering Journal* 54, no. 3 (2015): 315-324.
- [44] Ding, X., He, Y., Ren, J., and Sun, T. "A comparative study of control algorithms for active trailer steering systems of articulated heavy vehicles." *American Control Conference (ACC)*, (2012) (pp. 3617-3622). IEEE.
- [45] Sun, T., Lee, E., and He, Y. "Non-Linear Bifurcation Stability Analysis for Articulated Vehicles with Active Trailer Differential Braking Systems". *SAE Int. J. Mater. Manf.* 9(3) (2016), doi:10.4271/2016-01-0433.
- [46] Kharrazi, S., Lidberg, M., and Fredriksson, J. "A generic controller for improving lateral performance of heavy vehicle combinations." *Proceedings of the Institution of Mechanical Engineers, Part D: Journal of Automobile Engineering* 227, no. 5 (2013): 619-642.
- [47] Islam, M.M., Ding, X., and He, Y. "A closed-loop dynamic simulation-based design method for articulated heavy vehicles with active trailer steering systems." *Vehicle system dynamics* 50, no. 5 (2012): 675-697.

- [48] Lee E., Kapoor S., Sikder T., and He Y. "An optimal robust controller for active trailer differential braking systems of car-trailer combinations." *International Journal of Vehicle Systems Modelling and Testing* (2017) (In Press).
- [49] Pacejka, H. "Tire and vehicle dynamics". Warrendale, *Society of Automotive Engineers* (2006).
- [50] Gu, D.W., Petkov, P., and Konstantinov, M.M. "Robust control design with MATLAB®." *Springer Science & Business Media* (2005).
- [51] D'Urso, P. "Development of  $H^\infty$  control strategy for a multi-wheeled combat vehicle." *Master Thesis University of Ontario Institute of Technology* (2016).
- [52] Skogestad, S., and Postlethwaite, I. "Multivariable feedback control: analysis and design." Vol. 2. New York: *Wiley* (2007).
- [53] Glover, K., and McFarlane, D. "Robust stabilization of normalized coprime factor plant descriptions with  $H^\infty$ -bounded uncertainty." *IEEE transactions on automatic control* 34, no. 8 (1989): 821-830.
- [54] Horiuchi, S., Yuhara, N., and Takei, A. "Two degree of freedom/ $H^\infty$  controller synthesis for active four wheel steering vehicles." *Vehicle System Dynamics* 25, no. S1 (1996): 275-292.
- [55] Lv, H.M., Nan C., and Pu L. "Multi-objective  $H^\infty$  optimal control for four-wheel steering vehicle based on yaw rate tracking." *Proceedings of the Institution of Mechanical Engineers, Part D: Journal of Automobile Engineering* 218, no. 10 (2004): 1117-1123.
- [56] Zhao, W.Z., Li, Y.J., Wang, C.Y., Zhao, T., and Gu, X.Y. " $H^\infty$  control of novel active steering integrated with electric power steering function." *Journal of Central South University* 20, no. 8 (2013): 2151-2157.
- [57] Guvenc, B.A., Bunte, T., Odenthal, D., and Guvenc, L. "Robust two degree-of-freedom vehicle steering controller design." *IEEE Transactions on Control Systems Technology* 12, no. 4 (2004): 627-636.

- [58] Hingwe, P., Tan, H.S., Packard, A.K., and Tomizuka, M. "Linear parameter varying controller for automated lane guidance: experimental study on tractor-trailers." *IEEE Transactions on control systems technology* 10, no. 6 (2002): 793-806.
- [59] Chen, B.S., Wu, C.S., and Uang, H.J. "A minimax tracking design for wheeled vehicles with trailer based on adaptive fuzzy elimination scheme." *IEEE Transactions on Control Systems Technology* 8, no. 3 (2000): 418-434.
- [60] Sun, H., and Yan, L. "Robust Fuzzy Control for Nonlinear Discrete-Time Stochastic Systems with Markovian Jump and Parametric Uncertainties." *Mathematical Problems in Engineering* 2014 (2014).
- [61] Wang, R., Jing, H., Karimi, H.R., and Chen, N. "Robust fault-tolerant  $H^\infty$  control of active suspension systems with finite-frequency constraint." *Mechanical Systems and Signal Processing* 62 (2015): 341-55.
- [62] Zhang, Y., and Jiang, J. "Bibliographical review on reconfigurable fault-tolerant control systems." *Annual reviews in control* 32, no. 2 (2008): 229-252.
- [63] Wanner, D., Stensson Trigell, A., Drugge, L., and Jerrelind, J. "Survey on fault-tolerant vehicle design." In *26th Electric Vehicle Symposium, (EVS26), Los Angeles, CA* (2012).
- [64] Isermann, R. "Fault-diagnosis systems: an introduction from fault detection to fault tolerance." *Springer Science & Business Media* (2006).
- [65] Odhams, A.M.C., Roebuck, R.L., Cebon, D. and Winkler, C.B. "Dynamic safety of active trailer steering systems." *Proceedings of the Institution of Mechanical Engineers, Part K: Journal of Multi-body Dynamics*, 222(4), no. 4 (2008): 367-380.
- [66] Oudghiri, M., Chadli, M., and El Hajjaji, A. "Robust observer-based fault-tolerant control for vehicle lateral dynamics." *International Journal of vehicle design* 48, no. 3-4 (2008): 173-189.

- [67] Frank, P.M. "Fault diagnosis in dynamic systems using analytical and knowledge-based redundancy: A survey and some new results." *automatica* 26, no. 3 (1990): 459-474.
- [68] Isermann, R. "Diagnosis methods for electronic controlled vehicles." *Vehicle System Dynamics* 36, no. 2-3 (2001): 77-117.
- [69] Jeppesen, B.P., and Cebon, D. "Analytical redundancy techniques for fault detection in an active heavy vehicle suspension." *Vehicle System Dynamics* 42, no. 1-2 (2004): 75-88.
- [70] Jeppesen, B.P., and Cebon, D. "Application of observer-based fault detection in vehicle roll control." *Vehicle System Dynamics* 47, no. 4 (2009): 465-495.
- [71] Alkaya, A., and Ilyas E. "Luenberger observer-based sensor fault detection: online application to DC motor." *Turkish Journal of Electrical Engineering & Computer Sciences* 22, no. 2 (2014): 363-370.
- [72] You, S.H., Cho, Y.M., and Hahn, J.O. "Model-based fault detection and isolation in automotive yaw moment control system." *International Journal of Automotive Technology* 18, no. 3 (2017): 405-416.
- [73] Luenberger, D. "An introduction to observers." *IEEE Transactions on automatic control* 16, no. 6 (1971): 596-602.
- [74] Hu, X., Sun, F., and Zou, Y. "Estimation of state of charge of a lithium-ion battery pack for electric vehicles using an adaptive Luenberger observer." *Energies* 3, no. 9 (2010): 1586-1603.
- [75] Ibaraki, S., Suryanarayanan, S. and Tomizuka, M. "Design of Luenberger state observers using fixed-structure H-infinity optimization and its application to fault detection in lane-keeping control of automated vehicles". *IEEE-ASME TRANSACTIONS ON MECHATRONICS*, 10(1) (2005) 34-42.
- [76] Cherouat, H., Braci, M., and Diop, S. "Vehicle velocity, side slip angles and yaw rate estimation." In *Industrial Electronics, 2005. ISIE 2005. Proceedings of the IEEE International Symposium on*, vol. 1, pp. 349-354. IEEE, 2005.

- [77] Kalman, R.E. "A new approach to linear filtering and prediction problems." *Journal of basic Engineering* 82, no. 1 (1960): 35-45.
- [78] Grewal, M.S., and Andrews, A.P. "Applications of Kalman filtering in aerospace 1960 to the present [historical perspectives]." *IEEE Control Systems* 30, no. 3 (2010): 69-78.
- [79] Sivashankar, N., and Ulsoy, A.G. "Yaw rate estimation for vehicle control applications." *TRANSACTIONS-AMERICAN SOCIETY OF MECHANICAL ENGINEERS JOURNAL OF DYNAMIC SYSTEMS MEASUREMENT AND CONTROL* 120 (1998): 267-274.
- [80] Venhovens, P.J., and Naab, K. "Vehicle dynamics estimation using Kalman filters." *Vehicle System Dynamics* 32, no. 2-3 (1999): 171-184.
- [81] Emirler, M.T., Kahraman, K., Şentürk, M., Aksun Güvenç, B., Güvenç, L., and Efendioğlu, B. "Vehicle yaw rate estimation using a virtual sensor." *International Journal of Vehicular Technology* 2013 (2013).
- [82] Kapoor S., Sikder T., and He Y. "Fault-Tolerant Control of Active Trailer Steering Systems for Multi-Trailer Articulated Heavy Vehicles". *Proceedings of the 25th Symposium of the International Association for Vehicle System Dynamics (IAVSD 2017)* (2017) (Submitted).
- [83] Islam, M.M., He, Y., Zhu, S., and Wang, Q., "A comparative study of multi-trailer articulated heavy-vehicle models." *Proceedings of the Institution of Mechanical Engineers, Part D: Journal of Automobile Engineering* 229, no. 9 (2015): 1200-1228.
- [84] Truck and Bus Powertrain Steering Committee. "A Test for Evaluating the Rearward Amplification of Multiarticulated Vehicles." *SAE Standard J 2179* (1993).
- [85] Manring, N. "Hydraulic control systems". *Wiley* (2005).
- [86] Vu, V.T., Sename, O., Dugard, L., and Gáspár, P. "Enhancing roll stability of heavy vehicle by LQR active anti-roll bar control using electronic servo-valve hydraulic actuators." *Vehicle System Dynamics* 55, no. 9 (2017): 1405-1429.

- [87] Miège, A.J.P., and Cebon, D. "Active roll control of an experimental articulated vehicle." *Proceedings of the Institution of Mechanical Engineers, Part D: Journal of Automobile Engineering* 219, no. 6 (2005): 791-806.
- [88] Boettcher, K., Broekema, M., Drempevic, K., Rodrigues, C., Sayin, M., and Smith, P. "Design and Validation of Electro-hydraulic Steering Actuators for Heavy Trailers", *Capstone Design Project Report, University of Ontario Institute of Technology*, (2015): 70 pages.
- [89] Rafa, A.H.A.B., Yahya, A.F., Rawand, E.J.T., and Talabani, J. "A study on the effects of servovalve lap on the performance of a closed-loop electrohydraulic position control system." *Al-Rafidain Engineering* 17, no. 5 (2009).
- [90] MathWorks. "Model and simulate multidomain physical systems." [Online]. Available: <https://www.mathworks.com/products/simscape.html>. Accessed: July 31<sup>st</sup>, 2017.
- [91] Piłat, A., and Włodarczyk, P. "The  $\mu$ -synthesis and analysis of the robust controller for the active magnetic levitation system." *Automatyka/Akademia Górniczo-Hutnicza im. Stanisława Staszica w Krakowie* 15, no. 1 (2011): 85-98.
- [92] Mares, C., and Surace, C. "An application of genetic algorithms to identify damage in elastic structures." *Journal of sound and vibration* 195, no. 2 (1996): 195-215.
- [93] Poussot-Vassal, C., Sename, O., Fergani, S., Doumiati, M., and Dugard, L. "Global chassis control using coordinated control of braking/steering actuators." *Robust Control and Linear Parameter Varying approaches: application to vehicle dynamics* 437 (2013): 237.
- [94] Zhu, S., and He, Y. "A driver-adaptive stability control strategy for sport utility vehicles." *Vehicle System Dynamics* 55, no. 8 (2017): 1206-1240.
- [95] Yoon, J., Yim, S., Cho, W., Koo, B., and Yi, K. "Design of an unified chassis controller for rollover prevention, manoeuvrability and lateral stability." *Vehicle system dynamics* 48, no. 11 (2010): 1247-1268.

- [96] El-Gindy, M. "Course Notes on Vehicle Dynamics and Control (ENGR 5300G)" *University of Ontario Institute of Technology* (2011): Chapter 2.2.
- [97] Patki, V.V., Sonwane, D.N., Ingole, D.D., and Naik, V.V. "Design and implementation of discrete augmented ziegler-nichols pid controller." *International Journal on Control System and Instrumentation* 4, no. 1 (2013): 16.
- [98] Williams, R.L., and Lawrence, D.A. "Linear state-space control systems." *John Wiley & Sons* (2007).
- [99] Dahleh, M., Dahleh, M.A., and Verghese, G. "Lectures on dynamic systems and control." *A+ A 4*, no. 100 (2004): 1-100.
- [100] Naik, N., Gemson, R.M.O., and Ananthasayanam, M.R. "Introduction to the Kalman filter and tuning its statistics for near optimal estimates and Cramer Rao bound." *arXiv preprint arXiv:1503.04313* (2015).
- [101] MathWorks. "Band-Limited White Noise." [Online]. Available: <https://www.mathworks.com/help/simulink/slref/bandlimitedwhitenoise.html> Accessed: July 31<sup>st</sup>, 2017.

## APPENDIX A: NOTATIONS OF THE 4DOF B-TRAIN DOUBLE MODEL PARAMETERS

Symbol	Parameter Description	Units
$m_1$	Total mass of the tractor	$kg$
$m_2$	Total mass of the first trailer	$kg$
$m_3$	Total mass of the second trailer	$kg$
$I_1$	Yaw moment of inertia of the tractor	$kg\ m^2$
$I_2$	Yaw moment of inertia of the first trailer	$kg\ m^2$
$I_3$	Yaw moment of inertia of the second trailer	$kg\ m^2$
$V_x$	Forward speed of the Vehicle	$\frac{m}{s}$
$V_{y1}$	Lateral speed of the tractor	$\frac{m}{s}$
$V_{y2}$	Lateral speed of the first trailer	$\frac{m}{s}$
$V_{y3}$	Lateral speed of the second trailer	$\frac{m}{s}$
$\dot{\psi}_1$	Yaw rate of the tractor	$\frac{deg}{s}$
$\dot{\psi}_2$	Yaw rate of the first trailer	$\frac{deg}{s}$
$\dot{\psi}_3$	Yaw rate of the second trailer	$\frac{deg}{s}$

$F_{y1}$	Lateral force of the tractor's 1 <sup>st</sup> axle	$N$
$F_{y2}$	Lateral force of the tractor's 2 <sup>nd</sup> axle	$N$
$F_{y3}$	Lateral force of the tractor's 3 <sup>rd</sup> axle	$N$
$F_{y4}$	Lateral force of the first trailer's 1 <sup>st</sup> axle	$N$
$F_{y5}$	Lateral force of the first trailer's 2 <sup>nd</sup> axle	$N$
$F_{y6}$	Lateral force of the first trailer's 3 <sup>rd</sup> axle	$N$
$F_{y7}$	Lateral force of the second trailer's 1 <sup>st</sup> axle	$N$
$F_{y8}$	Lateral force of the second trailer's 2 <sup>nd</sup> axle	$N$
$F_{y9}$	Lateral force of the second trailer's 3 <sup>rd</sup> axle	$N$
$F_{h1}$	Lateral reaction force at the 1 <sup>st</sup> fifth-wheel	$N$
$F_{h2}$	Lateral reaction force at the 2 <sup>nd</sup> fifth-wheel	$N$
$C_1$	Cornering Stiffness of the tractor's 1 <sup>st</sup> axle	$\frac{N}{deg}$
$C_2$	Cornering Stiffness of the tractor's 2 <sup>nd</sup> axle	$\frac{N}{deg}$
$C_3$	Cornering Stiffness of the tractor's 3 <sup>rd</sup> axle	$\frac{N}{deg}$
$C_4$	Cornering Stiffness of the first trailer's 1 <sup>st</sup> axle	$\frac{N}{deg}$
$C_5$	Cornering Stiffness of the first trailer's 2 <sup>nd</sup> axle	$\frac{N}{deg}$

$C_6$	Cornering Stiffness of the first trailer's 3 <sup>rd</sup> axle	$\frac{N}{deg}$
$C_7$	Cornering Stiffness of the second trailer's 1 <sup>st</sup> axle	$\frac{N}{deg}$
$C_8$	Cornering Stiffness of the second trailer's 2 <sup>nd</sup> axle	$\frac{N}{deg}$
$C_9$	Cornering Stiffness of the second trailer's 3 <sup>rd</sup> axle	$\frac{N}{deg}$
$\alpha_1$	Side-slip angle of the tractor's 1 <sup>st</sup> axle	$deg$
$\alpha_2$	Side-slip angle of the tractor's 2 <sup>nd</sup> axle	$deg$
$\alpha_3$	Side-slip angle of the tractor's 3 <sup>rd</sup> axle	$deg$
$\alpha_4$	Side-slip angle of the first trailer's 1 <sup>st</sup> axle	$deg$
$\alpha_5$	Side-slip angle of the first trailer's 2 <sup>nd</sup> axle	$deg$
$\alpha_6$	Side-slip angle of the first trailer's 3 <sup>rd</sup> axle	$deg$
$\alpha_7$	Side-slip angle of the second trailer's 1 <sup>st</sup> axle	$deg$
$\alpha_8$	Side-slip angle of the second trailer's 2 <sup>nd</sup> axle	$deg$
$\alpha_9$	Side-slip angle of the second trailer's 3 <sup>rd</sup> axle	$deg$
$S_1$	Distance between the tractor's 1 <sup>st</sup> axle and the CG of the tractor	$m$
$S_2$	Distance between the tractor's 2 <sup>nd</sup> axle and the CG of the tractor	$m$
$S_3$	Distance between the tractor's 3 <sup>rd</sup> axle and the CG of the tractor	$m$

$S_4$	Distance between the first trailer's 1 <sup>st</sup> axle and the CG of the first trailer	$m$
$S_5$	Distance between the first trailer's 2 <sup>nd</sup> axle and the CG of the first trailer	$m$
$S_6$	Distance between the first trailer's 3 <sup>rd</sup> axle and the CG of the first trailer	$m$
$S_7$	Distance between the second trailer's 1 <sup>st</sup> axle and the CG of the second trailer	$m$
$S_8$	Distance between the second trailer's 2 <sup>nd</sup> axle and the CG of the second trailer	$m$
$S_9$	Distance between the second trailer's 3 <sup>rd</sup> axle and the CG of the second trailer	$m$
$h_1$	Distance between 1 <sup>st</sup> hitch point and the CG of the tractor	$m$
$h_2$	Distance between 1 <sup>st</sup> hitch point and the CG of the first trailer	$m$
$h_3$	Distance between 2 <sup>nd</sup> hitch point and the CG of the first trailer	$m$
$h_4$	Distance between 2 <sup>nd</sup> hitch point and the CG of the second trailer	$m$

## APPENDIX B: VEHICLE SYSTEMS MATRICES

The system matrices  $A$  and  $B$  for the 4DOF linear model described in Section 3.2 are given below.

$$A = M^{-1}N; B = M^{-1}P$$

$$M = \begin{bmatrix} h_1 m_1 & I_1 & 0 & 0 & 0 & 0 \\ m_1 & 0 & m_2 & 0 & m_3 & 0 \\ h_2 m_1 & 0 & 0 & I_2 & -h_3 m_3 & 0 \\ 0 & 0 & 0 & 0 & -h_4 m_3 & I_3 \\ 1 & -h_1 & -1 & -h_2 & 0 & 0 \\ 0 & 0 & 1 & -h_3 & -1 & h_4 \end{bmatrix}$$

$$N = \frac{1}{V_x} \begin{bmatrix} n_{11} & n_{12} & 0 & 0 & 0 & 0 \\ n_{21} & n_{22} & n_{23} & n_{24} & n_{25} & n_{26} \\ n_{31} & n_{32} & n_{33} & n_{34} & n_{35} & n_{36} \\ 0 & 0 & 0 & 0 & n_{45} & n_{46} \\ 0 & -V_x^2 & 0 & V_x^2 & 0 & 0 \\ 0 & 0 & 0 & -V_x^2 & 0 & V_x^2 \end{bmatrix}$$

$$P = \begin{bmatrix} -(S_1 + h_1)C_1 \\ -C_1 \\ -h_2 C_1 \\ 0 \\ 0 \\ 0 \end{bmatrix}$$

$$n_{11} = C_1(h_1 + S_1) + C_2(h_1 - S_2) + C_3(h_1 - S_3)$$

$$n_{12} = C_1 S_1(h_1 + S_1) - C_2 S_2(h_1 - S_2) - C_3 S_3(h_1 - S_3) - h_1 m_1 V_x^2$$

$$n_{21} = C_1 + C_2 + C_3$$

$$n_{22} = C_1 S_1 - C_2 S_2 - C_3 S_3 - m_1 V_x^2$$

$$n_{23} = C_4 + C_5 + C_6$$

$$n_{24} = -C_4S_4 - C_5S_5 - C_6S_6 - m_2V_x^2$$

$$n_{25} = C_7 + C_8 + C_9$$

$$n_{26} = -C_7S_7 - C_8S_8 - C_9S_9 - m_2V_x^2$$

$$n_{31} = h_2(C_1 + C_2 + C_3)$$

$$n_{32} = C_1h_2S_1 - C_2h_2S_2 - C_3h_2S_3 - h_2m_1V_x^2$$

$$n_{33} = -C_4S_4 - C_5S_5 - C_6S_6$$

$$n_{34} = C_4S_4^2 + C_5S_5^2 + C_6S_6^2$$

$$n_{35} = -h_3(C_7 + C_8 + C_9)$$

$$n_{36} = h_3(C_7S_7 + C_8S_8 + C_9S_9 + m_2V_x^2)$$

$$n_{45} = -C_7(h_4 + S_4) - C_8(h_4 + S_8) - C_9(h_4 + S_9)$$

$$n_{46} = C_7S_7(h_4 + S_4) + C_8S_8(h_4 + S_8) + C_9S_9(h_4 + S_9) + h_4m_2V_x^2$$

The system matrices  $A_h$  and  $B_h$  for the AHA system model described in Section 3.4 are given below.

$$A_h = M_h^{-1}N_h; B_h = M_h^{-1}P_h$$

$$M_h = \begin{bmatrix} m & c + \frac{A_A^2 + A_B^2}{2 K_c} & 0 \\ 0 & 1 & 0 \\ 0 & 0 & \tau \end{bmatrix}$$

$$N_h = \begin{bmatrix} 0 & -k & \eta_{af}(A_A + A_B)K_p \\ 1 & 0 & 0 \\ 0 & 0 & -1 \end{bmatrix}$$

$$P_h = \begin{bmatrix} 0 \\ 0 \\ \varphi \end{bmatrix}$$